Synthesis and Applications of Discrete TiO_2 Nanotubes in Water Treatments and Superhydrophobic Coatings

By

NAJIA MAHDI

A thesis submitted in partial fulfillment of the requirements for the degree of

Master of Science

In
Microsystems and Nanodevices

Department of Electrical and Computer Engineering

University of Alberta

Abstract

TiO_2 as an n-type semiconducting material is one of the most investigated transition metal oxides with a large bandgap of 3.2 eV that is environmentally friendly, chemically stable, biocompatible and have applications in photocatalysis, superhydrophobic coatings, antifouling membranes for water treatments, solar cells and biomedical technologies due to its physical, optical, chemical and electronic properties. The 1-D nanostructures of TiO_2 such as nanotubes, nanorods, nanowires and nanofibers have been explored extensively due to their effective one-directional charge transport and large surface area when compared with bulk TiO_2. Despite the advantages of 1-D nanotube arrays, to further understand and benefit from their properties in full potential, the discrete TiO_2 nanotubes (d-TNTs) have gained attention specifically in applications where their porosity, hydrophilicity, adsorption capacity, large surface area and fast electron transport without any interruption matter.

The present work described in this thesis is towards understanding the synthesis of TiO_2 nanotubes for simpler discretization and their applications in two different projects; (1) antifouling and hydrophilic fabrication of polymer nanocomposite membranes to be used in water treatments, and (2) all-solution based, scalable superhydrophobic coatings to be used in oil and gas industry as well as two other projects proposed for future work investigating the fluorescent, electrical and optical properties of d-TNTs.

In this thesis, d-TNTs are synthesized using three different organic electrolytes (ethylene glycol, EG-, dimethyl sulfoxide, DMSO-, and diethylene glycol, DEG-) containing fluoride ions to investigate their behavior in superhydrophobic coatings and antifouling polymer membranes. Amongst the other fabrication methods of TiO_2 nanotubes, electrochemical anodization method is

the simplest and cost effective method to synthesize TiO_2 nanotubes with tunable properties such as length, diameter, wall thickness and barrier (oxide) layer thickness. In water treatment application, the hydrophilic TiO_2 nanotubes with large area and high absorbance capacity are used as nanofillers in naturally hydrophobic PES polymer improving the rejection of organic content, water flux and antifouling properties in water filtration processes. In superhydrophobic coatings application, the hydrophobic properties of stainless steel is improved by coating a thick layer of d-TNTs solution due to nanotube's porosity, mechanical strength, distance between nanotubes and inner microvoids that create a Cassie-Baxter state. To further improve the hydrophobicity and corrosion resistance of stainless steel, ODPA (octadecylphosphonic acid) SAMs is used to functionalize the surface of stainless steel after discrete nanotube coating is applied. The resultant surface presents a high contact angle (166±8º) with a good surface coverage and high corrosion resistance confirmed by electrochemical impedance spectroscopy and abrasion/adhesion tests.

Preface

The research work reported in this thesis is carried out at the University of Alberta and the majority of the work including the synthesis of polymer (PES) nanocomposite membranes and metal oxide (TiO_2 nanotubes) as well as their characterization and analysis are done by Najia Mahdi under the supervision of both Professor Karthik Shankar (Department of Electrical and Computer Engineering) and Professor Mohatada Sadrezadeh (Advanced Water Research Lab).

Each chapter of this thesis starts with background information about the fundamentals of synthesis and characterization methods used specifically to the application covered in the chapter. In chapter 1, a detailed introductory information on the background of TiO_2 as a material is given with further explanations about the synthesis and characterization methods of both TiO_2 nanotubes on foil and discrete TiO_2 nanotubes in suspension. In chapter 2, the basic background information about PES polymers and their nanocomposite membranes are given prior to presenting the synthesis and application details that are based on the manuscript titled "Robust Polymer Nanocomposite Membranes Incorporating Discrete TiO_2 Nanotubes for Water Treatment" which has been submitted for publication as a journal article. The sections 2.2.3.2 and 2.2.3.4 which correspond to X-Ray photoelectron spectroscopy (XPS) and Atomic Force Microscopy (AFM) results respectively, were performed by post-doctoral fellows in Prof. Shankar research group. The XPS was performed and analyzed by Dr. Pawan Kumar and the AFM was performed by Dr. Ankur Goswami.

The majority of chapter 3 after section 3.4 was published as P. Roy et al., "All-solution processed, scalable superhydrophobic coatings on stainless steel surfaces based on functionalized discrete titania nanotubes," in Chemical Engineering Journal in 2018. The abstract was used as an excerpt

from the published paper where Najia Mahdi is a co-author. In Chapter 3, the synthesis of d-TNTs, sample preparation of stainless-steel coated with d-TNTs and ODPA SAMs, and some characterizations such as SEM and preliminary contact angle measurements were done by Najia Mahdi. The majority of characterizations such as electrochemical impedance spectroscopy, Tafel analysis, abrasion and adhesion tests as well as optimization of stainless steel functionalization was performed by Dr. Partha Roy.

Chapter 4 of this thesis consists of the summary as well as the two proposed projects based on d-TNTs. All the preliminary fundamental work is done by Najia Mahdi, except the fluorescent microscopy images presented in section 4.2.1.2 which were acquired with the help of Aarat Kalra, PhD student in Prof. Shankar's group.

Dedication

I would like to dedicate this thesis to my parents Wahid Mahdi, Jamila Mahdi and my sister Nabila Mahdi. I would not be able to complete this thesis without your support and love.

“One last dance
To forget my immense pain
I want to run away, that everything begins
Oh, my sweet suffering “

Acknowledgements

I would like to thank Dr. Shankar first, for his endless support and understanding during my academic journey as an undergraduate capstone student and later as a master's student in his research group. During my time in Professor Karthik Shankar's group, I have learned to push the boundaries to be a better version of myself both academically and personally, gained confidence in my skills and improved more and learned that miracles really happen sometimes and hard work somehow pays off at the end when there is no hope left to have faith on. Again, many thanks to Dr. Shankar and Dr. Mohtada Sadrezadeh for letting me be a part of their research groups which will be an unforgettable experience of my life.

I wish to thank Dr. Piyush Kar for his kind supervision, friendship and support during my hard times. Also, special thanks to Dr. Pawan Kumar for being an awesome mentor and friend who has a positive perspective about the situations that seemed very difficult to overcome and listened to me when things were not going right and always found an easy and fun solution. I wish to express my warm thanks to my colleagues Dr. Kazi Alam, Yun Zhang, Dr. Partha Roy, Ujwal Thakur, Sheng Zeng, Mourad Benlamri, Dr. Samira Farsinezhad, Dr. Arash Mahmoudpor, Ben Wiltshire, Dr. Mohammad Zarifi, Ajay Manuel, Weidi Hua, Ryan Kissingler, Advaita Bhatnagar, Aarat Kalra, Saralyn Riddell and many more.

Also, I would like to thank my dear parents and sister for their support, encouragement and unconditional love. My parents have sacrificed so much to raise me and my sister and had all their faith on us and our future. Finally, I would like to express my warmest feelings to my friends Arezoo Hosseini, Navid Hosseini, Mehmet Meric Hirpa, Vishakha Gupta, Bardia Rahmani and Ehsan Vahidzadeh for giving me all the love and being my second family.

Table of Contents

List of Tables

List of Figures

List of Abbreviations

Abbreviations	Description
TiO_2	Titanium Dioxide (Titania)
Ti	Titanium
ODPA	Octadecylphosphonic Acid
SAM	Self-Assembled Monolayer
TNT	Titanium Dioxide Nanotube
d-TNT	Discrete Titanium Dioxide Nanotube
SEM	Scanning Electron Microscope
WCA	Water Contact Angle
CNTs	Carbon Nanotubes
ECA	Electrochemical Anodization
AAO	Anodic aluminum Oxide
1-D	One Directional
HCl	Hydrochloric Acid
DI	Deionized Water
HF	Hydrogen Fluoride
NaF	Sodium Fluoride
KF	Potassium Fluoride
EG	Ethylene Glycol
DEG	Diethylene Glycol
DMSO	Dimethyl Sulfoxide
SSTNM	Self-standing Nanotube Membranes
H_2O_2	Hydrogen Peroxide
H_2SO_4	Sulfuric Acid
NH_4F	Ammonium fluoride
Bu_4NF	Tetrabutyl Ammonium Fluoride
$BnMe_3NF$	Benzyltrimethyl Ammonium Fluoride
Ag/AgCl	Silver/Silver chloride
DC	Direct Current
FAD	Field Assisted Dissolution
$[TiF_6]^{2-}$	Hexafluoro Titanium Complex
NF	Nanofiltration
MF	Microfiltration
UF	Ultrafiltration
RO	Reverse Osmosis
PVA	Polyvinyl Alcohol
PES	Polyether sulfone
PP	Polypropylene
PVDF	Polyvinylidene fluoride
PVC	Polyvinyl chloride

Abbreviations	Description
PAN	Polyacrylonitrile
PVP	Polyvinylpyrrolidone
PI	Polyimide
PE	Polyethylene
CA	Cellulose Acetate
NIPS	Non-solvent Induced Phase Inversion/Separation
SAGD	Steam Assisted Gravity Drainage
FE-SEM	Field Emission Scanning Electron Microscopy
AFM	Atomic force Microscopy
FTIR	Fourier-transform Infrared Spectroscopy
XPS	X-Ray Photoelectron Spectroscopy
WLS	Warm Lime Softener
DMA	N, N-dimethylacetamide
HR-XPS	High-resolution XPS spectra
TOC	Total Organic Carbon
SS	Stainless Steel
SH	Superhydrophobic
PTFE	Polytetrafluoroethylene
APA	Alkylyphosphonic acid
PFDPA	1H,1H,2H,2H-perfluorodecylphosphonic acid
EIS	Electrochemical Impedance Spectroscopy
AC	Alternating Current
IRRAS	Infrared reflection Absorption Spectroscopy
PL	Photoluminescence
DEP	Dielectrophoresis

Chapter 1- Introduction

1.1 Introduction to TiO_2

Titanium dioxide (titania, TiO_2) is a versatile, non-toxic material that can be produced in many forms of nanostructures such as nanowires, nanoparticles, nanorods, nanoribbons, and nanotubes [1-3]. In the past many decades, an extensive research time has been devoted to the investigation of engineered metal- oxide nanostructures.

Although, TiO_2 has been used in white pigment from ancient time, however, William Gregor first discovered titanium dioxide in black magnetic sand in 1791. Titanium dioxide was first explored in 1972 by Fujishima and Honda for its potential to be used for water photolysis [4]. In 1991, after the discovery of carbon nanotubes (CNTs) by Lijima et al., one-dimensional tubular nanostructures have been extensively investigated. Among the other metal oxide and titania nanostructures, TiO_2 nanotubes (TNTs) have been studied the most due to their facile and cost –effective fabrication and desirable enhanced properties such as high refractive index of 2.4 for anatase and 2.7 for rutile phase, mechanical robustness, chemical inertness and high transparency. Various fabrication methods such as template-assisted technique [5, 6], hydrothermal method [7-9], solvothermal method [10], and electrochemical anodization (ECA) method [11-13] have been used to synthesize one dimensional TiO_2 nanotubes (TNTs). In 1999, Hoyer et al. first reported the synthesis of TNTs using the template-assisted method [5]. In the same year, Zwilling prepared an electrolyte containing fluorine and synthesized regular porous titania using the electrochemical anodization method which promoted many other researchers' work in the synthesis of TNTs [14]. Later in 2001, the first successful synthesis of TNTs using electrochemical anodization was reported by Zhi Chen and his group [15, 16]. Although each method has its own unique features and

advantages; the facile, cost-effective and self-organized TNTs were formed by electrochemical anodization method.

One dimensional, n-type semiconducting nanotube array of TiO_2 with a wide band gap of 3.2 eV for anatase and 3.0 eV for rutile phase have been the center of attention in many research fields of science and technology. The optical and electrical properties of semiconducting TiO_2 nanotubes compared to their bulk material are the striking distinguishing factors which have attracted many researchers [17]. The large surface area of nanotubes possesses strong adsorption capacity which specifically enables antifouling water treatment, superhydrophobic coating, highly efficient photovoltaic cells, photocatalysis, nanoelectronics and sensors applications [18-23].

1.2 Processing Methods of TNTs

In this section, the main preparation methods of TiO_2 nanotubes are discussed in detail. As mentioned before, various methods have been explored to tailor the synthesis of nanotubes based on the needs of the applications. The brief explanations for each method are given to compare their advantages, disadvantages and functional features.

1.2.1 Template-Assisted Method

Anodic aluminum oxide (AAO)-template assisted method is a TNTs processing method in which AAO film with uniform pores is used as a template for 1-D nanostructure growth [24]. Wang [25] and Brinda [26] prepared TNTs using this method by immersing the aluminum oxide template in a filling colloid (TiO_2 precursor) solution. The TNTs synthesized by AAO template assisted method usually have lower nanotube surface area due to the thicker nanotube wall. Also, the pore size of the template mostly affects the diameter of synthesized nanotubes which is a limitation for many applications. The biggest drawback of this method is that the nanotubes prepared are stripped from the template using calcination and HCl treatment and this might break parts of the nanotubes.

This is mainly caused by the limitation in the choice of substrate. On the other side, the advantages of the template method are the uniformity and controllable scale of nanotube growth and size by the applied template [27].

1.2.2 Hydrothermal Method

The hydrothermal method is one of the most commonly used aqueous solvent based synthesis methods of TNTs and it is a processing technique based on the crystal growth, crystal formation, phase equilibrium and fine crystal formation. The synthesis of 1-D TNTs by hydrothermal method using amorphous TiO_2 powder treated at high temperatures in a highly concentrated NaOH solution was first reported in 1998 by Kasuga Tomoko [27].

In a typical synthesis process, an autoclave which consists of a steel pressure vessel is used to enclose the mixed reaction solutions of NaOH/KOH and the TiO_2 precursors (anatase or rutile). The vessel is then kept in a temperature (~180 °C) and pressure-controlled oven for about 5 or 6 h depending on the required thickness of TNTs. Due to the temperature gradient, the hotter region dissolves the TiO_2 precursor and in the cooler region, the dissolved chemicals are deposited on a seed crystal, promoting the growth of the crystal. The hydrothermal process usually forms alkali metal titanate on the surface of hydrothermally grown TiO_2. After the reaction, nanotubes are washed with DI water to remove Na^+ ions followed by treatment with HCl resulting in the formation of anatase form TiO_2 nanotubes after drying. As a result of the reaction in vessel, the hydrothermal process has almost 99-100% conversion for the precursors to form TNTs in one process time. The high nanotube production rate and easy enhancement of nanotube features are some advantages of this method. On the other side, long reaction durations, the difficulty of achieving uniform size nanotubes, non-directionality of nanotubes and dependency on seed crystal size are the disadvantages making this process less desirable to be used in many applications [28].

1.2.3 Solvothermal Method

A solvothermal method is very similar to the hydrothermal method in reactions conditions aspect of forming nanotubes under high temperature and high pressure. The main difference between these two process techniques is that the solvothermal method uses organic solvents instead of aqueous solutions [29-31]. Due to the variety and higher boiling points of organic solvents, higher temperature and pressure can be used to control the crystal phase, nanosize, agglomeration of products and size distribution in solvothermal method [30, 31]. In the solvothermal method, the solvents used play a key role determining the crystallization behavior of the product, solubility and reaction time. In the end, when hydrothermal and solvothermal process techniques are compared, the solvothermal method have more advantages.

1.2.4 Electrochemical Anodization Method

Electrochemical anodization (ECA) is an in-situ nanotube fabrication method which is widely used for anodizing many metals such as 1-D TNTs. Compared to the methods such as hydrothermal, solvothermal and template-assisted methods, the electrochemical anodization method is a facile, cost effective, non-toxic and recyclable technique which produces self-organized, ordered, and vertically-oriented nanotubes to the surface of the electrode substrate.

Electrochemical anodization process consists of two electrodes dipped in an electrolyte and applied opposite bias. The electrode to be oxidized is the anode and it is connected to the positive terminal of a power supply of voltage source. The electrode that is conductive is the cathode which can be the same metal, platinum or graphite with similar dimensions as the anode. The formation of nanotubes is achieved in acidic electrolytes containing chloride or fluoride ions. During this

process, when a voltage is applied, the reduction of hydrogen ions on the surface of cathode electrode causes the formation of hydrogen bubbles. On the other side, the metal surface of the anode is exposed to the oxygen ions of electrolyte which results in oxidation [32].

The growth of nanotubular structures can be achieved by a trade-off between the dissolution by the electrolyte and the oxide growth. There are also many other parameters which affect the nanotube growth which are; electrolyte, voltage, temperature, pH, water and fluoride content. Parameters such as nanotube length, tube diameter, intratubular spacing and wall thickness to further control the nanotube geometry for specific applications have been researched extensively. There have been four generations of electrolytes for electrochemical anodization of nanotubes so far which have produced nanotubes with specific properties. Each electrolyte in four generations has its own advantages and shortcomings.

First Generation: Hydrogen fluoride (HF)-based electrolytes were used for the first-generation electrolytes. Due to the high etching rate of HF, the growth of nanotubes longer than 500 nm was restricted. In HF-based electrolytes, the temperature of bath was manipulated to change the wall thickness of short and tapered conical shaped TNTs [33, 34].

Second Generation: Nanotubes with lengths up to 4.4 μm have been fabricated using the second-generation acidic (3-5 pH) NaF and KF electrolytes [35]. It was discovered that at lower pH, the length of the nanotubes was short and increasing the pH in these electrolytes increased the nanotube length. Also, increasing the anodization voltage and duration resulted in an increase in the tube diameter and tube length respectively [36].

Third Generation: The third-generation electrolytes consist of the polar organic solvents such as ethylene glycol (EG), diethylene glycol (DEG), formamide, dimethyl formamide, dimethyl

sulfoxide (DMSO) and glycerol provide the best control over the nanotube dimensions among the other electrolytes [37-41]. The third-generation electrolytes enable the growth of nanotubes up to 2 mm in length due to their high viscosity and lower conductivity [42]. Also, self-standing nanotubes membranes (SSTNM) with a tube length of 2 mm was fabricated by double size anodization consuming the metal electrode.

Fourth Generation: The fourth-generation electrolytes are fluoride free and consisted of HCl, H_2O_2, and H_2SO_4 which produce bundles of nanotubes. Although, the electrolytes based on chloride fabricates very high aspect ratio nanotubes in very short amounts of time such as 5 minutes, the major drawback of the fourth generation is the non-uniformity of nanotubes [43].

1.3 Tunable Morphology of TNTs in Electrochemical Anodization

Formation of nanotubes is affected by many factors such as electrolyte, voltage, water and fluoride content, electrolyte temperature, pH and anodization duration. The effect of all these parameters are explained in detail in this section especially focusing on organic electrolytes as well as giving some information about the aqueous electrolytes.

1.3.1 Effect of Electrolyte

The choice of electrolyte used in electrochemical anodization has a strong influence on the anodization parameters determining the properties of nanotubes and the applications they are used for. In this thesis, the discrete titania nanotubes used for various applications were formed with organic electrolytes due to flexibility in controlling the parameters specially the length, nanotube diameter and intratubular distance. Each electrolyte produces different electric field intensities based on their nature. For instance, higher breakdown in oxide layer due to higher electric field intensity results in the formation of nanotubes with wider diameters. Also, the chemical dissolution

of each electrolyte differs which affect the formation of debris which is also called nanograss on the surface of nanotubes by slicing the nanotube mouth at higher dissolution rates.

1.3.2 Effect of Voltage

The applied voltage in anodization strongly affects the tube diameter. Also, voltage influences the film thickness and inter pore/tubular distance [44]. At lower applied voltages, due to less electric field dissolution, titania nanotubes with smaller diameters form. Based on the observations, if the voltage is too low, then the oxide layer becomes thicker without forming any nanotubular structure. Also, if the applied voltage is too high, then in that case instead of nanotubular structures, a sponge-like structure form or in some cases, discrete, hollow and tube-like nanostructures form. Although the applied voltage has a huge impact on the nanotube diameter, the range of voltage to be applied is dependent on the type of electrolyte used in electrochemical anodization. Due to the low conductivity of organic electrolytes, the applied voltage does not have a huge influence on the nanotube formation in non-aqueous electrolytes. On the contrary, the aqueous electrolytes affect the nanotube growth and the range of anodization voltage is usually between 10 V to 25 V. The high pH value of aqueous electrolytes with higher dissolution rate causes local acidification at the bottom of the tubes. If the voltage is increased more than the voltage range, then permanent dissolution of oxide layer occurs inhibiting the formation of nanotubes [45].

1.3.3 Effect of Electrolyte Temperature

The effect of electrolyte temperature in electrochemical anodization was first reported by Lin and Wang in aqueous and non-aqueous fluoride containing electrolytes [46]. The electrolyte temperature directly affects the wall thickness, rate of oxide growth and length [47, 48]. As the temperature increases bundles or lumps of nanotubes form which are mechanically unstable. The increase in electrolyte temperature increases the pore size due to lower viscosity of electrolyte

increase the mobility of fluoride ions which leads to a faster etching rate [49]. As the chemical dissolution rate increases due to even higher temperatures, titania nanotubes can produce corrosion resulting in agglomeration on the nanotube surface. Contrarily, when the electrolyte temperature is decreased to 5° or lower, the ion mobility decreases leading to slower etching rate of oxide layer. As a result, regular pores do not form in lower temperature [50]. Based on the observations presented in figure 1.1, at higher electrolyte temperature the wall thickness of TNTs decreases and at lower temperatures, the wall thickness of TNTs increases.

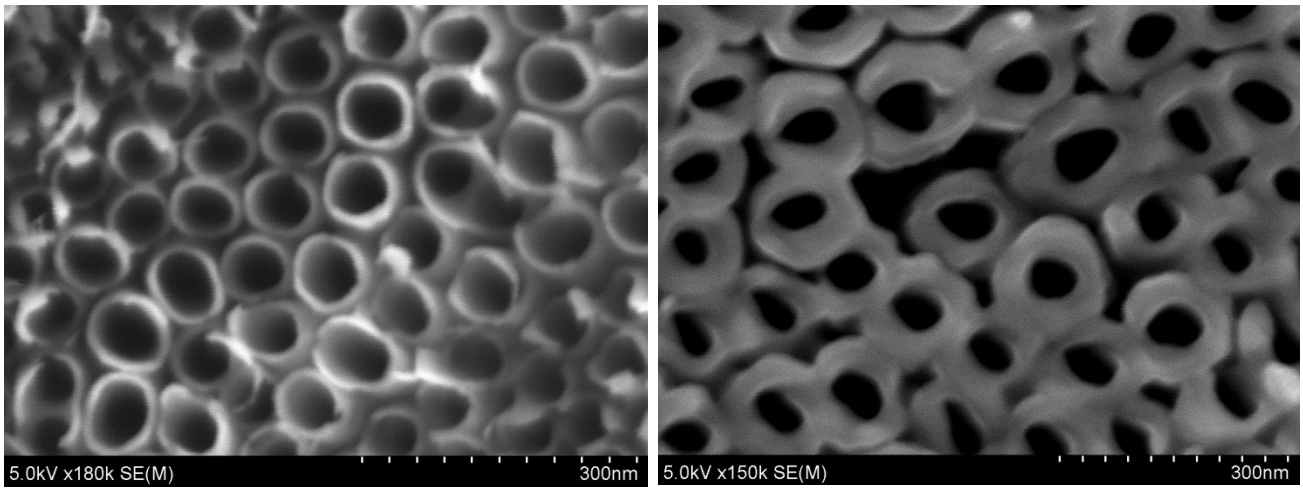

Figure 1.1 SEM images of TiO_2 nanotubes anodized in different electrolyte temperature **(a)** EG electrolyte at 50°, **(b)** EG electrolyte at 0°.

1.3.4 Effect of pH

The pH value of the electrolyte directly affects the TiO_2 dissolution rate which in turn affects the length and diameter of the nanotubes as reported by Kang et al [51]. In a study of pH value in electrolyte, Hazan et al. found that the oxide dissolution rate is accelerated with lower pH values. Also, the inner diameter increased enhanced acidic electrolytes due to high chemical dissolution rate. On the contrary, it was discovered that the inner diameter does not change with higher pH values [52]. In an electrochemical anodization process, the pH value at the tube bottom is controlled by self-acidification process whereas; the pH value at the tube mouth is controlled by

the pH of the bulk solution. Even though the chemical dissolution reaction also occurring at the tube mouth, the reaction is extremely slow resulting in longer anodization durations [53].

1.3.5 Effect of Water Content

To successfully grow titania nanotubes especially in organic electrolytes, the water content should be kept under 5% volume. When the water content is reduced in organic electrolytes, the oxygen needed for the formation of oxide barrier layer is also reduced resulting in thinner oxide layer underneath the nanotubes [54,55]. Moreover, when the water content is reduced, the chemical dissolution rate of TiO_2 at the nanotube mouth decreases leading to the formation of longer titania nanotubes in fluoride containing organic electrolytes [56]. The anodization process suffers from lack on hydrogen ions in the absence of water in electrolytes. Also, the high viscosity of electrolyte without water results in the formation of oxide layer only.

1.3.6 Effect of Fluoride Content

The key factor in the formation of titania nanotubes is the fluoride ions which affect the current density to be higher compared to the non-fluoride electrolytes. A compact oxide layer forms if there are no fluoride ions in the electrolyte. Increasing the fluoride concentration increases the nanotube length. The presence of various cations in fluoride containing compounds also affects the nanotube growth. Based on a study reported by Shankar and co-workers [57,58], when five different fluoride compounds namely; HF, NH_4F, sodium fluoride (NaF), tetrabutyl ammonium fluoride (Bu_4NF) and benzyltrimethyl ammonium fluoride ($BnMe_3NF$) were compared, the longest nanotube arrays was found to be 94 μm in an electrolyte containing Bu_4N^+ and the shortest grown nanotubes grown was observed in H^+ containing electrolyte. This was explained by the effect of quaternary ammonium ions which reduced the formation of barrier oxide layer. As a

result, the thinner oxide layer leads to higher ionic transport through the oxide layer increase the rate of nanotube growth.

1.3.7 Anodization Duration

The effect of anodization duration depends on the electrolyte used. For instance, in aqueous water-based electrolytes, after about an hour the nanotube length becomes independent of anodization duration. Due to high acidity in aqueous electrolytes, the chemical dissolution rate at the top of the nanotubes equals to the rate of nanotube formation at the bottom. As a result, the length of titania nanotubes were limited to about 500 nm in HF-water based electrolytes. When the pH of these electrolytes was increased to near-natural, the maximum nanotube length obtained was reported to be 4.4 μm after 20 hrs [59]. In the contrary, based on the observations of Macak and Schmuki, the nanotube length is time-dependent [60]. Based on the observations of Li et al., the minimum time needed for nanotube formation is 15 min. At 5 min, the formation of porous structure was observed [60]. Recently, So et al reported that the addition of lactic acid can greatly enhance the nanotube growth in very short durations of anodization such as 7 μm at 25 seconds. This is achieved by a higher ion transport through oxide layer by reduction of localized dielectric breakdown of oxide layer at higher applied voltages by lactic acid [61]. The nanotube length increases up to 1 h of anodization but eventually due to over dissolution of nanotubes at the tube mouth by fluoride ions causes collapse of nanotubes.

1.4 Crystalline Phases of TNTs

Among the transition metal-oxides, TiO_2 is one of the most studied materials that is environmentally friendly, economic and earth-abundant. The TiO_2 material exist in three natural phases (polymorphs) namely anatase (tetragonal, a=b=3.782 Å, c=9.502 Å), rutile (tetragonal, a=b=4.584 Å, c=2.953 Å) and brookite (orthorhombic, a=5.436 Å, b=9.166 Å, c=5.135 Å) [62-

64]. Although rutile phase is the most stable in terms of thermodynamics, anatase is the most preferred phase due to its higher conduction band edge and large bandgap (3.20 eV) which enables photocatalytic and optoelectronic applications. The structural details of each phase of TiO_2 are illustrated in figure 1.2.

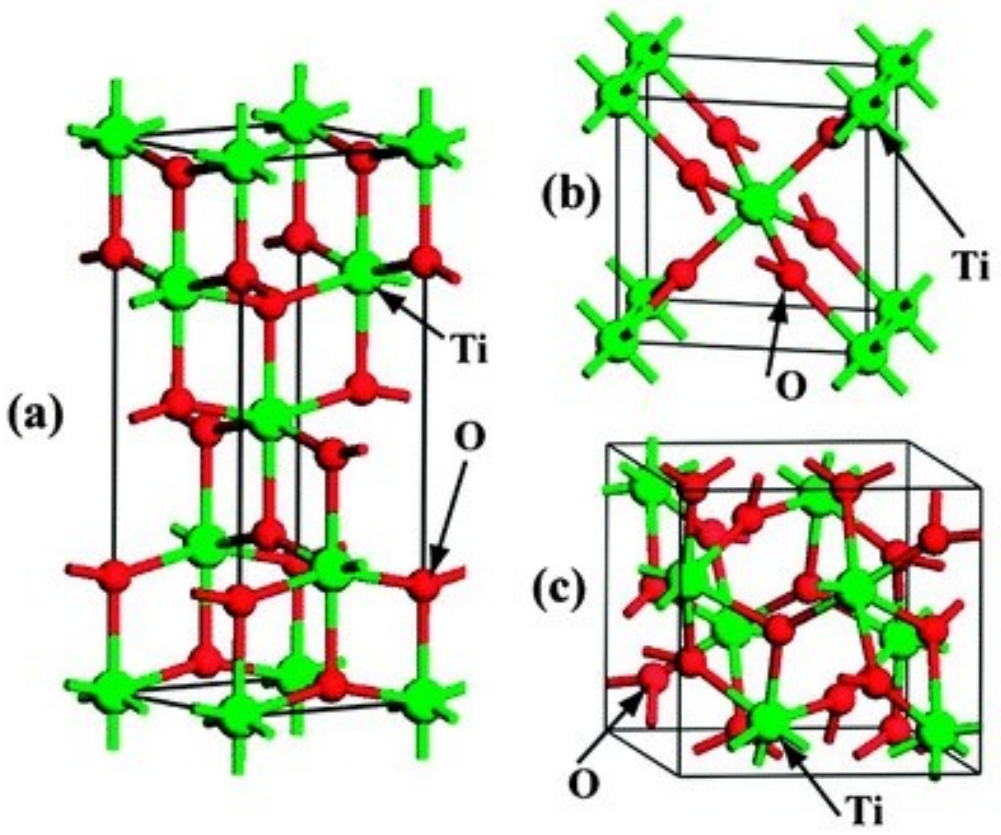

Figure 1.2 – The schematic of unit cells of (a) anatase, (b) rutile, and (c) brookite TiO_2. (The red spheres represent the O atoms and green spheres Ti atoms. Reprinted with permission from ref. [74] Royal Society of Chemistry 2014.

Anatase and rutile phases of TiO_2 are the most commercially used structures as they have been studied based on the surface science techniques. The TiO_2 nanotubes prepared with anodization have an amorphous structure. Since the amorphous structure is not photoactive, high temperature annealing method is used to transform the nanotubes into anatase starting at 280 °C, a mixture of

anatase and rutile at 450 °C, and rutile at 700-800 °C [65-67]. The thermal annealing atmosphere and temperature mainly affect the crystallinity, conductivity, photoresponse and lifetime of charge carrier of nanotubes.

Both anatase and rutile structures consist of a building block where a titanium atom is surrounded by six oxygen atoms. The anatase phase has a slightly larger distortion of the TiO6 octahedron compared to the rutile phase [68, 69]. In both anatase and rutile, the aspices of octahedron are a little longer between the two bonds of titanium and oxygen atoms. In rutile, one corner along <110> direction is shared by the neighboring octahedra. In anatase, (001) plane is formed by the corner-sharing octahedra. The brookite phase is formed by edge-sharing TiO6 octahedra. Due to less dense structure and high cell volume of brookite, it has not often used in experimental investigations. Therefore, the main differences between the three phases of TiO_2 are the average distance between the oxygen and titanium atoms and the way in which octahedra are packed. Although the rutile phase is stable at most pressures up to 60 kbar and temperatures, it was found that the anatase phase is more stable than rutile at 0 K with particle sizes lower than 14 nm [70]. Also, the photoactivity of anatase is higher which enables many applications in related areas due to lower capacity to adsorb oxygen, and slightly higher Fermi level.

1.5 Formation of TiO2 Nanotubes via Electrochemical Anodization

As mentioned before, TiO_2 nanotubes with large interfacial area and flexibility in controlling the synthesis parameters are better candidates for surface-area dependent applications. Out of all the other synthesis methods, the anodization method is proven to be the most promising and effective way to fabricate highly-ordered nanotubes.

An electrochemical anodization device can consist of either three-electrodes or a simple two-electrode design. In a three-electrode set up, titanium (Ti) foil is the working electrode (anode),

usually either platinum, graphite or titanium are the counter electrode (cathode), and Ag/AgCl is the reference electrode. However, the two-electrodes set up only consist of an anode and cathode which are Ti foil and an inert metal electrode [71]. Besides the electrodes, the anodization process needs an electrolyte containing either fluoride ion, bromide ion, chloride ion, chromium ion or perchlorate and DC power supply.

The main principles of formation mechanism of anodic TiO_2 nanotubes come from the report in 1969 where Diggle studied the formation of compact anodic oxide and porous anodic oxide [72]. Although a huge amount of research work was based on the transition of pores to tubes, the process was not explained theoretically at the time. Based on the conventional field-assisted dissolution (FAD), the process of self-organized TiO_2 nanotubes formation occurs due to four relatively independent procedures namely; electrochemical oxidation of Ti, formation of oxide layer (TiO_2), electrical field induced dissolution of oxide layer, and the fluorine ion induced chemical dissolution. In an electrochemical anodization process, the fluoride ion (F^-) is a key factor in the formation of nanotubular structure because it can form soluble hexafluoro titanium complex ($[TiF_6]^{2-}$). Also, due the small ionic radius of fluoride ion, it acts as an oxide dissolution agent. The formation of nanotubes can be explained by the following equations and figure 1.3 in three distinct stages:

Oxidation of Ti:

$$Ti \rightarrow Ti_4^+ + 4e^- \quad (1)$$

Formation of oxide layer:

$$Ti_4^+ + 2H_2O \rightarrow TiO_2 + 4H^+ \quad (2)$$

Dissolution of oxide layer:

$TiO_2 + 6F^- + 4H^+ \rightarrow [TiF_6]^{2-} + 2H_2O$ (3)

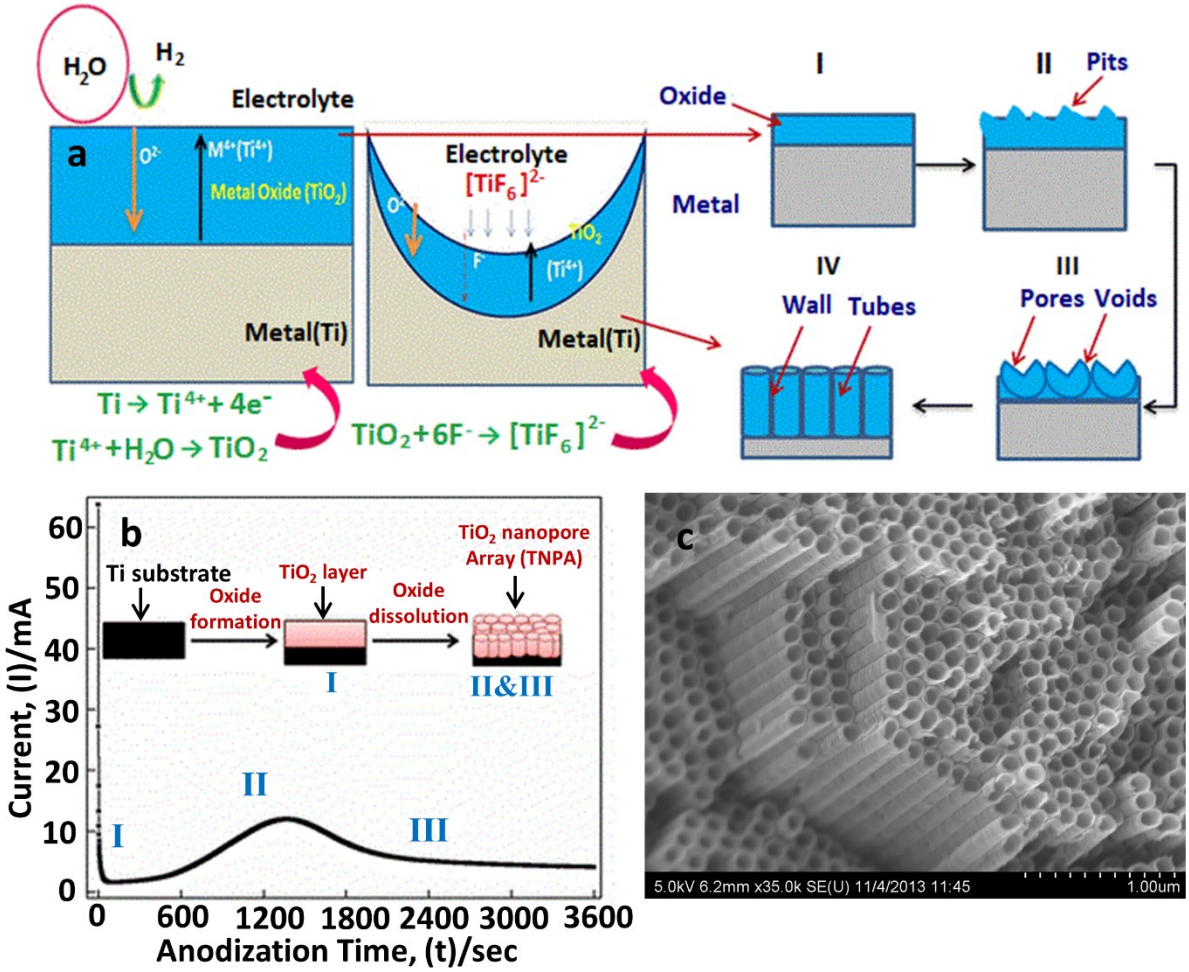

Figure 1.3 Schematic representation of TiO_2 nanotube synthesis details (a) nanotube formation process. (b) Current vs. time plot for a typical anodization process. (a) and (b) are reprinted with permission from ref. [75] (c) SEM image of top view of TiO_2 nanotubes.

Based on equation 2 and stage (1) of figure 1.3, there is a rapid current decay due to the formation of oxide layer. In this stage, during hydrolysis H^+ ions accumulate, and to achieve a balance or electroneutrality, F^- ions migrate to the sites of H^+. In other words, $O2^-$ migrate inward towards the metal/oxide interface and $Ti4^+$ ions migrate outwards towards the oxide/electrolyte interface. In stage (2) of the figure 1.3 (b), the current starts to rise with a time lag due to an increase in the

surface area of the anode. In this stage the higher the concentration of fluoride is the shorter time lag due to the fluoride induced dissolution of TiO_2 by the formation of $[TiO6]^{2-}$ (equation 3). The formation of pores initiates the growth of TiO_2 nanotubes. In stage (3), the current reaches a steady state when the rate of induced dissolution of formed TiO_2 is in equilibrium with pore growth rate at the metal/oxide interface. The formation of self-organized TiO_2 nanotubes are mainly influenced by the potential distribution at the Ti surface. The nanotube formation can be summarized by the following steps:

(a) formation of oxide layer,

(b) pore formation and deepening of the pore,

(c) incorporation of adjacent small pores into a big pore,

(d) earlier nanotube arrays formation, and

(e) formation of perfect nanotube arrays [55]

1.5.1 Discrete TiO_2 Nanotubes

Although, the synthesis details and applications of TiO_2 nanotubes have been explored extensively in different forms such as on native substrates, non-native substrates as transparent nanotubes and free-standing nanotubes, it is not very common to come across studies based on discrete dispersed titania nanotubes. The study of discrete nanotubes is specifically very interesting due to its applications in electronics, superhydrophobic coating in many fields, and highly adsorbent hydrophilic nanofiller in water treatment applications based on polymer membranes.

1.5.1.1 Formation of Discrete TiO_2 (d-TiO_2) Nanotubes

Based on the observations in this thesis work, the formation of discrete titania nanotubes mainly depends on the barrier (oxide) layer thickness and the intratubular distance between the titania nanotubes. These two parameters mainly depend on the choice of electrolyte being employed in the electrochemical anodization processes. As mentioned in previous sections, the titania nanotubes with high surface area, high aspect ratio and highly-ordered structure have been fabricated using the organic electrolytes which enables us to tune anodization parameters to synthesize nanotubes with required functionalities.

Discrete titania nanotubes were formed with mainly using three different fluoride based organic electrolytes such as ethylene glycol (EG), dimethyl sulfoxide (DMSO), and diethylene glycol (DEG). In the first stages of fabricating discrete titania nanotubes, fluoride containing – EG electrolyte with 4% distilled water (DI), 0.3 wt. % NH4F was used in the anodization process. Although, we could fabricate highly-ordered nanotubes, the main obstacle in this recipe was the close packed nanotube morphology which prevented us from discretizing the nanotubes in simple ways. The discretization of nanotubes synthesized in EG based electrolyte needed a two-step process where the nanotubes had to be delaminated from the native substrate (which is Ti foil) first and then sonicated in a solution containing a very small concentration of HF to dissolve the side ripples of nanotubes that connect the walls causing a very dense pack. This method made the discretization process undesirable due to the steps it involved, and safety concerns caused by constant use of HF as a dispersion solvent.

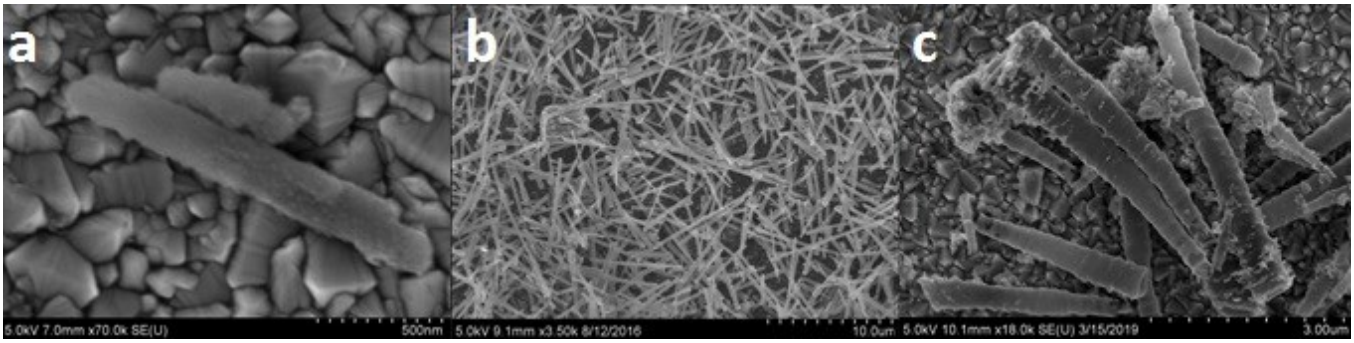

Figure 1.4 SEM images of discrete (individual) TiO_2 nanotubes fabricated with different electrolytes. d-TNT fabricated with (a) EG (b) DMSO (c) DEG

In contrast to the titania nanotubes synthesized with EG based electrolyte, anodization in DMSO and DEG based electrolytes leads to large tube-to-tube spacing. Based on the literature, the main problem with using DMSO and DEG based electrolytes is the anodization time required for the formation of self-organized nanotubes. When nanotubes formed in these two electrolytes compared, the DMSO electrolyte has a higher growth rate of titania nanotubes than DEG electrolyte. This is mainly due to the protophilic nature of DMSO as it accepts a hydrogen (proton) from HF leading to an increase in the pH of the electrolyte. As a result, the chemical etching capability of the electrolyte decreases shifting the breakdown voltage that is mostly dependent on ion concentration [71]. The discrete nanotubes used in the 3rd chapter of this thesis is made by 2 vol. % HF-containing DMSO electrolyte (explained further in chapter 3). This recipe was also used in a report by Roy et al. where the nanotubes have a reduced tube-to-tube binding strength and easily dispersed in an ethanol/water solution and later used to enhance blood clotting for the control of hemorrhage [73].

In the 2nd chapter, discrete nanotubes were synthesized by using a 2 vol. % HF-containing DEG electrolyte. The growth rate of nanotubes is the slowest in DEG electrolyte due to its high viscosity

(35.7 mPa.s) and slower migration of fluoride ions. Compared to nanotubes formed in DMSO electrolyte, in DEG electrolytes the nanotubes are bundle free with larger intratubular distance. Out of the three electrolytes, nanotubes formed with DEG based electrolyte have more applications as an individual or free-standing nanotubes due to their weak adhesion to the barrier (oxide) layer.

1.6 Thesis Scope

In recent years, the mechanical, chemical and electronic properties of individual nanotubes have been studied to better understand the behavior of nanotubes separately from the nanotube arrays and its bulk version. The scope of this thesis is limited to synthesis methods and applications of discrete TiO_2 nanotubes. All the chapters include an overview of the application including specific synthesis details of discrete nanotubes as well as the list of references at the end.

Chapter 2 is focused on the water treatment application of discrete TiO_2 nanotubes incorporated PES polymers. A detailed review of background information on polymer membrane synthesis method, application, surface modification, antifouling phenomena and characterization of nanotube incorporated PES membranes are included in two main sections of this chapter.

Chapter 3 is based on the superhydrophobic applications of spray coated discrete TiO_2 nanotubes on stainless steel. The background information, the effect of monolayers (SAM) on surface properties of discrete TiO_2 nanotubes, the characterizations (providing more detail) are included in this chapter.

Finally, chapter 4 includes a summary of previous chapters as well as two specific project details as future work. These two projects form the fundamentals of electronic applications of discrete TiO_2 nanotubes. For each of these two projects background information, experimental details and discussions as well as the possible application information is presented.

Chapter 2. Robust Polymer Nanocomposite Membranes Incorporating Discrete TiO_2 Nanotubes for Water Treatment

2.1 Introduction to Antifouling Membranes in Water Treatment

The membrane technology has been studied over few decades for applications such as water purification and waste water management due to its cost effectiveness, easy production and high removal capacity of foulants. An increase in world population and demand for clean water motivates the researchers to find new and reliable techniques to clean water. The overall available source of water for drinking purposes in Earth is only about 0.5 % and about 97% is salt water which is not available for human use due to its high salinity [1, 2].

The membranes to be used in water treatment applications are classified as polymer and inorganic membranes. The inorganic membranes have high mechanical, structural and thermal stability and are made of metals or ceramic materials. The major drawback of the inorganic membranes is their low permeability. Although micro porous silica membranes are used in sieving applications, it cannot be used in applications where the tunability of pore size is required. Also, the inorganic membranes have some disadvantages such as solid acidity, adsorption and ion exchange capacity. On the other side, the polymeric membranes have a wide range of applications due to their high permeability, flexibility, low cost, chemical stability, mechanical strength and high tunability of pore size, membrane thickness and surface modification properties [3, 4].

2.1.1 Polymer Membranes for Filtration Applications

Water filtration with polymeric membranes have been used in various applications based on their pore size and are classified as nanofiltration (NF), microfiltration (MF), ultrafiltration (UF), and reverse osmosis (RO) [5-8]. In MF, the pore size of the membrane must be 0.1-1 μm where it can separate larger particles such as bacteria and colloids. The UF membranes require pore sizes from

0.01- 0.1 μm to separate macromolecules, viruses, and high molecular solutes. The NF membranes are highly dense with pore sizes from 0.001- 0.1 μm where it only passes the monovalent ions and removes divalent ions. The RO membranes are the densest membranes out of all the membranes with very small pore sizes which are less than 0.001 μm and it removes the monovalent ions cleaning the water to a high extent. All these filtration processes are high pressure driven [9, 10].

The polymeric membranes can be fabricated with various materials such as Polyvinyl alcohol (PVA), Polyether sulfone (PES), Polypropylene (PP), Polyvinylidene fluoride (PVDF), Polyvinyl chloride (PVC), Polyacrylonitrile (PAN), Polyimide (PI), Polyethylene (PE), Cellulose acetate (CA), Polyamide (PA) and Chitosan [11]. Among all the polymers, PES is the most widely used polymer due to its higher permeability, oxidation and pH resistance, chemical inertness, mechanical, thermal and hydrolytic stability [12].

2.1.2 Phase Inversion Phenomena

The membrane structure can be categorized as symmetrical and asymmetrical. Compared to the symmetrical membranes that have uniform pore size, the asymmetrical membranes are consisted of a dense skin layer less than 500 nm and a porous layer with thickness less than 200 nm. Also, the same thickness of an asymmetric membrane has a higher permeability compared to a symmetric membrane. In filtration, the thinner membrane has a higher permeation rate which goes to show that the membrane thickness is inversely proportional to the permeation rate. Also, the advantage of the thin membrane is the reduction in energy consumption [13-16].

Although, various methods are employed to fabricate polymeric membranes, the asymmetric porous PES membranes are fabricated by non-solvent induced phase inversion/ separation (NIPS) method. This method is mainly based on separation of solvent and non-solvent of dope (polymer)

solution producing a porous polymer membrane. Most of the commercial and lab membranes are prepared with this method [17]. The morphology of polymer membrane in NIPS method depends on demixing of two solvents. The coagulation medium and temperature, evaporation time and dope composition are the parameters required to control the solvent exchange rate in a NIPS method. NIPS method produces asymmetric polymer membranes with dense skin layer and porous sub layer [18].

2.1.3 Surface Charge of Membranes

The surface charge measurement of polymeric membranes is named zeta potential. The value of zeta potential determines the stability, membrane performance and the extent of fouling [19-21]. If zeta potential value is higher, then the membrane is less prone to fouling due to repulsion between negative surface charges of polymer membrane and hydrophobic foulants such as proteins. The higher zeta potential also means higher stability and higher membrane performance overall. The zeta potential measurements can be done on both the colloidal suspensions and solid membranes [22, 23].

2.1.4 Antifouling Phenomena

Fouling is a phenomenon that is caused by adsorption of deposition of colloids, salts, particles, and macromolecules on the surface, pore walls and inside the pores of the polymer membranes. Therefore, antifouling is a system that prevents these contaminants to attach to the surface of polymers [24, 25].

Fouling can be reversible or irreversible based on bound strength of the foulants. If the bounds are weaker, then reversible fouling occurs and the membrane can be cleaned by hydraulic cleaning [26-28]. However, some foulants are attached to the surface of membranes strongly due to higher affinity towards the membrane surface causing irreversible fouling. This type of fouling can only

be cleaned by chemical cleaning which negatively affects the performance quality and durability of the membrane [29].

Fabricating antifouling polymeric membranes is a crucial factor in water treatment applications. Introducing hydrophilic additives to the membranes improves the hydrophilicity of the membranes reducing its interactions with hydrophobic foulants. The TiO_2 material in general is known for its antifouling properties and high adsorption capacity. In this chapter, we present a work based on discrete TiO_2 nanotube incorporated PES polymers for water treatment application [30, 31]. Although, TiO_2 nanoparticles have been used as hydrophilic nanofillers in PES polymer, to the best of our knowledge, discrete TiO_2 nanotubes fabricated with electrochemical anodization method as nanofillers have been reported for the first time here. To date, only carbon nanotubes have been used to modify PES membranes as a new generation nanocomposite membranes by replacing the nanoparticles used before [32-34]. To the best of our knowledge, although 8° to 15° are the best results for hydrophilic change in contact angle measurements for carbon nanotube modified membrane, the discrete TiO_2 nanotubes results in 27.7° hydrophilic change improving the antifouling property of the PES membrane significantly. The rest of this chapter is based on the specific details of the water treatment application and presents all the results and discussion [35-37].

2.2 Discrete TiO_2 nanotube incorporated PES Membranes for water treatment

Polyethersulfone (PES) is a polymeric permeable material mostly used for the fabrication of ultrafiltration (UF) membranes due to its high thermomechanical and chemical stability. However, the hydrophobic nature of PES membranes renders it prone to fouling and therefore restricts the practical applications of PES in the fabrication of water treatment membranes. The present study

demonstrates a non-solvent induced phase separation (NIPS) approach to modifying the PES membranes with different concentrations of discrete TiO_2 nanotubes (NTs). The zeta potential and contact angle measurements exhibited enhanced hydrophilicity and surface negative charge of TiO_2 NTs/PES nanocomposite membranes compared to unmodified PES membranes upon the addition of nanocomposites. To discern the antifouling and permeation properties of the TiO_2 NTs/PES membranes, steam assisted gravity drainage (SAGD) wastewater obtained from the Athabasca oil sands of Alberta was used. The TiO_2 modified polymer nanocomposite membranes depicted a higher organic matter rejection and water flux than the unmodified PES membrane. The improved surface chemical attributes of the TiO_2 NTs/PES nanocomposite were assumed to be responsible for excellent antifouling nature. The addition of discrete TiO_2 NTs at 1 wt. % afforded maximum water flux (82 LMH at 40 psi), organic matter rejection (53.9%) and antifouling properties (29% improvement in comparison to pristine PES membrane). An enhancement in fouling resistance of TiO_2 NTs/PES nanocomposite membranes was observed in flux recovery ratio experiments.

2.2.1 Introduction

Water sources such as lakes, groundwater and rivers have been mostly contaminated by industrial waste disposal directly or indirectly [38]. The shortage of clean water continues to increase due to which improved water usage efficiency is of paramount importance. Various methods have been explored for water recycling that is both more energy efficient and environmentally sustainable [39, 40]. Filtration using polymeric membranes for wastewater has seen increased adoption recently due to cost efficiency, low energy consumption, reliability and ease of contaminant removal without using harmful products and no phase change at room temperature operations in comparison to other methods of water recycling [41-45].

Polymers are economical materials that can be used for large-scale membrane fabrication and are easy to modify as needed [46]. Among all the other polymers, polyethersulfone (PES) is the most common polymeric materials used for filtration applications due to its excellent thermomechanical, chemical, and contaminant separation properties [47-50]. However, the hydrophobicity of PES results in poor performance of membrane which could hinder its anti-fouling properties negating many of its advantages during the filtration process [49]. Such poor anti-fouling properties have a detrimental effect on the permeation properties which causes a decrease in lifespan of the membrane resulting in an increase of operation cost [51]. Surface modified ultrafiltration (UF) membranes have been explored significantly to enhance the anti-fouling properties of the PES membrane by increasing the hydrophilicity and decreasing the surface charge as these parameters can have significant positive effects on the initial stages of fouling [48,52,53]. A variety of methods such as chemical grafting [54], the addition of antifouling blending materials [55], surface coating and ultraviolet plasma treatment [56, 57] have been explored to fabricate anti-fouling surfaces.

Currently, much research and development are underway on the surface modification of membranes by the incorporation of hydrophilic nanostructures into the PES polymer to fabricate polymer nanocomposite membranes with higher surface hydrophilicity, increased anti-fouling properties and enhanced separation performance [58, 59]. Numerous studies investigated the effect of various nanostructures including porous nanostructures such as carbon nanotubes (CNTs), graphene oxide, zeolites and mesoporous silica and nonporous metal/metal oxides particles such as Ag, TiO_2, MgO, ZnO, Al_2O_3, ZrO_2, Fe_2O_3, and SiO_2 on the structural morphology, transport properties and surface characteristics of the fabricated nanocomposite membranes [60–64]. Among different nanostructures, TiO_2 has received significant attention due to its stability, non-

toxicity, and natural abundance for a variety of applications such as batteries, cosmetics, photocatalysis, pollutant degradation, gas sensing and painting [65].

In the present study, the effect of incorporation of different concentrations of discrete TiO_2 NTs on the physicochemical characteristics and permeation properties of the polyethersulfone (PES) membranes are reported. TiO_2 nanotubes are synthesized by the electrochemical anodization process and can be tailored to have cylindrical or square pores, with tunable diameters from ~ 10 - 1000 nm [66-68]. In addition, bare TiO_2 nanotubes are superhydrophilic and can be rendered amphiphobic if needed by suitable surface functionalization [69].

The nonsolvent-induced phase separation (NIPS) method was used to fabricate TiO_2 NTs incorporated PES membranes. The morphology of structures, chemical compositions and surface properties of the synthesized membranes were investigated by field emission scanning electron microscopy (FESEM), Atomic Force Microscopy (AFM), Fourier-transform infrared spectroscopy (FTIR), surface zeta potential, and water contact angle measurements. Water flux, organic matter rejection and fouling resistance of the TiO_2 NTs incorporated PES membranes were studied using both real and synthetic produced water and were compared with unmodified PES membrane.

2.2.2 Materials and Methods

2.2.2.1 Chemical and Reagents

The ultrafiltration membranes were made using the PES polymer with a molecular weight of 58 kDa obtained from BASF. Polyvinylpyrrolidone (PVP) (MW: 360 kDa) was procured from Sigma Aldrich and used as an additive. Potassium chloride (KCl) and N, N-dimethylacetamide (DMA)

were purchased from Fisher Scientific. The discrete TiO_2 NTs were synthesized using an electrochemical anodization process followed by sonication for discretization. Diethylene glycol (DEG) and Ammonium Fluoride (NH_4F) were purchased from Sigma Aldrich to be used as an electrolyte in electrochemical anodization. Octadecylphosphonic acid (ODPA) to functionalize discrete nanotubes was also indented from Sigma Aldrich. An industrial wastewater, produced from steam assisted gravity drainage (SAGD) in Athabasca oil sands industry (Alberta, Canada) was used for the membrane permeation and fouling characteristics tests. The produced water is the feed water to the warm lime softener (WLS) of current SAGD water treatment facilities.

2.2.2.2 Preparation of TiO_2 NTs/PES Membranes

The preparation of TiO_2 NTs / PES membranes consisted of two steps. The first step includes synthesis of TiO_2 NTs via an electrochemical anodization process in DEG based electrolyte using a two-electrode electrochemical cell as shown in figure 2.1. The synthesized TiO_2 NTs on foil were annealed in a furnace at 500 °C for 3 h followed by functionalization with 1 mM ODPA solution overnight (figure 2.2). The TiO_2 NTs were discretized in 8 mL DMA using a probe sonicator. Different concentrations of discrete NT solutions were made to test the effect of concentration of nanomaterials on PES membrane structure and permeation properties.

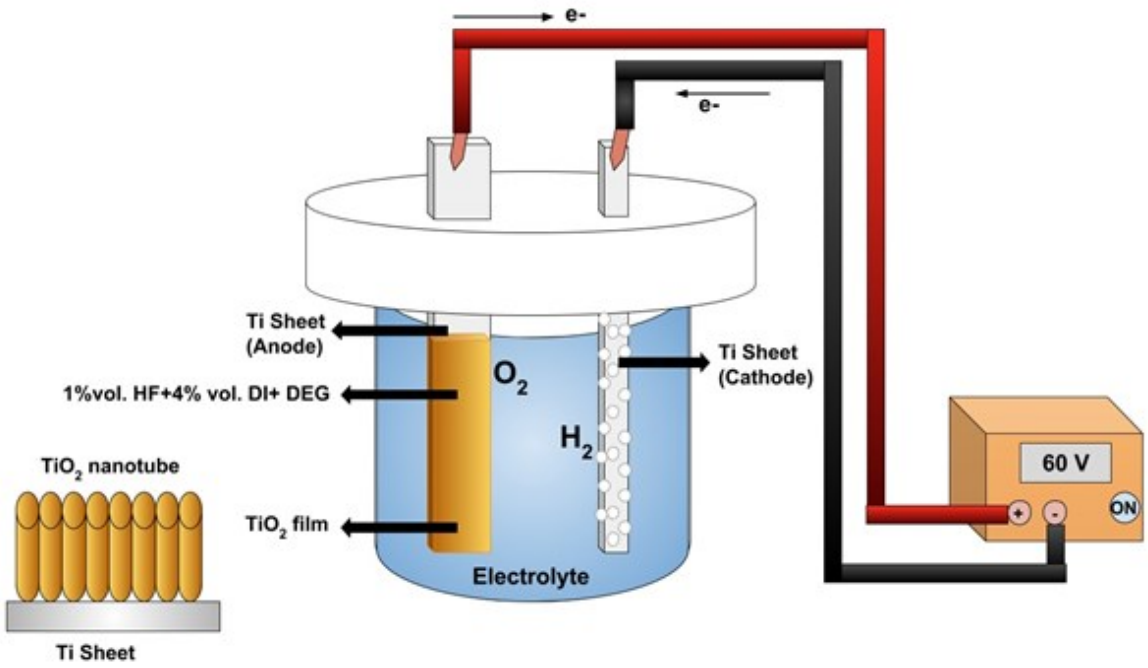

Figure 2.1. Electrochemical anodization process used to form TiO_2 NTs

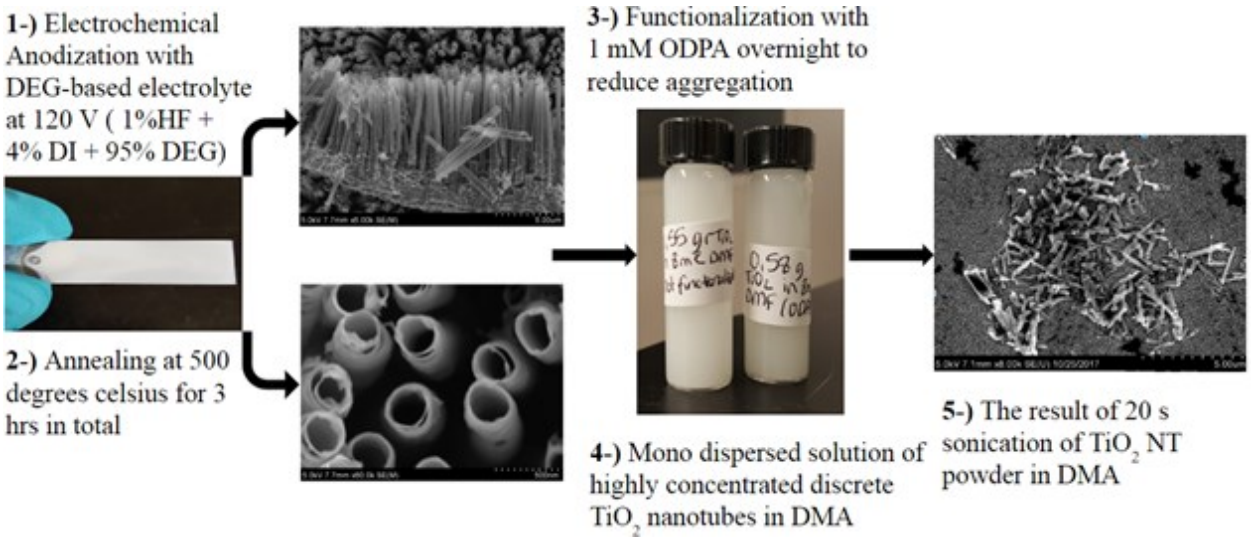

Figure 2.2. Discrete TiO_2 NT synthesis, functionalization and discretization methods explained

The second step, which is shown in figure 2.3, was to fabricate TiO_2 NTs / PES nanocomposite membranes. First, a casting solution was prepared by dissolving desired amounts of PES pellets,

discrete TiO_2 NTs and PVP in DMA solvent. In this work, to produce porous polymer films, homogeneously doped polymer solutions were prepared by mixing DMA with 14 wt.% PES, 2wt% PVP and various ratios of discrete TiO_2 NTs to polymer (1 wt.%, 0.5 wt.% and 0.25 wt.%). Next, a probe sonicator was used to disperse the discrete TiO_2 NTs in DMA uniformly. PVP and PES mixture was then added to the discrete TiO_2 NT/DMA solution and stirred overnight at 100 rpm. The obtained mixture which is also called dope solution was kept at room temperature for 24 h to remove air bubbles from casting solution and to produce a defect-free membrane. A film applicator (Gardco, MICROM II) with a clearance gap of 190 μm and a casting speed of 5 mm/s was used to cast the solution on a flat glass surface. The film was then immersed in DI water and the membrane formation was completed after 24 h by liquid-liquid demixing.

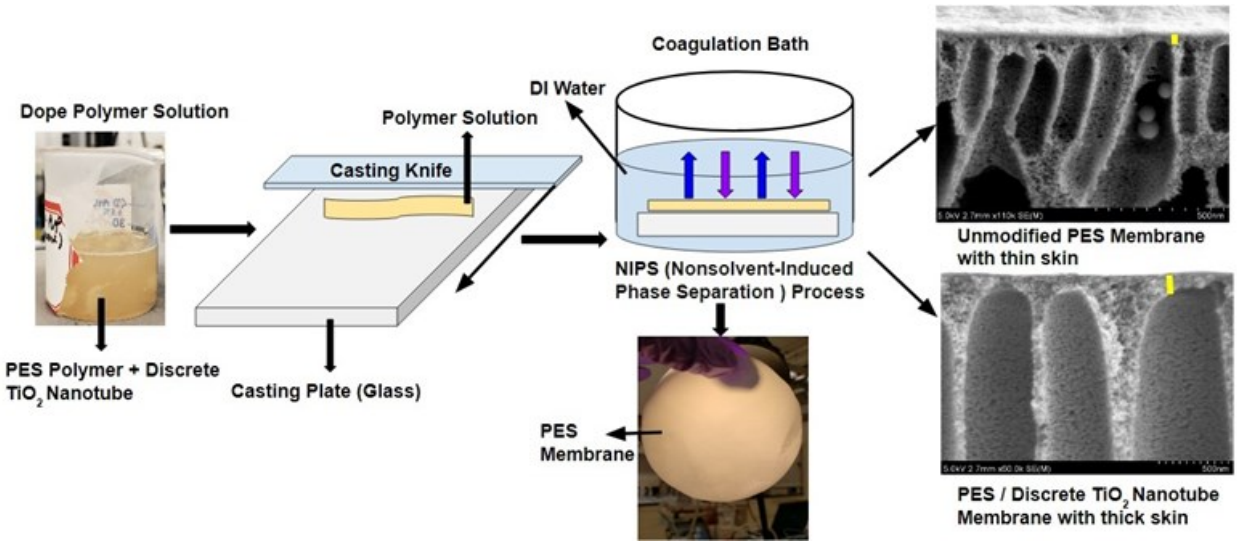

Figure 2.3. Fabrication process of TiO_2 NTs / PES nanocomposite membranes

2.2.2.3 Measurements of Porosity and Pore Size

The average pore size of the membrane was measured using the following expression below which was proposed by Guerout-Elford-Ferry [1]:

$$r_m = \sqrt{\frac{(2.9-1.75\varepsilon)8\eta l Q}{\varepsilon A \Delta P}} \quad (1)$$

Where Q is the permeate volumetric flow rate (m^3/s), η is the water viscosity which is 8.9×10^{-4} Pas at 25 °C and ΔP is the transmembrane pressure (Pa). The applied transmembrane pressures in this study were 10, 20, 30 and 40 psi.

Average porosity of membranes which is the ratio of total pore volume to the volume of the membrane was calculated using the gravimetric method [39]. The following equation was used to calculate the porosity of a membrane. To calculate the average porosity of each membrane the measurements were repeated 3 times.

$$\varepsilon = \frac{w_1 - w_2}{Al\rho} \quad (2)$$

Where w_1 and w_2 are mass of wet and dry membranes (g) respectively, ρ is the water density (0.997 g/cm^3 at 25 °C), l is the membrane thickness (cm), and A is the surface area (cm^2) of the membrane.

2.2.2.4. Pure Water Flux Measurement

A dead-end filtration cell setup consisted of a membrane with an area of 41.8 cm^2 and a dead-end stirred cell (Amicon, UFSC40001) with a capacity of 400 mL. To monitor and record the permeate water flux over time, a digital balance (ME 4002, Mettler Toledo, USA) connected to a computer was employed. Various transmembrane pressures were applied using the pressurized

nitrogen gas. The solution in the dead-end cell, in this case, the DI water was stirred at a rate of 80 rpm. The equation below was used to calculate the water flux (J_0):

$$J_0 = \frac{W}{A\Delta t} \quad (3)$$

Where A is the membrane effective area (m^2), w is the mass of the permeate water (kg), and t is the permeation time (h).

2.2.2.5. Fouling Tests

The fouling tests consisted of a three-step experimental procedure. The pure water flux, J_{W1}, was first measured. The, J_{WF}, water flux during the filtration of WLS inlet water, was then recorded. Lastly, the pure water filtration after hydraulic washing of the membrane surface with DI water for 15 min was performed and the pure water flux of the cleaned membrane J_{W2} was measured again. Based on these fouling tests, the fouling evaluation parameters namely total flux decline ratio (DR_t), the sum of the reversible flux decline ratio (DR_r), irreversible flux decline ratio (DR_{ir}) and flux recovery ratio (FRR) were calculated using the equations below [40,41]:

$$DR_t = 1 - \frac{J_{wF}}{J_{w1}} \quad (4)$$

$$FRR = \frac{J_{w2}}{J_{w1}} \quad (5)$$

$$DR_r = \frac{(J_{w_2} - J_{wF})}{J_{w1}} \quad (6)$$

$$DR_i = 1 - \frac{J_{w2}}{J_{w1}} \quad (7)$$

The total organic carbon (TOC) in the WLS inlet water was measured using a TOC analyzer (Shimadzu, model TOC-V; detection range 3-25000 mg/L). The TOC analyzer measures the level of the organic contaminants or organic molecules in purified water and in this work the concentration of organic carbon atoms covalently bonded in the organic molecules of the PES based membranes was detected by the TOC analyzer. This parameter can be used to test the efficiency of the treatment process. The rejection of the organic matter can also be calculated using the measured TOC concentrations of the permeate (C_P) and feed (C_F) solutions. The rejection was calculated using the equation below:

$$R = \left(1 - \frac{C_p}{C_F}\right) \times 100 \qquad (8)$$

2.2.2.6. Chemical Composition Test (FTIR)

The TiO_2 NTs were functionalized to improve the monodispersity of the discrete TiO_2 NTs in DMA. To verify the functionalization of TNTAs with ODPA, The IR active vibration of material was investigated with the help of Fourier transform infrared (FT-IR) spectroscopy recorded on a Digilab (Varian) FTS 7000 FT-Infrared Spectrophotometer equipped with a UMA 600 Microscope and ZnSe ATR accessory. The sample was scratched from the surface and deposited directly on the ZnSe crystal and nitrogen gas flow was maintained through the ATR assembly. The spectra were accumulated by averaging 64 scans in the frequency range of 850–4000 cm^{-1}.

2.2.2.7. X-Ray Photoelectron Spectroscopy (XPS)

X-ray photoelectron spectroscopy (XPS) was used to determine the surface and subsurface (up to ~10 nm) chemical composition and oxidation state of materials using an Axis-Ultra, Kratos Analytical instrument equipped with a monochromatic Al-Kα source (15 kV, 50 W) with photon

energy of 1486.7 eV under ultrahigh vacuum (~10^{-8} Torr). The binding energy of adventitious carbons C1s peak at ≈ 284.8 eV was used as standard (carbon correction) to assign the peak of other elements. The raw spectra in .vms format were deconvoluted into various peak components using CasaXPS and exported data was plotted in origin 2018.

2.2.2.8. Surface Properties (Wettability and Surface Charge)

Surface wetting characteristics of the fabricated membranes with various concentrations of discrete TiO_2 NTs were measured using contact angle analyzer (FTA-200 Edmonton, CA). DI water was used as a drop method to measure the contact angle. The lower the wettability of the membrane, the higher is the contact angle.

The Surpass3 zeta potential analyzer was used to analyze the charging behavior of the membrane surface when in contact with a liquid such as DI water. The surface zeta potential is derived from a flow of potential which arises from the interaction between the motions of liquid relating to the solid surface. The zeta potential values were obtained using various pH values (5, 6, 7, and 8) at 25 °C using 0.001 M KCl solution.

2.2.2.9. Membrane Morphology Study

The morphologies and cross-sections of the dried membranes were studied using the field emission scanning electron microscopy (Hitachi S-4800 Field Emission SEM (FE-SEM)). The conductivity of the membranes was improved by sputtering 10 nm of gold on the surface of the membrane using Denton Gold Sputterer Unit (for SEM). A high vacuum with 5 kV/20 µA condition was used to image the cross-sectional structure of the prepared nanocomposite membranes.

2.2.2.10. AFM (Atomic Force Microscopy)

Atomic Force Microscopy (AFM, Bruker, The Dimension Fast Scan Atomic Force Microscope, Santa Barbara CA, USA) was used to image the surface topography of the TiO_2 NTs / PES nanocomposite membrane.

2.2.3 Results and Discussions

2.2.3.1 FTIR Measurement Results

A vibrational spectrum of ODPA monolayer functionalized TiO_2 nanotubes was collected to validate the successful chemical functionalization of TiO_2 NTs surface with ODPA molecules (figure 2.4a). The FTIR spectrum of ODPA functionalized TiO_2 exhibits a characteristic IR absorption band at 2848 and 2917 cm^{-1} due to symmetric and anti-symmetric C–H stretching vibrations of CH_2 in alkyl chain of ODPA [69]. The IR peak at 3019 cm^{-1} was derived from C-H stretch of terminal methyl ($-CH_3$) groups. Further, the peak observed at 3320 and 1605 cm^{-1} was assigned to O-H stretch and bending vibration of surface adsorbed water, respectively. Additionally, various peaks corresponding to symmetric and asymmetric bending vibration of CH_2 and CH_3 groups in ODPA were observed at 1492 cm^{-1} (CH_2+CH_3 bend), 1450 cm^{-1} (CH_2 in-plane bend) and 906 cm^{-1} (C-H out of plane bend) confirming the presence of ODPA molecule on the surface of TiO_2 nanotubes. The IR spectrum of ODPA functionalized TNTAs in the frequency range 850-1300 cm^{-1} shows various IR bands at1265, 1152, 1065 and 1027 cm^{-1} assigned to P=O vibration, PO_3 asymmetric stretch, PO_3 symmetric stretch and P-O-(H) symmetric stretch respectively. The presence of these IR bands clearly demonstrates successful chemical functionalization of TNTA with OPDA *via* reaction between -OH group on the surface of TiO_2 and phosphonate group ($-H_2PO_4$) on ODPA to form phosphonate ester linkage ($ROPO_2$–) [70, 71].

2.2.3.2 XPS Results

The oxidation state and surface chemical attributes of ODPA functionalized TiO_2 nanotubes were determined using X-ray photoelectron microscopy (XPS) (figure 2.4b and 2.5a-d). The appearance of C1s, O1s, Ti2p, P2p peaks in XPS elemental survey scan of ODPA functionalized TiO_2 nanotubes demonstrate successful functionalization of TiO_2 nanotubes with carbon and phosphorous rich organic molecules. The signal intensity of C1s peak was much higher agreed with a high concentration of carbon at the surface of TiO_2 due to better coverage with ODPA monolayer (figure 2.5b). High-resolution XPS spectra (HR-XPS) of ODPA functionalized TiO_2 nanotubes in Ti2p region show two peaks components located at a binding energy (BE) 458.8 and 464.6 eV, originated due to $Ti2p_{3/2}$ and $Ti2p_{1/2}$ peak components of Ti^{4+} state in TiO_2 crystal lattice (figure 2.5a) [80,81]. The peak separation of 5.8 eV between $Ti2p_{3/2}$ and $Ti2p_{1/2}$ peaks and their respective positions validate O^{2-} coordinated Ti^{4+} in tetragonal anatase phase TiO_2 [82]. Core-level HR-XPS spectra of ODPA functionalized TiO_2 nanotubes in O1s region can be deconvoluted into three peak components centered at BE ≈ 530.4, 531.5 and 532.7 eV (figure 2.5b). The peak component at BE value 530.4 eV was originated from contribution from Ti coordinated oxygens (O^{2-}—Ti^{4+} forming TiO_6 octahedron) present in crystal lattice of TiO_2 and P=O of surface adsorbed ODPA molecule while intense peak at BE ≈ 531.5 eV was corroborated to non-lattice adventitious oxygens (-OH groups) and P-O oxygen of ODPA molecule (figure 2.5b) [83, 84]. Relatively small peak component at 532.7 eV was assigned to adventitious carbon bonded oxygens (C=O). Deconvoluted HR-XPS spectra of ODPA functionalized TiO_2 nanotubes in the C1s region gave two peak components, at 284.8 and 286.3 eV (figure 2.5c). The major peak component at 284.8 eV was originated from sp^3 hybridized carbons composing alkyl chain of ODPA while less intense shoulder peak at 286.3 eV was arising from contribution of C-OH/C-P type carbons [85,86] Additionally, a single peak at BE ≈134.1 eV, in HR-XPS of ODPA grafted TiO_2 nanotubes in P2p

region was assigned to phosphorous in phosphonate group (P-O) bonded to TiO_2 confirms successful grafting of ODPA on TiO_2's surface (figure 2.5d) [87].

2.2.3.3. Surface and Cross Section Morphology

The membranes were immersed in liquid nitrogen for a few seconds to get a clear cut before preparing the samples for the internal cross-sectional imaging. The images of the unmodified PES membrane and the TiO_2 NTs incorporated PES membranes are presented in figure 2.6 for a comparison. The PES membranes used for microfiltration (MF) and UF purposes have a common trait which is having a porous finger-type asymmetric structure due to the top dense skin layer [72,73]. Figure 2.6 shows this very clearly in all the membrane cross-sectional images. According to figure 2.6, the addition of discrete TiO_2 NTs to unmodified PES membrane decreased the thickness of the membrane. However, the average skin thickness of the membranes increased as the concentration of discrete TiO_2 NTs increased. A possible explanation is that the addition of the discrete NTs slows down the solvent/non-solvent exchange rate in coagulation bath and this causes the formation of thinner membranes with thicker skin layer due to the entrapment of more discrete TiO_2 NTs at the top surface during phase separation [74, 75]. The discrete TiO_2 NTs are hydrophilic additives and tend to enhance thermodynamic instability of the casting solution that accelerates the exchange of solvent and non-solvent [72]. Also, due to the high surface area of discrete TiO_2 NTs and their superhydrophilic properties, the swelling of the polymer film by hydrophilic nanotubes before its solidification allows more non-solvent to flow into the casting film during NIPS process and thus tends to increase in thickness of the membrane. However, an increase in the viscosity of the casting solution due to addition of discrete TiO_2 NTs has reversed

these effects. As a result, the mutual diffusivities between non-solvent and solvent were reduced causing a decrease in the membrane thickness

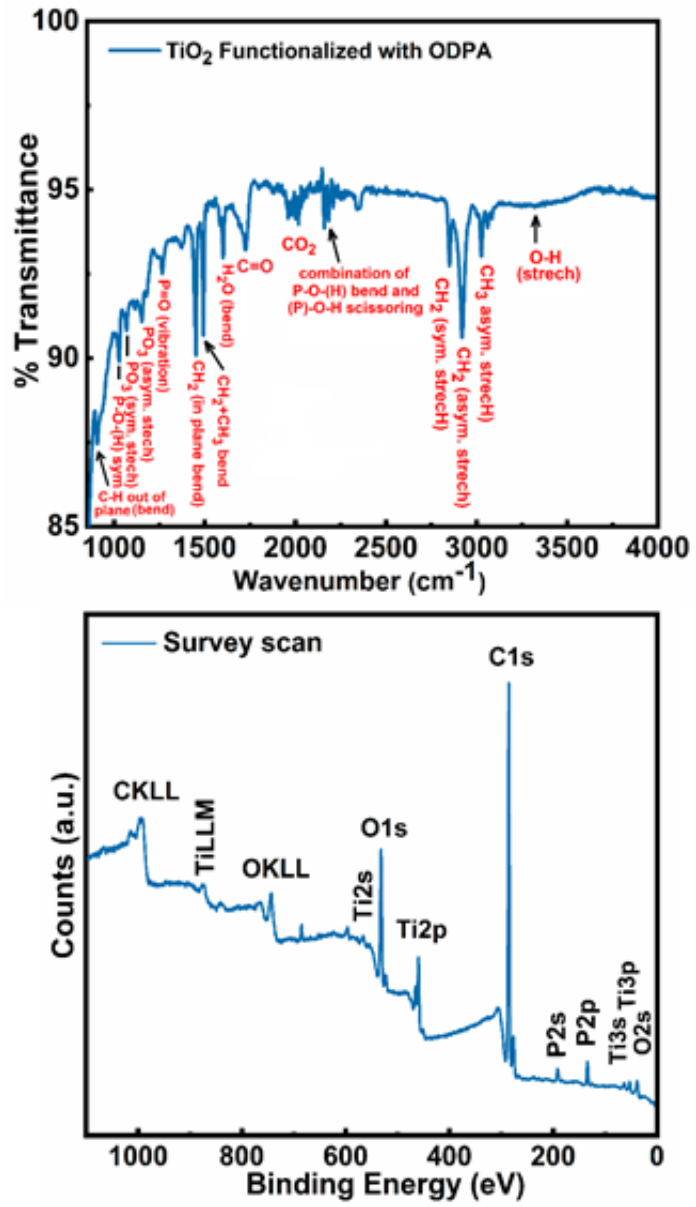

Figure 2.4. (a) FTIR spectra of ODPA functionalized TiO_2 NTs. **(b)** XPS elemental survey scan of ODPA functionalized TiO_2 nanotubes

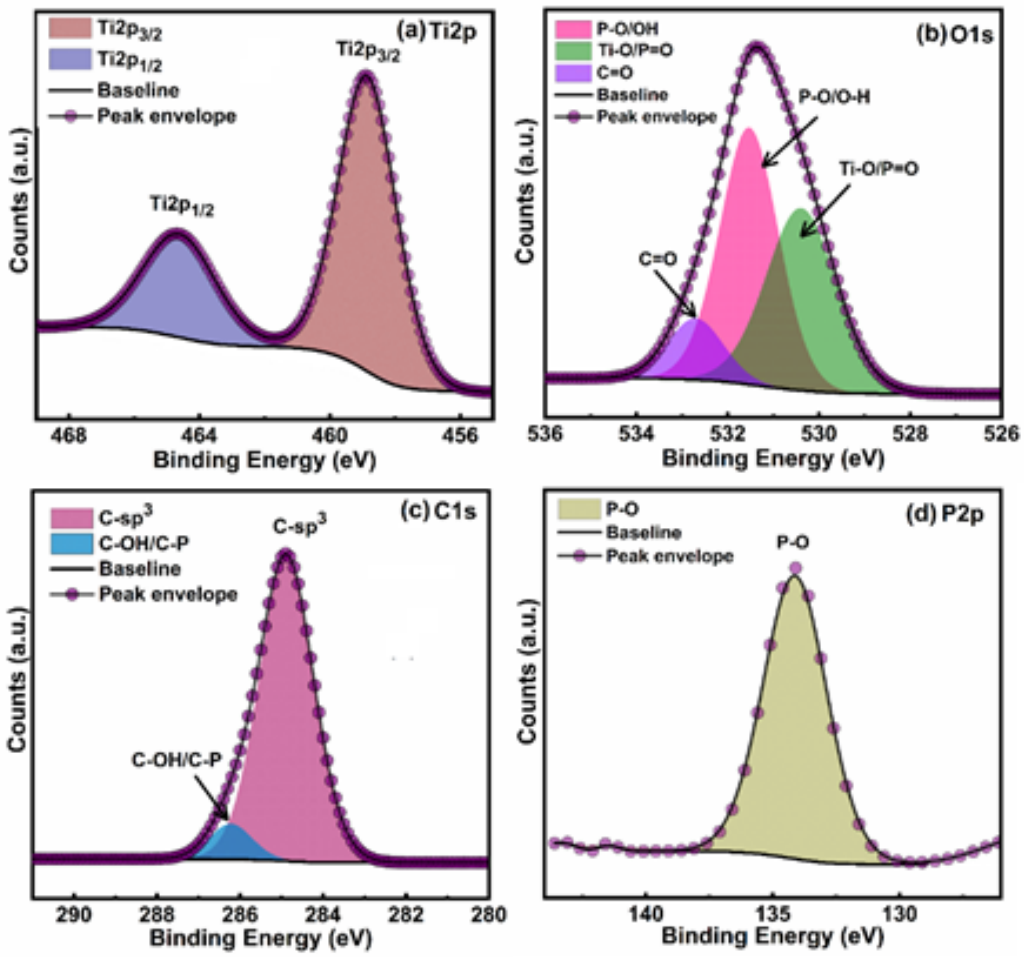

Figure 2.5. Core-level HR-XPS spectra of ODPA functionalized TiO_2 nanotubes in **(a)** Ti2p region, **(b)** O1s region. **(c)** C1s region and **(d)** P2p region.

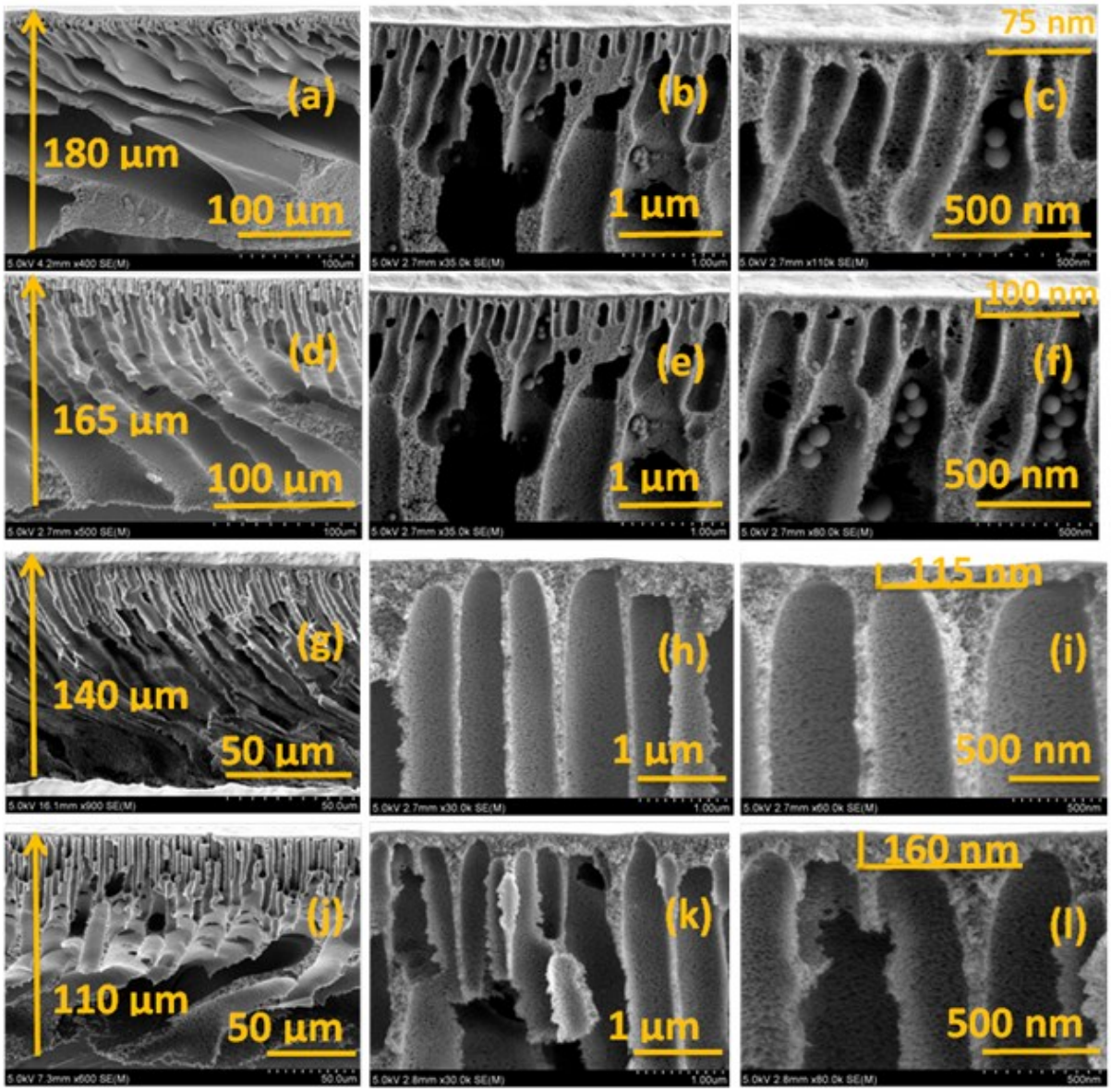

Figure 2.6. The cross-sectional SEM images of pristine PES and TiO_2 NTs/PES nanocomposite membranes. **a)** Pristine PES membrane **d)** 0.25% TiO_2 / PES membrane **g)** 0.5% TiO_2 / PES membrane **j)** 1% TiO_2 / PES membrane.

2.2.3.4. Atomic Force Microscopy (AFM)

Roughness is a direct metric of surface topography which can be measured with AFM. According to the images in figure 2.7, the surface roughness increased with increasing the concentration of discrete TiO_2 NTs in PES membranes. The surface roughness of pristine PES, 0.25% TiO_2/PES, 0.5% TiO_2/PES and 1% TiO_2/PES were measured to be 57.1 nm, 83.3 nm, 121 nm and 133 nm, respectively. The PES membrane with 1% discrete TiO_2 NTs had the highest surface roughness. This membrane also had the lowest contact angle meaning that a part of improved wettability of nanocomposite membranes can be attributed to the increased roughness. According to the Wenzel equation, a membrane that is slightly hydrophilic becomes more hydrophilic as the surface roughness increases. In addition, based on Table 1, 1% TiO_2/PES membrane was more negatively charged (-32.0±0.6 mV) which proves the intended material improvement, e.g., addition of TiO_2 NTs to increase the hydrophilicity of the membranes.

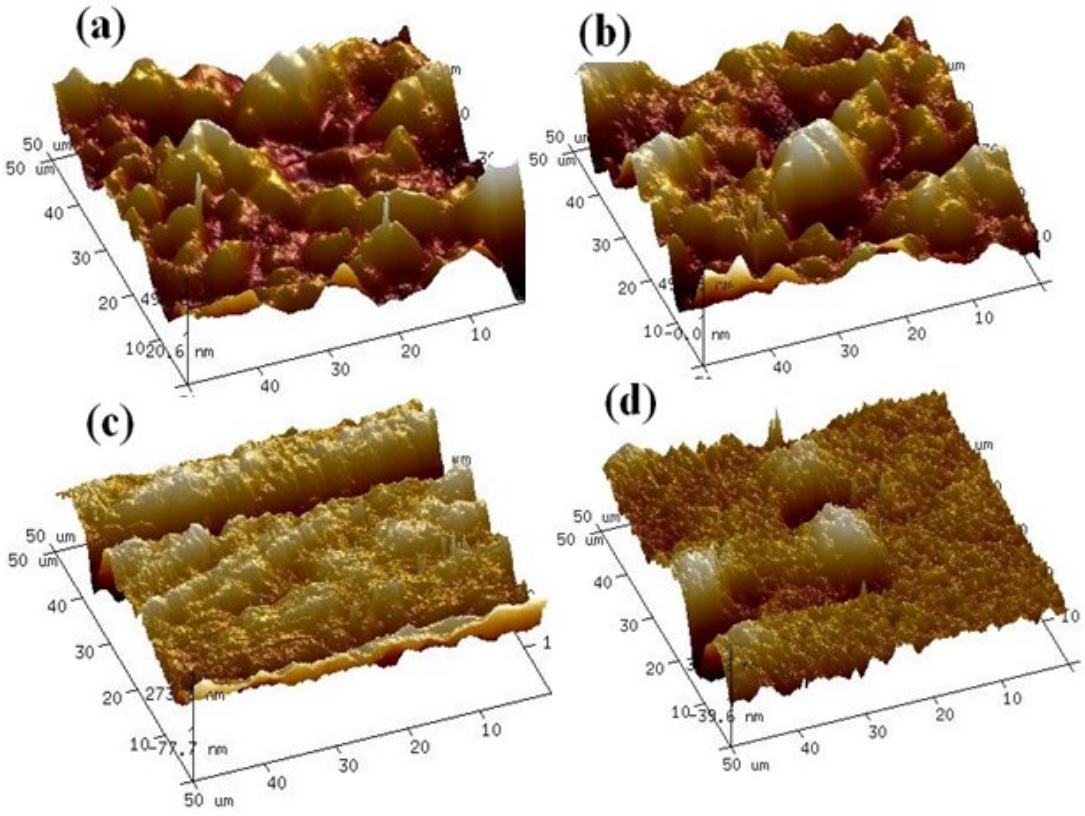

Figure 2.7. Topography of discrete TiO_2 based PES membranes using Atomic Force Microscopy. **a)** 1% TiO_2 / PES membrane **b)** 0.5% TiO_2 / PES membrane **c)** 0.25% TiO_2 / PES membrane **d)** Pristine PES membrane

2.2.3.5 Contact Angle Measurement Results

Water contact angle analysis is a technique to study the hydrophilic properties of synthesized membranes. In general, a higher contact angle means that the membrane is more hydrophobic, and a lower contact angle reveals more hydrophilicity and higher surface energy of the membrane. A syringe which was positioned above the sample surface was used to deposit water droplets with a volume of 1 µL and a high-resolution camera was used to capture the side image of the droplet. The angle of the image was then analyzed using a protractor to measure the contact angles. For each membrane, three different measurements were taken from various spots on the membrane and the average values were reported. The contact angles of the membranes are presented in Table 1. The contact angle of the bare PES membrane was 65±2^o and as the concentration of discrete TiO_2 NTs increased from 0.25% to 1%, the contact angle was observed to decrease from 49±1^o to 37±1^o. The contact angle of the bare TiO_2 NTs was measured to be 8.0±2^o which is highly hydrophilic compared to PES membrane. The accumulation of hydrophilic discrete TiO_2 NTs on the surface during phase inversion process reduced the interface energy. Based on contact angle measurements, the addition of discrete TiO_2 NTs to PES membranes leads to the formation of more hydrophilic membranes. More hydrophilicity of MF/UF membranes can be correlated with their antifouling properties as will be discussed later.

2.2.3.6. Membrane Surface Charge Results

The nature of surface charge on the membrane is a crucial parameter which governs the hydrophilicity and longevity of the membrane. The incorporation of discrete TiO_2 NTs in TiO_2 NTs/ PES increases the hydrophilicity due to the lowering of the surface free energy which concomitantly reduces fouling of the PES membranes. The contact angle measurements and the surface charge of the membranes are presented in Table 1. The PES polymer consists of polyetherphenylsulfone backbone with pendant sulfonate ($-SO_3H$) groups and numbers of the sulfonic acid group are dependent on the degree of sulfonation. At pH values higher than the isoelectric point (IEP), the sulfonate groups in PES polymer get dissociated into negatively charged ($–SO_3^-–$). Due to low dissociation constant (pKa), the sulfonate groups readily get dissociated in water at pH-7, which gave them surface negative charge as observed from zeta potential measurement. In the pristine PES material, a certain fraction of sulfonates functionalities remains undissociated due to strong hydrogen bonding and inaccessibility of solvent. The incorporation of discrete TiO_2 NTs, the membrane surface becomes more accessible to solvents which facilitate dissociation of sulfonic acid groups and increase negative change. Additionally, TiO_2 also introduce readily ionizable surface functional groups such as hydroxyl and carboxylic groups, which also contribute to the total surface negative charge of the composite. As the pH of the solution is increased, more carboxylic (-COOH) and hydroxyl (-OH) get deprotonated to negative charges $–COO^-$ and $–O^-$ groups and become the source of electric charge resulting in a more negatively charged membrane [77]. The PES membrane with 1 wt. % TiO_2 NTs is more negatively charged and is expected to reduce the fouling by organic and inorganic contaminants in the water due to electrostatic repulsion [77].

Table 2.1. Surface Charge of PES Membranes and Contact Angle Measurements Results

Membranes	**Contact Angle**	**Zeta Potential (mV) at pH 5**	**Zeta Potential (mV) at pH 6**	**Zeta Potential (mV) at pH 7**	**Zeta Potential (mV) at pH 8**
Unmodified PES	65.1±2°	-24.2±0.1	-26.6±0.7	-27.5±0.1	-28.0±0.9
Unmodified TiO_2 NT membrane	8.0±2°	-8.3±0.5	-8.8±0.4	-9.2±0.2	-10.1±0.8
PES with 0.25 wt% TiO_2 NTs	49.1±1°	-25.2±0.8	-27.0±0.6	-27.8±0.4	-28.4±0.5
PES with 0.5 wt% TiO_2 NTs	40.5±2°	-26.4±0.7	-27.3±0.4	-28.6±0.6	-29.7±0.8
PES with 1 wt% TiO_2 NTs	37.4±1°	-28.2±1	-29.4±0.4	-31.5±0.3	-32.0±0.6

2.2.3.7 Permeability of Membranes

In asymmetric membranes, there are two layers; the top dense layer which governs the permeation properties and the bottom porous layer which provides mechanical strength. The addition of the inorganic discrete TiO_2 NTs which are polar attract the polar water molecules to the membrane surface which leads to an improvement in pure water flux. The pure water flux graph of pristine PES membrane and nanocomposite PES membranes with 0.25 wt. % to 1 wt. % loading of discrete TiO_2 NTs, as a function transmembrane pressure is shown in figure 2.8a. The hydraulic permeability of the PES based membranes was obtained from the slopes of this figure.

As can be seen in this figure, incorporating discrete TiO_2 NTs has resulted in higher water permeability than unmodified PES membrane. The addition of more hydrophilic hydroxyl groups to the surface of the membrane improved the hydrophilicity (Table 1) which also increased water permeability of the membrane [77]. The nanocomposite membrane prepared by 1 wt. % discrete TiO_2 NTs was found to provide the maximum hydraulic permeability of 1.65 LMH/psi. The extracted hydraulic permeability results from figure 2.8a are shown in figure 2.8b. As can be seen in this figure, increasing the concentration of discrete NTs up to 1 wt. % increased the water permeability. This result can be attributed to a remarkable increase in hydrophilicity of membranes (Table 1). In addition, the overall thickness of membranes was reduced by the incorporation of TiO_2 NTs (figure 2.6), which decreased the resistance of the membranes against water transport.

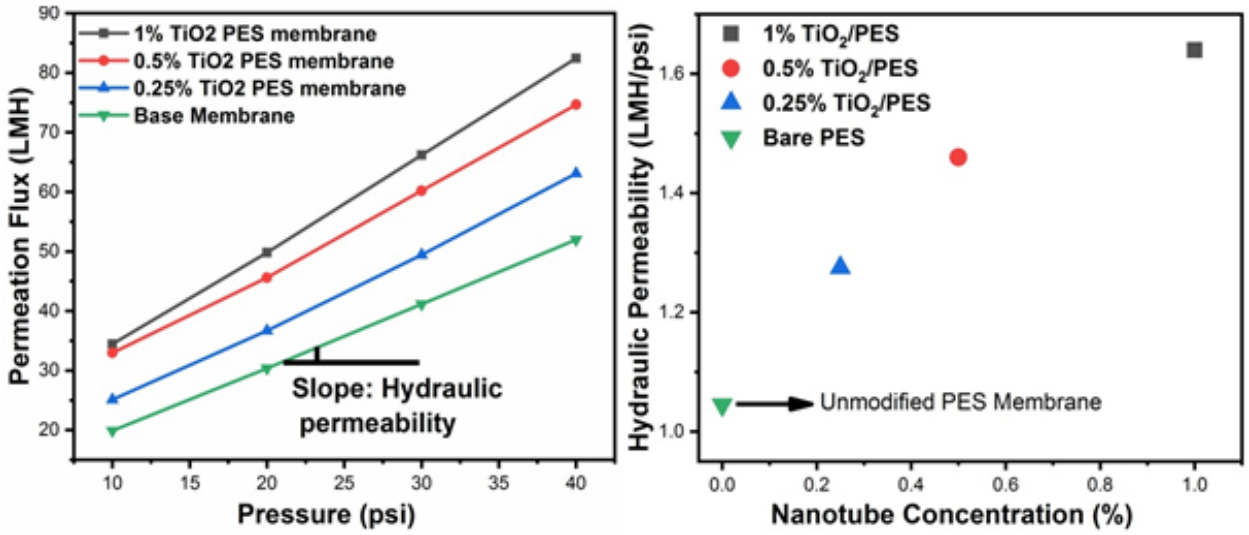

Figure 2.8. a) Permeation flux as a function of transmembrane pressure. **b)** Hydraulic permeability of membranes as a function of NT concentration

2.2.3.8 Porosity and Mean Pore Radius of Membrane

The porosity (%) is the void spaces over the total volume of a polymer matrix and is one of the most important properties of a polymer. The pore size and pore volume are essential parameters to be measured prior to the application of a polymer in various fields. Porosity is measured by

filling the pores either with a liquid or gas. Following the gravimetric method, the wet and dry masses of various membranes were measured, and this is shown in Table 2. The porosity of nanocomposite membranes is shown in figure 2.9. By the addition of discrete TiO_2 NTs up to 1 wt. %, the overall porosity is increased. Theoretically, PVP as an additive to PES increases the thermodynamic instability due to its non-solvent property and kinetic hindrance due to its high molecular weight. As result, this relation between kinetic hindrance and thermodynamic enhancement of the casting solution affects the solidified membranes' functional and structural properties by changing the porosity of phase inversion membranes [78]. The addition of hydrophilic discrete TiO_2 NTs to the polymer solution further decreases its thermodynamic stability. Addition of both PVP and discrete TiO_2 NTs results in thermodynamic variation which enhances the demixing of solution, thus leading to the formation of more porous structures. On the other hand, an increase in the viscosity of casting solution by the addition of TiO_2 NTs can lead to the delayed demixing of solvent and non-solvent and thus formation of denser structures. This implies the presence of an optimum loading of discrete NTs (0.25 wt. % to 1 wt. % TiO_2 NTs) for improving the water flux [78]. The increase in porosity is another parameter that improved the water flux results as shown in figure 2.8. According to figure 2.9, the mean pore size decreased, and the overall porosity increased as the percentage of discrete TiO_2 NTs in membrane increased (see equation 1). The reduced pore diameter can potentially improve the separation properties of the nanocomposite membranes. As mentioned before, the separation properties of membranes are governed by the overall porosity and the membrane thickness and the addition of higher concentration of NTs increases both of these parameters, thus bettering the membrane properties for water treatment applications. In the present study, the main reason for the increase in the removal of organic matter by the addition of 1 wt. % discrete TiO_2 NTs, as will be explained in

the next section, can be due to the increase in the thickness of skin layer (FESEM images in figure 2.6).

Table 2.2. Measured masses of dry and wet membranes for porosity and mean pore radius

Membrane	Mass of Dry Membrane (mg)	Mass of Wet Membrane (mg)
Unmodified PES	14.6±1	502.1±2
PES with 0.25 wt. % TiO_2 NTs	25.0±2	557.5±3
PES with 0.5 wt.% TiO_2 NTs	27.2±2	597.2±1
PES with 1 wt. % TiO_2 NTs	24.2±2	639.2±2

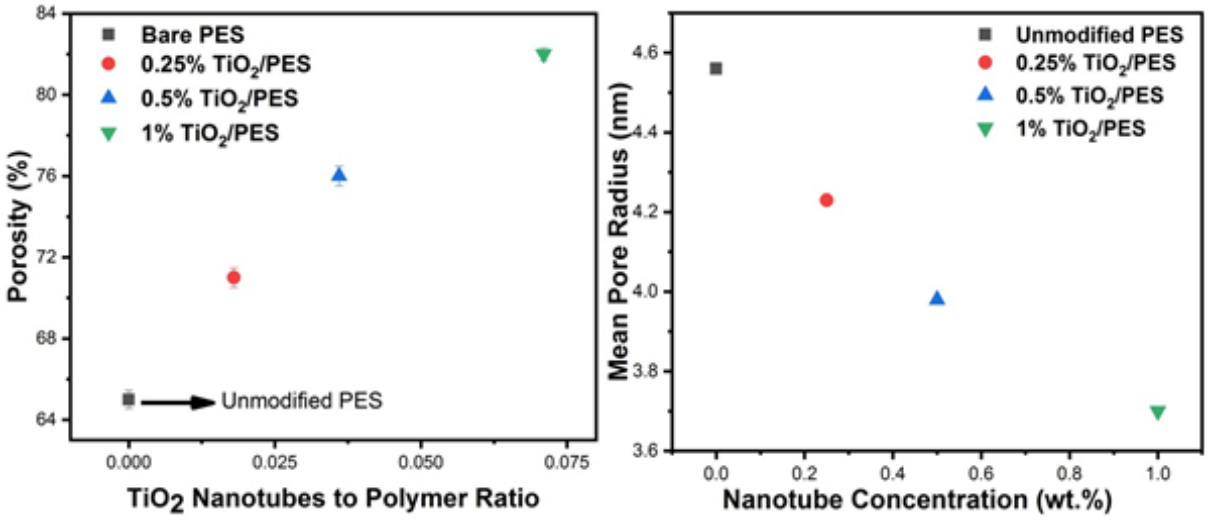

Figure 2.9. Porosity and mean pore radius plots of various membranes.

2.2.3.9 Separation Performance of Membranes

The separation performance of nanocomposite membranes was evaluated by the filtration of WLS feed water. Table 3 presents the organic matter rejection results. A better performance for the removal of organic matter from oil sands produced water was observed for the nanocomposite

membranes when compared with pristine membrane. The TOC rejection increased from 11.7 % (unmodified PES membrane) to more than 50% for 1 wt. % discrete TiO_2 NTs/ PES nanocomposite membrane. Based on the data presented in Fig. 4 and Table 3, the addition of 1 wt. % discrete TiO_2 NT has maximized both water flux (82 LMH at 40 psi) and TOC rejection (53.9%). The rejection was calculated using equation 8 in section 2.5.

Table 2.3. Removal of organic matter from WLS inlet water (TOC: 500 ppm)

	Permeate TOC (mg/L)	**Permeate TC (mg/L)**	**Permeate IC (mg/L)**	**WLS Feed Water Rejection (%)**
Bare PES	441.28	468.74	27.46	11.7
1 wt.% TiO_2/PES	230.70	253.80	23.10	53.9
0.5 wt.% TiO_2/PES	413.51	447.40	33.90	17.3
0.25 wt.% TiO_2/PES	424.23	451.20	26.97	15.15

2.2.3.10 Fouling Characteristics of Membranes

The fouling characteristics of unmodified pristine PES membrane and discrete TiO_2 NTs/ PES nanocomposite membranes during the filtration of WLS feed water is shown in Table 3. To investigate the effect of TiO_2 NTs on flux decline over time, all experiments were conducted at a similar initial permeation flux. Also, in all experiments, the feed solution chemistry, temperature, and hydrodynamic of membrane modules were kept similar. This allowed attributing the fouling propensity of membranes to the surface properties rather than feed properties and hydrodynamic conditions (e.g.; drag force) [76, 79]. The membranes were compressed at high pressure (70 psi)

before the experiments to ensure that the flux decline over time is only due to the fouling of the membranes [58]. At a constant initial flux, the flux decline can be attributed to the hydrophilicity, surface charge, and roughness of the modified membranes [63].

According to the figure 2.10, the flux decline of the unmodified membrane is more than the PES membranes modified with discrete TiO_2 NTs. The PES membrane with 1 wt. % discrete TiO_2 NTs showed approximately 29% more water flux than the unmodified PES membrane after 20 minutes of filtration. It is well known that the membranes with more negative surface charge and higher hydrophilicity have less interaction amongst the functional dissolved organic compounds in the feed solution and the polar groups on the membranes surface. This can be explained by formation of a water layer on the surface of the membrane that hinders foulant attachment to the membrane surface [77, 78] due to the formation of hydrogen bonding among the surface hydrophilic groups to start with. Also, due to the hydrophobic nature of most organic matter in the fluids tested [78] the fouling materials are less inclined to attach to a hydrophilic surface where there is smaller hydrophobic interaction with membrane surface. Membrane surface roughness, characterized by AFM, also plays a significant role in fouling. Foulant materials are entrapped in the edgy zones, behind the peaks and consequently clog the valleys on the surface of MF/UF membranes resulting in significant decrease in permeate flux. In this study, the combination of the hydrophilic surface of TiO_2 NTs-based nanocomposite membranes along with their high surface potential (Table 1) seem to have dominated the roughness effect and made them less prone to fouling by dissolved organic matter, which can be beneficial for oil sands produced water treatment.

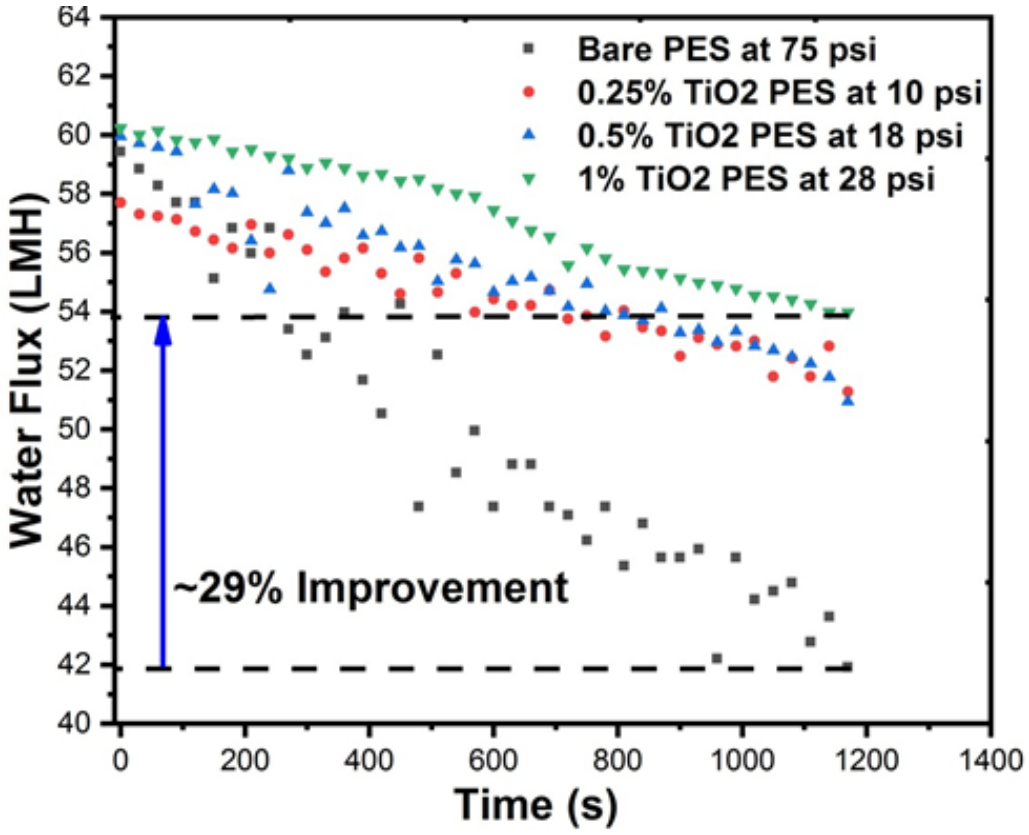

Figure 2.10. Water flux vs. time discrete TiO_2 nanocomposite membranes and unmodified PES membrane due to fouling.

The total flux decline ratio (DR_t), irreversible fouling ratio (DR_{ir}), water flux recovery ratio (FRR), and reversible fouling ratio (DR_r) for the pristine PES membrane and TiO_2 NTs/PES nanocomposite membranes are shown in figure 2.11. The membranes showed flux decline during the filtration of WLS feed water for 20 min, which was possibly due to the existence of inorganic and organic materials on the surface of membranes. TiO_2 NTs with high surface area is great adsorbent materials that adsorb foulants on the surface of the membrane and therefore decreasing the irreversible flux reduction. The DR_{ir} was found to be 12.5%, 11%, and 15% for 1wt%, 0.5 wt. %, and 0.25 wt. % TiO_2 loading as compared to 18% for unmodified PES membrane. The 1 wt. % TiO_2/PES membrane indicated 9% more flux recovery ratio than the pristine PES membrane,

suggesting an improvement in antifouling characteristics of the unmodified membrane by the incorporation of TiO_2 NTs.

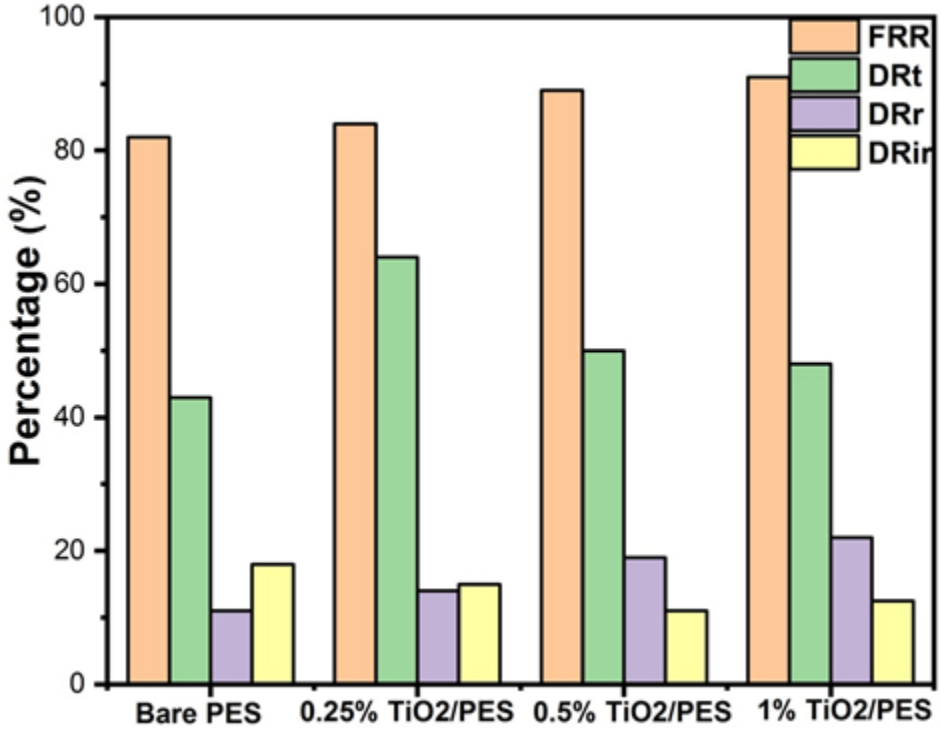

Figure 2.11. Comparisons of fouling characteristics of unmodified PES and PES/ discrete TiO_2 nanocomposite membranes.

2.2.4 Conclusion

In this study, discrete TiO_2 NTs with various concentrations were blended into a polymeric membrane matrix via NIPS technique. The surface properties of the nanocomposite membranes such as negative surface charge and hydrophilicity have noticeably changed to be stronger. The contact angle and zeta potential measurements showed the fabrication of more hydrophilic and negatively charged TiO_2 NTs PES nanocomposite membranes. All discrete TiO_2 NTs incorporated PES membranes showed better organic matter rejection and water flux when compared with the pristine PES membrane. The incorporation of discrete TiO_2 NTs, up to 1 wt. % enhanced the water flux due to an increase in overall porosity and hydrophilicity of the membranes. The most favorable

loading to improve both organic matter rejection and water flux was found to be 1 wt. % TiO_2 NTs incorporated PES membranes which removed 53.9% of dissolved organic matter from SAGD produced water. The SAGD WLS feed water was used to test the fouling propensity of membranes. The results showed that by the addition of discrete TiO_2 NTs, the fouling tendency of the membranes has hindered due to improved surface properties. Discrete TiO_2 NTs at its optimal loading (1 wt. %) has provided the maximum rejection of organic matter (53.9%), water flux (82 LMH at 40 psi), and antifouling properties (29% improvement compared to pristine PES membrane). The flux recovery ratio (FRR) experiments have confirmed notable improvement in the antifouling property of discrete TiO_2 NTs incorporated PES membranes.

As mentioned before, one of the potential benefits of TiO_2 NTs incorporated PES membranes is their low cost compared to other nanomaterials due to their nearly endless lifetime. The low human toxicity, high thermal and chemical stability are also other main advantages of TiO_2 NTs which make them a good material in water filtration processes commercially. This membrane technology can easily be implemented into an existing commercial production facility due to facile synthesis methods of TiO_2 NTs as well as the discrete TiO_2 NTs. Since it is possible to produce discrete nanotubes in large scale, commercial fabrication of nanotube nanocomposite PES membranes will be an easy solution to fouling of membranes in water treatment.

Chapter 3 - All-solution Processed, Scalable Superhydrophobic Coatings on Stainless Steel Surfaces Based on Functionalized Discrete Titania Nanotubes

Stainless steel structures are used in reactor vessels, pipelines, boilers and industrial tubing in the oil and gas industries and they regularly experience corrosion, erosion and fouling that necessitate frequent replacement and repairs. We demonstrate a new method to robustly protect the stainless steel surface and render it superhydrophobic. Our method utilizes self-assembled monolayers (SAMs) of octadecylphosphonic acid (ODPA) grown on discrete TiO_2 nanotube (d-TNT)-coated stainless steel surfaces for complete passivation. While the formation of superhydrophobic coatings based on anodically formed titania nanotube arrays has been previously reported by several research groups including us, the key techno-economic obstacle has been the need to use vacuum deposition to grow adherent and uniform precursor Ti films on non-native substrates such as stainless steel prior to electrochemical anodization. Vacuum deposition of the precursor Ti films is simply neither scalable nor economically feasible for the large and complex stainless steel structures used in pipelines, boilers and industrial tubing and solution processing, preferably a spray-coatable solution, is an absolute must. Our innovation here consists of formulating a spray-coatable suspension of functionalized discrete TiO_2 nanotubes that forms a superhydrophobic surface on stainless steel substrates. Vacuum deposition is completely eliminated from our process sequence and as such, we expect our coatings to inhabit the same niche as current commercial formulations while possessing the superior temperature stability and wear resistance of TiO_2 [61].

3.1 Overview of Superhydrophobic Coatings on Stainless Steel

Stainless steel (SS) is a metal alloy typically consisted of iron, carbon and chromium. Since its discovery in 1905, it has been used in a wide range of applications such as maritime, aviation, petrochemical and construction [1, 2]. The broad range of applications of this metal alloy is due to its combination, high mechanical strength and corrosion resistance. Although SS is relatively corrosion resistant, the surface of SS is subject to corrosion, organic fouling and scale formation which overtime results in loss of thermal conductivity, viscous drag and pits or weakened structural integrity [3]. The lower thermal conductivity in boilers and heat exchangers and increased viscous drag in pipelines can increase the energy costs [4, 5]. However, the formation of superhydrophobic coatings can reduce the corrosion and scaling problems inhibiting the direct contact of SS surface with ions present in aqueous media.

Superhydrophobic (SH) surfaces defined as having a contact angle higher than 150° have been studied extensively over the past decade [6-9]. The SH surfaces have been fabricated on polymers [10, 11], glass [12, 13], fabrics [14] and metals [15]. Amongst these materials, superhydrophobic metal surfaces are of great interest in industrial applications due to their wetting properties such as drag reduction [16-18], corrosion resistance [19] and self-cleaning [20, 21] which require a high contact angle and low drop adhesion (that is defined by a low contact angle hysteresis). Superhydrophobic surfaces with strong chemical inertness based on polytetrafluoroethylene (PTFE) are commercially available. However, they are not suitable and cost effective for large scale applications. Also their poor wear resistance and adhesion to the stainless steel surface lead the scientists to search for new superhydrophobic coating materials. To protect the surface of stainless steel or steel to be used in industrial applications, the cost effective formation of self-assembled monolayer (SAM) was found to be an effective coating process [22].

3.2 Introduction to Self-Assembled Monolayers (SAMs)

The self-assembled monolayers (SAMs) due to their structure and formation properties have been studied extensively and became the hot topic of research interest in the recent years due to their possible applications in sensors [23], protective coatings [24] and electronic semiconductors [25]. SAMs are a versatile tool that can be used to modify the surface properties of metals (Ag, Ag), metal oxides (Al2O3, SiO2, TiO_2) and semiconductors (Si, GaN, InP, InGaAs). The SAMs structures are formed by a spontaneous chemisorption on the surfaces in an ordered manner in the size range of 1-3 nm.

It is important to find a self-assembly molecule that can covalently bind to a specific surface of interest which usually consists of an anchor group, a spacer group and a terminal functional group [26]. The anchor group which is also named as head group forms chemical bonds to the adsorbent surface. The nature of the adsorbent determines the type of anchor group to be used because the thiol group (-SH) can be used for metals and the phosphonic (-PO(OH)2), silanol (-Si(OR)3), sulfonic (-SO2(OH)) or silyl (-SiR3) groups are more applicable to metal oxides [26, 27]. The terminal functional group of SAMs which is also named as tail group defines the properties of the SAM surface. For the field of corrosion protection, the non-polar group such as methyl (-CH3) can produce highly hydrophobic surfaces. Whereas, the polar groups such as carboxyl (-COOH), hydroxyl (-OH) or amine (-NH2) can form overlayers which is suitable for applications where adhesion promoters on metal or organic surfaces are needed [24, 27]. The tail group is highly applicable in the field of organic-based electronics due to their potential to form densely packed films by addition of monomers [28]. Lastly, the spacer group which is the group between the tail and anchor groups consists of long chain of alkyl with 10 to 18 methylene groups (–CH2-). The

spacer group affects the orientation and ordering of the molecules inside monolayer. The film formation and growth of monolayer is also influenced by the spacer group [27].

An Alkylyphosphonic acid (APAs) is an important class of self-assembling molecules that can produce well-anchored and robust SAMs on the surfaces of metal oxides. These SAMs produce surfaces with highly hydrophobic properties. Octadecylphosphonic acid (ODPA) is one of the long carbon chain phosphonate that is used for its bonding with metals and metal oxides such as titanium (Ti), stainless steel and nitinol [29-31].

3.2.1 ODPA functionalized TiO_2 Nanotubes

Self-assembled monolayers (SAMs) such as ODPA or PFDPA have been employed to create superhydrophobic coatings and address the problems such as high cost and poor wear resistance of stainless steel. However, most of these coatings suffered from the hydrolytic instability of the SAM and the highest achieved contact angle was 108° [32]. To improve the superhydrophobic properties of stainless steel surface, Fujishima et al. reported a superhydrophobic surface of stainless steel achieved by silane treatment [33]. The problem is that the organic monolayers alone will experience high erosion rates because a chemically inert ceramic host coating is needed for the monolayer. In other research works, SiO2 and TiO_2 nanoparticles were used to create superhydrophobic coatings [34, 35]. The problem is that, for instance, when TiO_2 coating on stainless steel is used following a functionalization with SAMs, the TiO_2 needs to cover most of the surface. However, this is not feasible due to limitations of depositing Ti on large surfaces. Also, due to turbulent flows, any deposited or fabricated nanostructure on stainless steel is not durable enough thus leading researchers to engineer the formation of Cassie-Baxter type wetting by combining nanoscale and microscale texture on the surface of stainless steel to resist water absorption by trapping air at different size scales. In this project, a solution containing

functionalized discrete titania nanotubes deposition on stainless steel surfaces is proposed to form superhydrophobic coating and together with discrete nanotubes facilitating the formation of Cassie-Baxter type wetting state.

3.3 Introduction to Contact Angle

Contact angle measurement is considered to be a simple and quick method to quantify surface wetting thus it is important to understand each wetting state and the key factors affecting the surface wetting properties. It is often difficult to reproduce contact angle measurements in any systems due to large number of parameters. There are three types of contact angles such as the Young model, Wenzel model and Cassie-Baxter model defined to address various situations. To analyze the contact angle; Young's equation for the ideal surface, the Wenzel equation for the surface with roughness, and the Cassie-Baxter equation for the surface with chemical heterogeneity are used. The figure 3.1 represents the wetting state of a liquid and their contact angles in these three models.

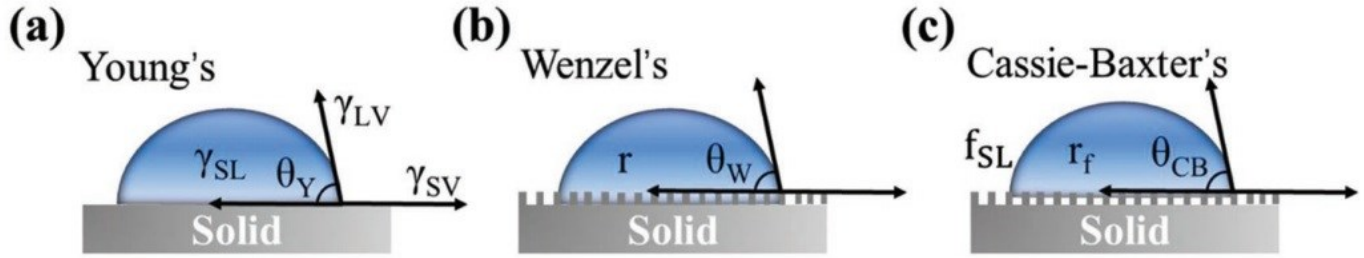

Figure 3.1- Wetting state of a liquid droplet on different solid surfaces in air and corresponded contact angle (CA) models: a) Young's, b) Wenzel's, and c) Cassie–Baxter's. Modified with permission from ref. [60]

3.3.1 Young's Model

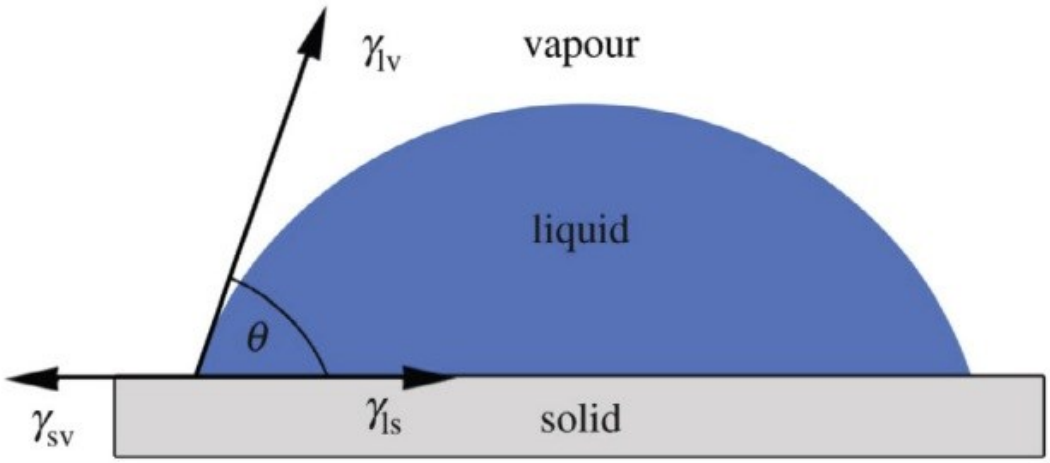

Figure 3.2- Schematic of Young's equation. Modified with permission from ref. [59]

Thomas Young, in 1805, first discovered the relationship between the surface tension and contact angle of a liquid drop on a solid surface as shown in figure 3.2 [36]. The ideal mechanical equilibrium of the drop is determined under the action of three interfacial tensions; solid-air surface tension, solid-liquid interfacial tension and liquid-air surface tension. The Young's contact angle is determined by the balanced surface tension forces and this relationship is described in Young's equation as given in equation (1);

$$Cos\Theta Y = (\gamma_{SV} - \gamma_{SL})/\gamma_{LV} \qquad (1)$$

where "γ_{SV}" is the change in surface energy between solid and vapor, "γ_{SL}" is the change in surface energy between solid and liquid, "γ_{LV}" is the change in surface energy between vapor and liquid.

The Young's classical equation, however, does not work for the real surfaces because it requires that the surface is flat, inert, smooth, non-porous, homogeneous, non-soluble and non-deformable [37-39]. According to Young equation, a surface that meets all these mentioned requirements is

accepted to be an ideal surface. The real surfaces have apparent contact angles that are not unique and therefore the value falls into a wide interval between a maximum (advancing) and minimum (receding) contact angles. The difference between these maxima and minima values is referred as **contact angle hysteresis** [40]. The hysteresis arises from surface heterogeneity, contamination, immobility on a macromolecular scale and roughness.

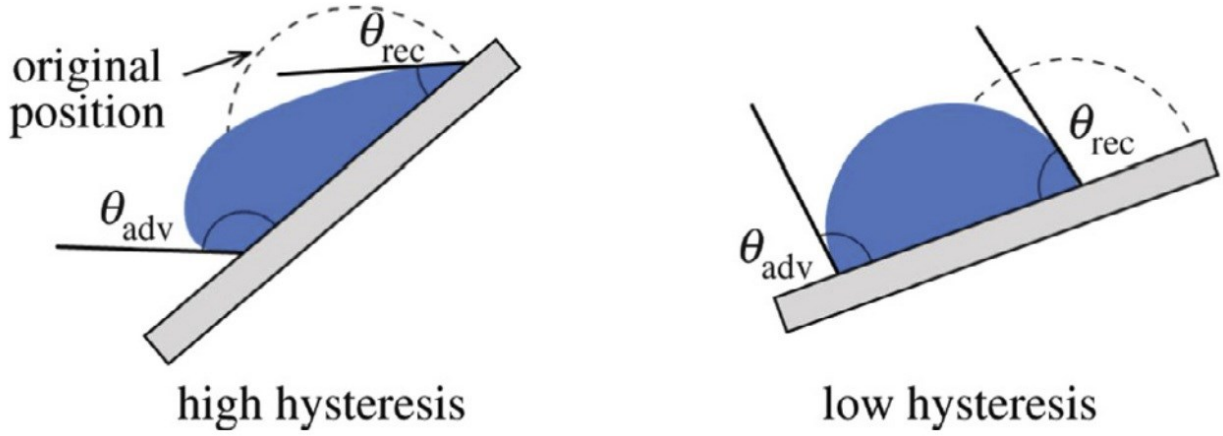

Figure 3.3- Schematic of high contact angle hysteresis (left), and low contact angle hysteresis (right) Modified with permission from ref. [59]

3.3.2 Wenzel's Model

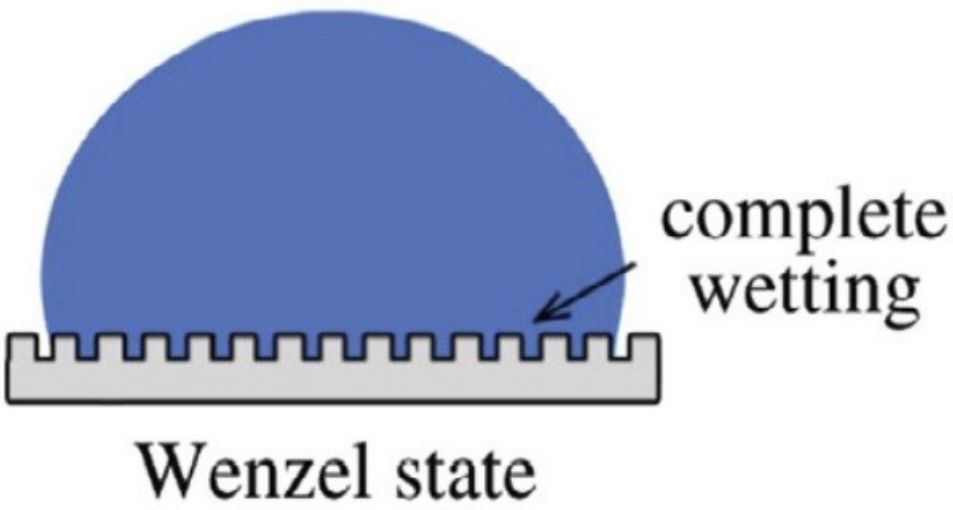

Figure 3.4 – Schematic of Wenzel's model. Modified with permission from ref. [59]

The effect of surface roughness on contact angle was first discovered by Wenzel [41]. According to Wenzel, the geometry of the surface compared to its chemistry has more effect on the static contact angle. Also, he observed that on rough surfaces a hydrophilic fluid behave as it is more hydrophilic and a hydrophobic surface behave as it is more hydrophobic. This means that the Wenzel model amplifies the wetting properties of the surfaces. The Wenzel equation is given in equation (2) where r stands for roughness factor;

$$\text{Cos}\Theta^* = r \cos\Theta_Y \qquad (2)$$

The Wenzel equation assumes that the liquid penetrates into the roughness grooves as illustrated in figure 3.4. In order for Wenzel equation to apply, the droplet must be larger than the surface roughness scale by two or three times. In case if the droplet is smaller and Wenzel equation does not apply, then the Cassie equation is used.

3.3.3 Cassie-Baxter's Model

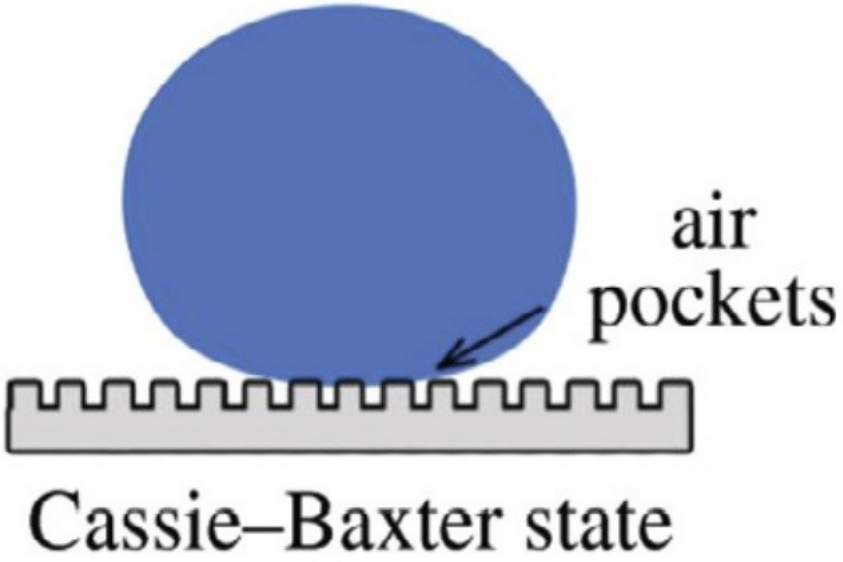

Figure 3.5 – Schematic of Cassie-Baxter model. Modified with permission from ref. [59]

The apparent contact angle of heterogeneous surfaces is determined by Cassie equation and this equation is reduced to Cassie-Baxter equation (3) for porous or mesh-like surfaces. Although it is difficult to determine the parameters of randomly roughened surfaces, the Cassie-Baxter model is more advantageous compared to Wenzel model because it can describe real surfaces more accurately. According to Cassie-Baxter model, there should be no penetration of the liquid inside the rough surface grooves [42].

$$Cos\Theta_{CB} = fs\,(r cos\Theta Y + 1) - 1 \qquad (3)$$

3.4 Experimental Work

3.4.1 Sample Preparation

A 0.5mm thick stainless steel substrate (T-304 Stainless from McMaster Carr) was used in our experiments. The substrates were initially cleaned by sequential ultrasonication in methanol (99.8%, from Fisher Scientific) then n-hexane (99%, from Acros) followed by isopropyl alcohol (99.8%, from Fisher Scientific); 15 min in each solvent. Finally, the cleaned surfaces were treated with O2 plasma for 10 min in order to get rid of adsorbed carbon impurities. Thereafter, a discrete TiO_2 nanotube (d-TNT) solution was drop-coated on O2 plasma treated stainless steel surface and was allowed to be dry overnight. Subsequently, the stainless steel surface coated with d-TNTs was immersed in a 1mM octadecylphosphonic acid (ODPA) (purchased from Alfa Aesar with 97% purity) solution in 4:1 methanol:water at room temperature for 20 h; alternatively, 1H,1H,2H,2H-perfluorodecylphosphonic acid (PFDPA) purchased from Aculon Inc. was used in an identical manner to ODPA to generate the samples used for mechanical testing. The as-modified and passivated stainless steel surface was rinsed with methanol in order to remove all physisorbed molecules and dried with N2 gas flow.

3.4.2 Synthesis of d-TNTs

Titanium foils with 0.79 mm thickness (99.7%; Alfa Aesar) were cleaned by sonication in methanol and deionized water (DI) and then dried with nitrogen gas to remove any contaminants. A two-electrode electrochemical cell with a voltage of 60 V was used for anodic formation of TiO_2 nanotubes (TNTs) with dimensions of 1×4 cm and 0.5×4 cm for anode and cathode, respectively. The anodization duration was 22 to 24 hours. A dimethyl sulfoxide (DMSO) electrolyte consisting of 2% HF was used to form TNTs with weak tube-to-tube binding as well as a weak adhesion to

the barrier layer. Hence the delamination and discretization of DMSO-synthesized TiO_2 nanotubes was rendered easier. The as-prepared TNTs were annealed at 500 °C in the presence of air for 2 hrs. The annealed TNTs from one anodized titanium foil (front and back) were detached with a blade into small vials filled with methanol (1 mL in volume). A tip sonicator was used to discretize the TNTs into a colloidal suspension of d-TNTs in methanol. The sonication was started at 150W amplitude for 4 min and continued at 240W amplitude for 1 min.

3.4.3 Electrochemical Impedance Spectroscopy

Electrochemical impedance spectroscopy (EIS) is a method that can determine both the capacitive (dielectric) and resistive properties of materials .Electrical impedance spectroscopy (EIS) is a technique that can be used in a wide range of applications, such as microbiological analysis, food products screening, corrosion monitoring, quality control of coatings, and cement paste), characterization of solid electrolytes and human body analysis. A bode plot or Nyquist (complex plane) plot is used to present the EIS data [56-58].

Electrochemical impedance spectroscopy (EIS) experiments were performed in 0.1M supporting electrolyte with a carbon counter electrode and an Ag/AgCl reference electrode. Four samples were analyzed in separate experiments and were used as the working electrode in EIS experiments – these were a bare stainless steel foil, a stainless steel foil coated with an ODPA monolayer, and two stainless steel surfaces coated with discrete TiO_2 nanotubes (d-TNTs) one with and the other without the ODPA SAM. The working electrodes had an area of 1 cm2 exposed to electrolyte and the remainder of the area was covered with parafilm. Alternating current (AC) impedance measurements were performed using a CH Instruments potentiostat in the frequency range 0 and 5000 Hz, at potentials near the open circuit potentials of the electrodes.

3.5 Characterization

A Hitachi S-4800 field emission scanning electron microscope (FESEM) and a Zeiss Sigma FESEM were used to image the morphology of the samples. Raman spectra were obtained using a Thermo-Fisher Scientific Nicolet Almega XR micro-Raman spectrometer Thermo-Fisher Scientific. Infrared spectra were obtained using a Thermo Scientific IR spectrometer. A First Ten Angstroms Inc. FTA-200 water drop contact angle measurement system together with ImageJ software, was used to make SCA measurements.

3.6 Wear Resistance and Adhesion Tests

A sand paper abrasion method was used to test the wear resistance of the stainless steel substrates coated with d-TNTs and ODPA SAMs. The stainless steel substrate was placed on 320 grit sandpaper with the coating facing downwards. A 50 g weight was placed on top of the sample, and the sample then pushed horizontally with a pair of tweezers for 5 cm increment cycles. The water drop contact angles were measured in between each abrasion cycle. Adhesion of the coating was evaluated by a tape test using Elcometer 99 Cross Hatch Adhesion Test Tape and following ASTM D3359 – 17. In short, a blade was used to scratch 5 parallel cuts 20mm long spaced 1mm apart in the coating, followed by another 5 cuts identical to the first 5 except perpendicular in orientation to produce a lattice pattern. The tape was pressed down firmly, left for one minute, and then pulled off quickly. The coating before and after the tape test was compared by FESEM. The ImageJ was used to process the resultant images.

3.7 Results and Discussions

The stepwise schematic of stainless steel surfaces coated with d-TNTs and octadeclyphosphonic acid (ODPA) is represented in figure 3.6. In summary, the d-TNTs were drop coated on the stainless steel substrate surfaces that were previously cleaned to create a porous micrometer-thick

coating. The negative charge of d-TNTs created a strong electrostatic interaction with the surface of stainless steel. As a result, the d-TNTs coat was able to survive repeated washing with water and drying cycles with nitrogen gun. In order to form superhydrophic coatings on the stainless steel surface and d-TNTs coatig, a 4:1 methanol:water solution of ODPA was prepared and the stainless steel with d-TNTs coating on was immersed in this solution. In this process, the phosphonic head group of ODPA was used to inhibit corrosion on stainless steel surface [43]. However, usually these phosphonic head groups do no totally attach to the surface of metals which does not create superhydrophobic surfaces. In this process, the addition of d-TNTs (metal oxides) provides the advantage over the bare metal surfaces because they minimize the contact area with the metal creating a higher contact angle of the surface in general [44-46]. The coating of d-TNTs' with packets of trapped air, and the micro-scale voids between the discrete nanotubes together with ODPA SAMs render the stainless steel surface superhydrophobic according to the Cassie-Baxter model [47].

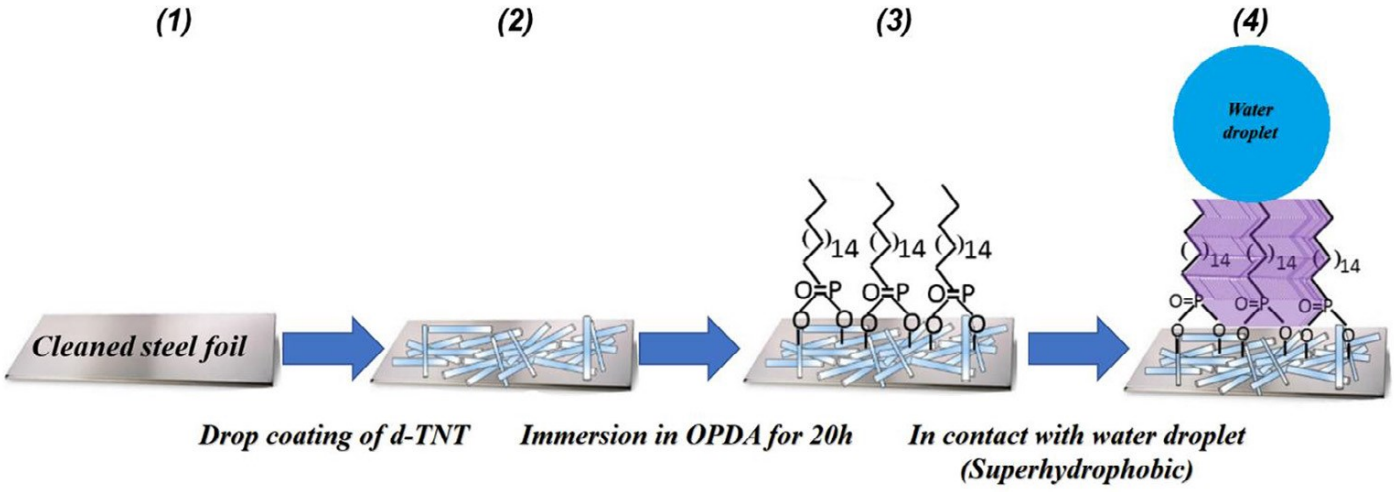

Figure 3.6 – Schematic representation of passivation of the stainless steel surface (2-3) and illustration of the expected superhydrophobic behavior of passivated stainless steel surface (4) [61]

The visual appearance of stainless steel with and without d-TNTs coat is represented in figure 3.7(a). There is a clear change in color due to the d-TNTs coat. It is observed that initially the stainless steel is totally dark and after the addition of d-TNTs, the color turns completely white. The broadband Mie scattering occurs in the white colored d-TNTs coating due to the assembly of discrete titania nanotubes. The mie scattering phenomena requires the existence of micrometer-scale nanostructures or features to resonantly scatter photons. The SEM image in figure 3.9 confirms the presence of micrometer-scale nanostructures on the large surface area of stainless steel. The Tafel analysis , which is represented in figure 3.7(b), was used to determine the open circuit potentials of the electrodes. These measurements were done by my colleague who was a post-doctoral fellow at that time.

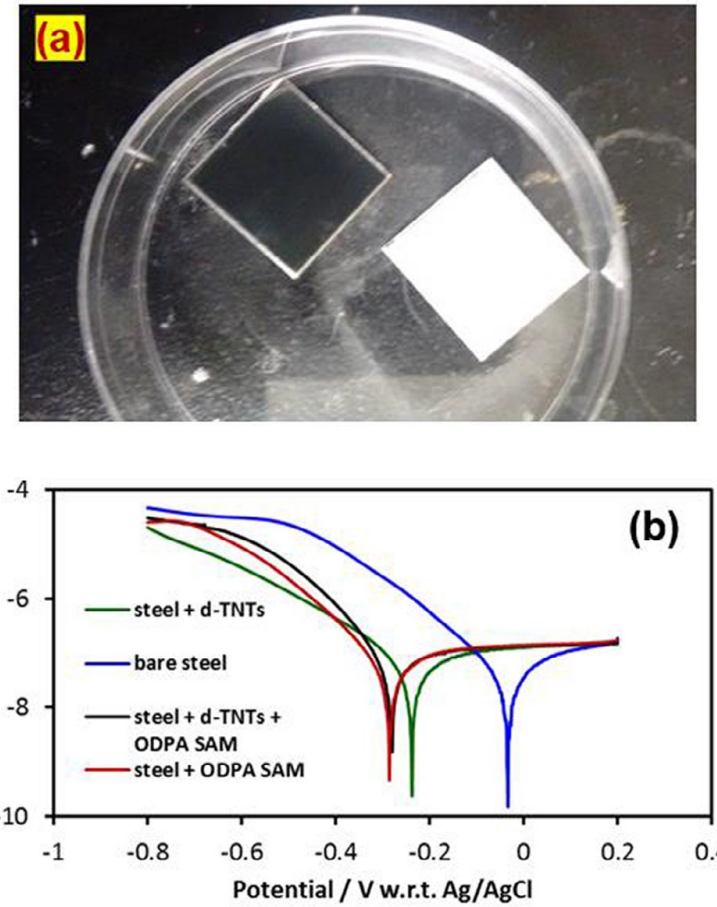

Figure 3.7 – (a) The visual appearance of stainless steel before (left) and after (right) d-TNTs coating. **(b)** Tafel plots for bare stainless steel (blue), stainless steel with ODPA SAM (red), stainless steel with d-TNTs (green) and stainless steel with d-TNTs and ODPA SAM (black).[61] Based on the Tafel analysis, the 0.25 negative shift in tafel plot in figure 3.7b, demonstrates improved corrosion resistance and passivation for the stainless steel coated with d-TNTs and subsequent functionalization with ODPA [48].

3.7.1 Raman Spectra

The Raman spectrum of stainless steel coated with d-TNTs is represented in figure 3.8. Based on this raman plot, the peaks confirm the presence of both anatase and brookite crystalline forms [49-50]. The titania nanotube arrays on foil were annealed before delamination to discretize the nanotubes. The advantage of annealing in this project was to reduce the amount of fluoride species present in nanotubes to reduce the impurities. As a result, crystalline d-TNTs with less fluoride containing species maximize the P-O-Ti bonds that are stable and strong [51].

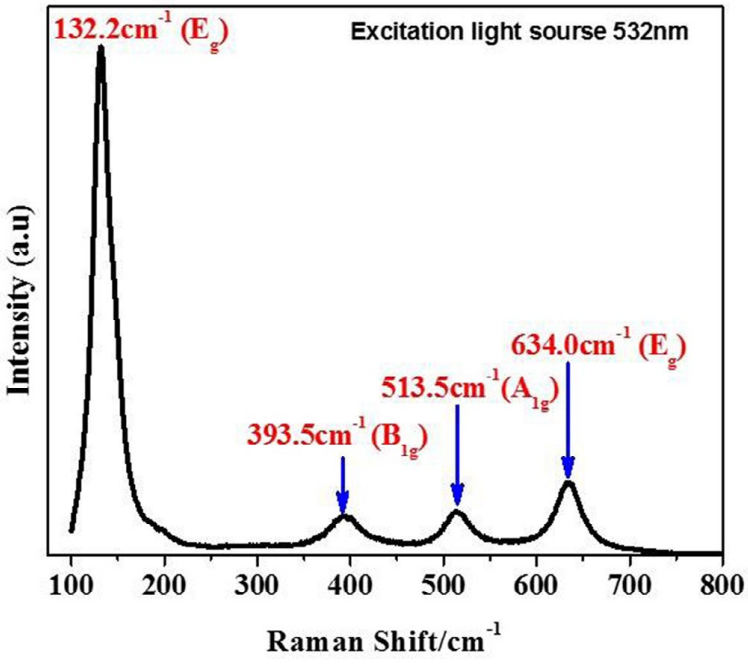

Figure 3.8 – Raman spectrum of TiO_2 nanotubes, excited by a 532 nm laser [61]

3.7.2 Morphology Study of d-TNTs Using FESEM

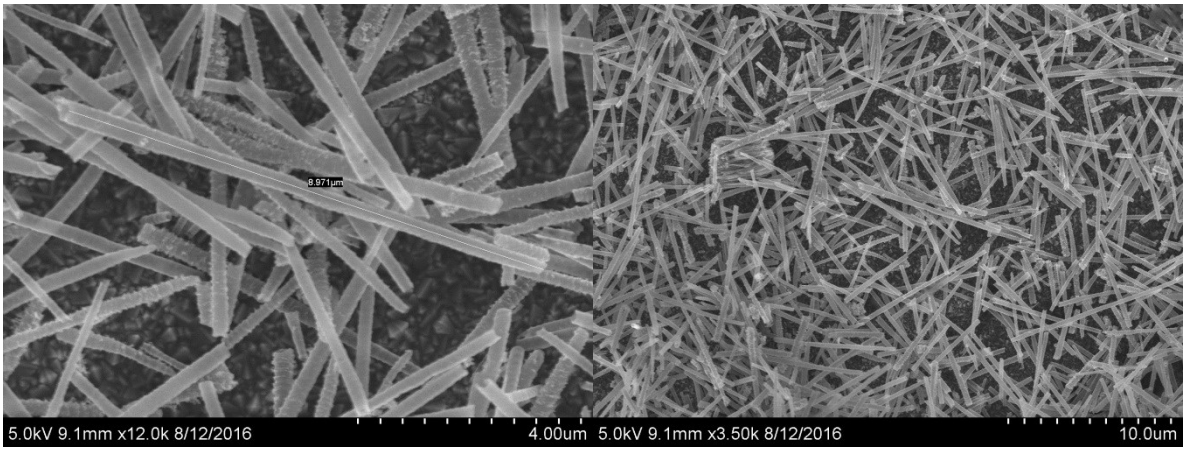

Figure 3.9 – FESEM images of d-TNTs on stainless steel surface [61]

The field emission scanning electron microscopy was used to characterize the surface morphology of the d-TNTs on the surface of stainless steel. As shown in figure 3.9, both images present the details about the individual nanotubular structure. Based on the images, the average nanotube length is between 8 to 12 µm. The diameters of nanotubes were measured to be between 100 to 150 nm. As seen in the images, the hollow structure of the nanotubes confirms the presence of sub-micrometer scales and the distance between the dispersed nanotubes confirms the micro-scale voids as mentioned before in other sections. Also, we observe a great coverage of d-TNTs on stainless steels surface which plays a key role in creating superhydrophobic coating after ODPA SAMs functionalization.

3.7.3 Contact Angle Measurements

The contact angle measurements were done in nanoFAB by dropping a 4 µL of water by sessile drop method on the surface of stainless steel. The figure 3.10 (a), (b),(c) and (d) represent the comparison of contact angles for stainless steel substrates at different conditions such as bare stainless steel cleaned with O2 plasma, stainless steel coated with ODPA SAMs, stainless steel coated with d-TNTs and stainless steel coated with both d-TNTs and ODPA SAMs. As shown in

the figure 3.10(a), the bare stainless steel has the lowest contact angle which is 21.64°. Although the stainless steel is coated with d-TNTs increase to 39.08°, the substrate is still super hydrophilic. The contact angle of ODPA only coated stainless steel agrees with the literature and it is 109.82° [52]. The coating of both d-TNTs and ODPA SAMs on stainless steel provides the best contact angle value of 174.20° which is superhydrophobic. The figure 3.10(e) represents the resilience of stainless steel substrate coated with d-TNTs and passivated with ODPA SAMs when a stream of water flows from a wash bottle. Even after 10 minutes of continuous water flow, the stainless substrate does not lose anything from its superhydrphobicity and therefore no change has been observed.

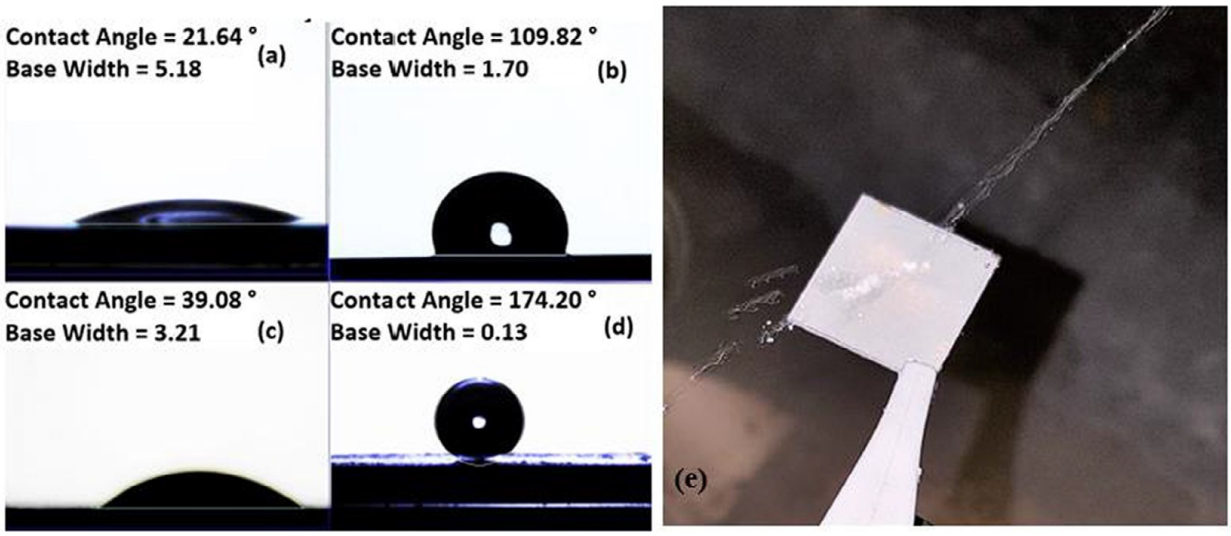

Figure 3.10 - Static contact angle values for (a) O2 plasma cleaned stainless steel surface (b) ODPA coated stainless steel surface (c) d-TNT passivated stainless steel surface and (d) ODPA coated d-TNTs on stainless steel surface (e) Photograph of water jet impacting the stainless steel surface coated with d-TNTs and the ODPA SAM. [61]

3.7.4 Infrared Reflection Absorption Spectroscopy (IRRAS)

Infrared reflection absorption spectroscopy (IRRAS) measurements provide intensities and frequencies of molecular vibration. In the IRRAS measurements, in figure 3.11 (c), two distinct

peaks of CH2 anti-symmetric and symmetric stretching modes at 2917 cm-1 and 2849 cm-1 appeared respectively [53]. In figure 3.11(d), the peaks at νP-O (∼1050 cm−1) and νP=O (∼ 1150 cm−1) confirm the presence of the phosphonate group. Since there is no peak of νP-O-H=920 cm−1, it is indicated that there is a bidentate coordination of the phosphonate to the surface [54]. In IRRAS measurements, based on the literature, the position of the Ch2 asymmetric peak indicates how organized the monolayer is on the surface. If the Ch2 anti-symmetric peak is below 2920 cm^{-1}, then the monolayer is considered as a well-organized (ordered) monolayer on the surface [55]. The peak position of CH2 anti-symmetric stretching at 2917 cm-1 shown in figure 3.11(c), confirms the formation of a well-ordered ODPA coating on d-TNTs coating of stainless steel.

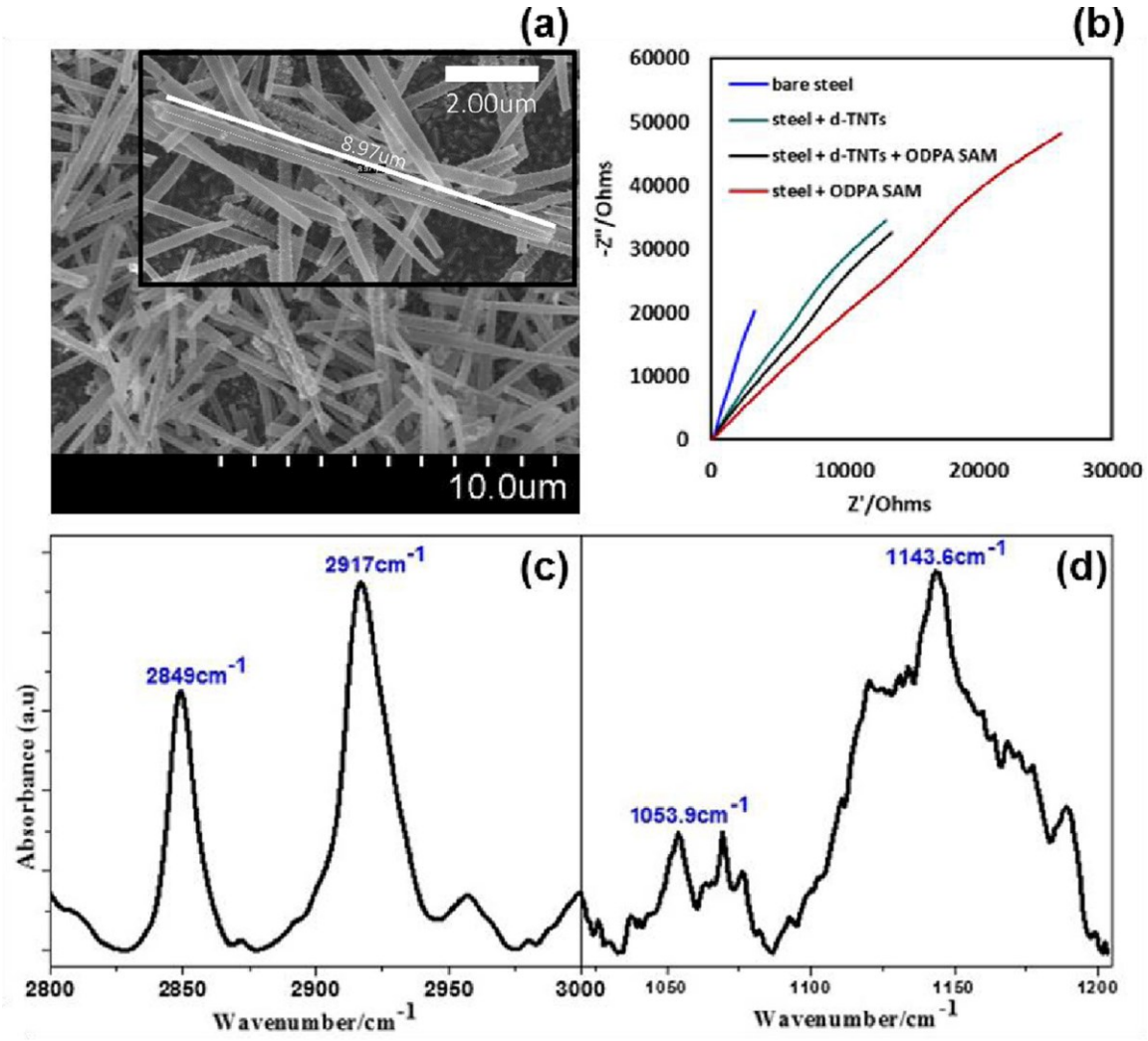

Figure 3.11 - (a) FESEM images of the discrete TiO_2 nanotubes on the stainless steel surface; (b) EIS Nyquist plots for bare stainless steel, stainless steel with ODPA SAM, stainless steel with d-TNTs and stainless steel with d-TNTs and ODPA SAM; IR spectra of C–H stretching and P-O stretching regions of ODPA monolayer are shown in (c) and (d), respectively. [61]

3.7.5 Electrochemical Impedance Spectroscopy (EIS)

The IRRAS measurement provided qualitative information about the surface coverage and binding of ODPA on the surface of d-TNTs coated stainless surface. The electrochemical impedance spectroscopy (EIS) provides quantification of the surface coverage of ODPA SAMs on the d-TNTs

coated stainless steel. A Nyquist plot of stainless steel under many conditions is shown in figure 3.11(b).

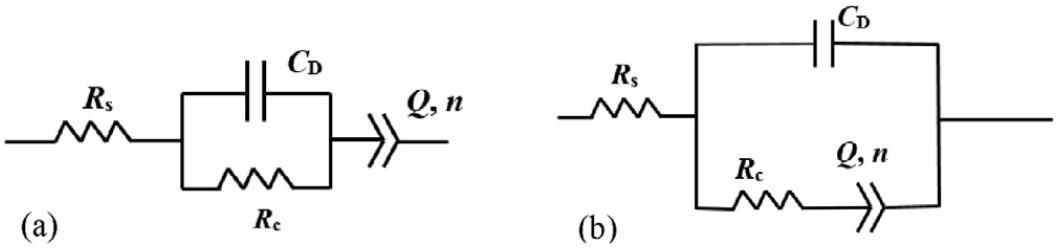

Figure 3.12- Equivalent circuit representing bare stainless steel and stainless steel with SAM (a), and the same for stainless steel with d-TNT as well as stainless steel with d-TNT and SAM (b). [61]

The equivalent circuits are given for both bare stainless steel in figure 3.12(a) and stainless steel with d-TNT and ODPA in figure 3.12(b). In order to extract the circuit parameters, the total impedance of the system was fitted to the experimental data. In figure 3.12, the parameters; R_S is the electrolyte resistance, R_C is the charge transfer resistance, C_D is the electrochemical double layer capacitance, Q is the constant phase element and n is the exponent of constant phase element. The parameters of the equivalent circuit is given in the Table 3.1 and the surface coverage angle (CSA) was calculated to be 75 % by the equation (4).

$$\theta = 1 - \frac{R_C\,(without\ ML)}{R_C(with\ ML)} \qquad (4)$$

Table 3.1. EIS generated values of circuit elements of bare stainless steel, stainless steel with ODPA SAM, stainless steel with d-TNTs, and stainless steel with d-TNTs and ODPA SAM [61]

	R_S (ohms)	**C_D (F)**	**R_C (ohms)**	**Q ($S \cdot s^n$)**	***n***
Bare stainless steel (O_2 plasma treated)	75	1.00×10^7	75	1.12×10^5	0.925
Stainless steel + ODPA SAM	75	1.15×10^5	20,000	4.00×10^6	0.690
Stainless steel + d-TNTs	75	3.00×10^7	50	6.00×10^6	0.800
Stainless steel + d-TNTs + ODPA SAM	75	7.00×10^6	200	7.00×10^6	0.760

3.7.6 Wear Resistance and Adhesion Test Results

The wear resistance of the stainless steel surfaces was tested with sand abrasion tests. The figure 3.13(a) shows the effect of increased abrasion on contact angle in graphical representation. In the abrasion tests, PFDPA was used instead of ODPA and as can be observed, the contact angle of PFDPA and d-TNT coated stainless steel (~152°) is a little less than the ODPA (as well as d-TNT) coated stainless steel. In the abrasion test, it was observed that as the abrasion of sand paper time increases the contact angle decreases. The static contact angles of the substrate surface before abrasion test were very close thus there is no error bar included in the graph. This shows that the superhydrophobicity is mostly uniform across the substrate. However, after abrasion tests, as the abrasion of sand paper length increases the standard deviation also increase. This confirms that the wear resistance is not uniform across the surface of the substrate. Also, based on the graph, at 15 cm abrasion length almost 10% of the coating was removed from the surface. The FESEM images in figure 3.13(b) and (c), represent the results of the tape test method. This time, ODPA and d-

TNTs coated stainless steel surface was evaluated to test the adhesion properties of the surface. When the tape was removed, there was only a clear sign of color change from strong and thick white to whitish grey color rather than chipping or flaking of the coat on stainless steel. As a result of the tape test, almost 80% of the coating was removed proving that there is still room for improvement of surface properties in the future projects.

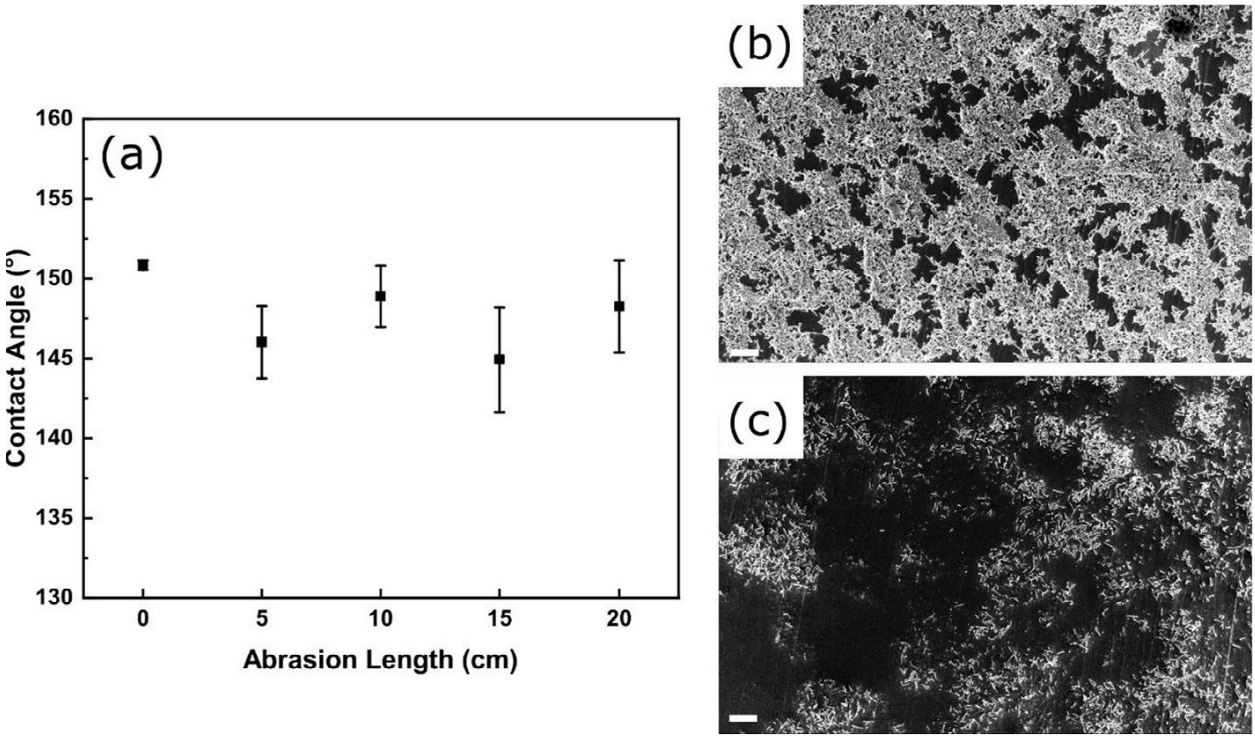

Figure 3.13 - (a) Static contact angle measurements of a PFDPA coated d-TNTs on stainless steel with corresponding abrasion length over sandpaper. FESEM images before and after a tape adhesion test of ODPA coated d-TNT coatings on stainless steel are shown in (b) and (c) respectively [61].

3.8 Conclusion

In this project, a new strategy is demonstrated to render a stainless steel surface superhydrophobic with coating the surface with d-TNTs and ODPA. The solution processing method was used to drop coat or spray coat the d-TNTs on the surface of stainless steel first and subsequently coat with

ODPA SAMs to increase the corrosion resistance of the surface. The anodically formed discrete TiO_2 nanotubes were used due to its facile method. In this project the hallmarks of the method are process simplicity, scalability, and cost effectiveness. The industrial significance of this method is emphasized by the fact that a contact angle of 166 ± 8° was obtained for stainless steel surfaces passivated by d-TNTs and ODPA SAM, implying highly water repellent behavior and corrosion resistance. This coating may be able to be extended to other substrates although we make a final note that initial trials depositing our d-TNTs on glass and polystyrene resulted in the formation of island spots rather than full coverage. The extension of the d-TNT/SAMs coatings to other substrates, as well as improving the mechanical properties of the coatings in general comprise potential topics for future work.

Chapter 4- Summary and Future Work

4.1 Summary

The work in this thesis on synthesis and applications of discrete TiO_2 nanotubes is highly applicable in large scale abrasion resistant superhydrphobic coatings in oil and gas industry and anti-fouling nano-composite polymer membranes for water filtration. For instance, any solution for cleaning the water with a scalable, facile and cost effective method is highly desirable when the scarcity of water in the world is considered. Also, creating superhydrophobic coating on metals that are frequently used in industrial pipelines, vessels and boiler etc., is desirable considering the high cost of replacement and deformation of the surfaces due to corrosion, fouling and abrasion over time.

In this thesis we take advantage of the cost effective, nontoxic and simple two-electrode processing fabrication method of TiO_2 nanotubes with tunable properties such as the length, packing and crystallinity. The work focusses specifically on the bottom-up fabrication method rather than other methods including lithography and vacuum deposition which are more time consuming and expensive.

As mentioned in introduction part of this thesis, various electrolytes were employed to fabricate nanotubes with low adhesion to barrier layer (or thin barrier oxide layer) and large tube-to-tube distance. Among the EG-, DMSO-, and DEG-based electrolytes, the DMSO and DEG electrolytes with specific concentrations of HF were found to be the ideal electrolytes to fabricate discrete (individual) TiO_2 nanotubes.

In chapter 2, the hydrophilic, porous, negative surface charge, large surface area and high adsorption properties of d-TNTs are used to make the hydrophobic permeable PES polymer

membrane more hydrophilic to improve its antifouling property in water filtration systems. The addition of maximum concentration (1%) of d-TNTs as nano fillers improved the antifouling by 29%, and also improved the water flux and rejection of organic matter in comparison to pristine PES membrane.

In chapter 3, a DMSO-based electrolyte was used to fabricate the discrete TiO_2 nanotubes to be used as porous hydrophobic coating together with ODPA SAM functionalization on the surface of stainless steel. As a result, the hydrophobicity (166+-8°), corrosion and abrasion resistance of stainless steel surface highly improved with a simple method as explained in the chapter. The results in this chapter has industrial significance as this method can be extended to other substrates such as glass and polystyrene once the mechanical properties of the coating is improved further for a better and stronger coverage on the surface.

In addition of the work done in chapters 2 and 3, two other project fundamentals have been studied for further investigation. These future projects take advantage of fast electron transport and robustness of d-TNTs for optical and electrical measurements of single nanotubes for device applications as well as compatibility with fluorescent dyes and semiconducting polymers for solar cells fabrication and dye degradation applications. These future work projects will be explained in details in the next section.

4.2 Future Work

Although there has been some work done on discrete (individual) titania nanotubes and their applications, there is a very limited amount of research has been done so far to further study the electrical and optical properties of discrete nanotubes. In this thesis, as mentioned earlier, there has been work done on the superhydrophobicity and anti-fouling properties of titania nanotubes to

improve antifouling and wear resistance of polymers and stainless steel to be used in pipelines, vessels, etc. respectively. This section of thesis is related to the possible projects of d-TNTs with very promising applications and some results explained in detail for the further investigations.

4.2.1 Discrete Titania Nanotubes Coated with Alizarin Dye for fluorescence Microscopy and Electronic/Environmental Applications

4.2.1.1 Structure and Properties of Alizarin dye

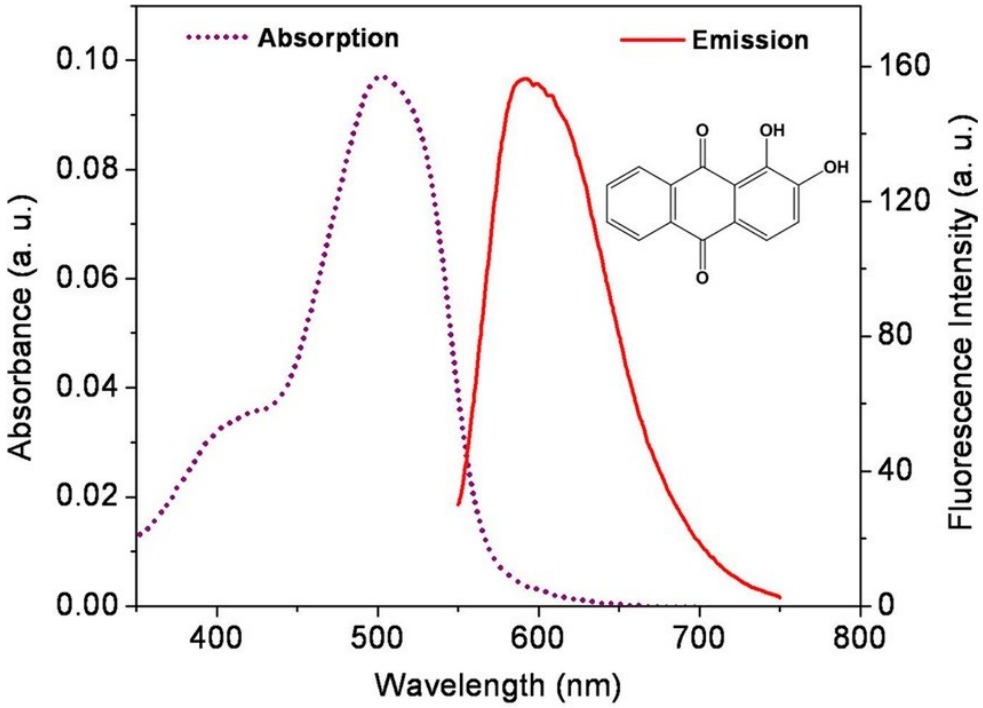

Figure 4.1 – Absorption and emission spectra of alizarin red in aqueous medium. Inset shows the molecular structure of the dye molecule. Reprinted with permission from ref. [13]

Alizarin, also known as Turkey Red or 1, 2-dihydroxyanthraquinone, is an organic compound with the formula $C_{14}H_8O_4$. Thorough the history, alizarin was used as a natural red dye in textile industry. This red dye was derived from the roots of plants of the madder genus [5]. The molecular structure of alizarin as well as its absorption and emission spectra are shown in figure 4.1. Based on the absorbance and emission plot, the dye exhibits a very intense absorbance at around 503 nm.

Around 407 nm, there is a less vibrational shoulder which corresponds to n → π* and π → π* transitions and molar extinction coefficient, ε ~ 29100 M−1 cm−1 corresponding to the monomeric form of the fluorophore [6]. The emission spectrum of the plot is maximum at 593 nm. Based on the study done by Rahman et. al., the maximum fluorescent intensity of alizarin dye increases with increasing concentration of the dye molecules. Also, in between the range of 3 to 33 μL, there is no high order of aggregation or significant dimerization which makes it suitable to be used in emission study of metals and semiconductors.

4.2.1.2 Interactions with TiO_2 nanotubes and Possible Applications

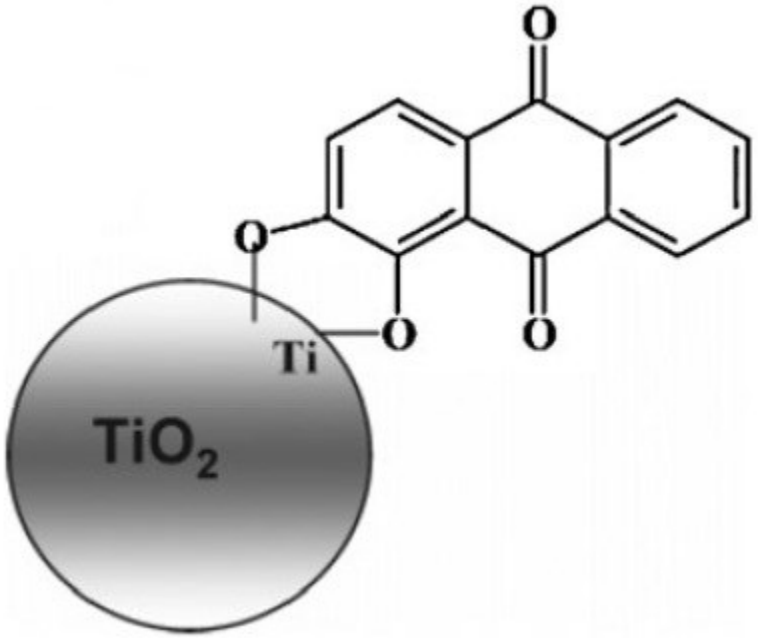

Figure 4.2 - Model of the surface adsorption of alizarin *via* the hydroxyl group bonding to the TiO_2 nanoparticles. Modified with permission from ref. [14]

Alizarin dye can anchor to TiO_2 very strongly with two chelating hydroxyl bonds [7, 8]. The adsorption of alizarin dye is illustrated in figure 4.2 by hydroxyl bonding to TiO_2 nanoparticles. Binding to TiO_2 nanotubes is also expected to be similar.

The fluorescent microscopy of single nanotubes coated with Alizarin dye can provide novel information for understanding the basic mechanism of heterogeneous chemical reactions on semiconductors. Also, the single nanotubes can help understanding the charge transfer properties of the system in the photocatalytic applications without any disturbance due to other molecules or nanoparticles present. The fluorescent microscopy images of alizarin dye coated d-TNTs are shown in figure 4.3. For further understanding the photocatalytic behavior of d-TNTs, photoluminescence (PL) measurements can also be done.

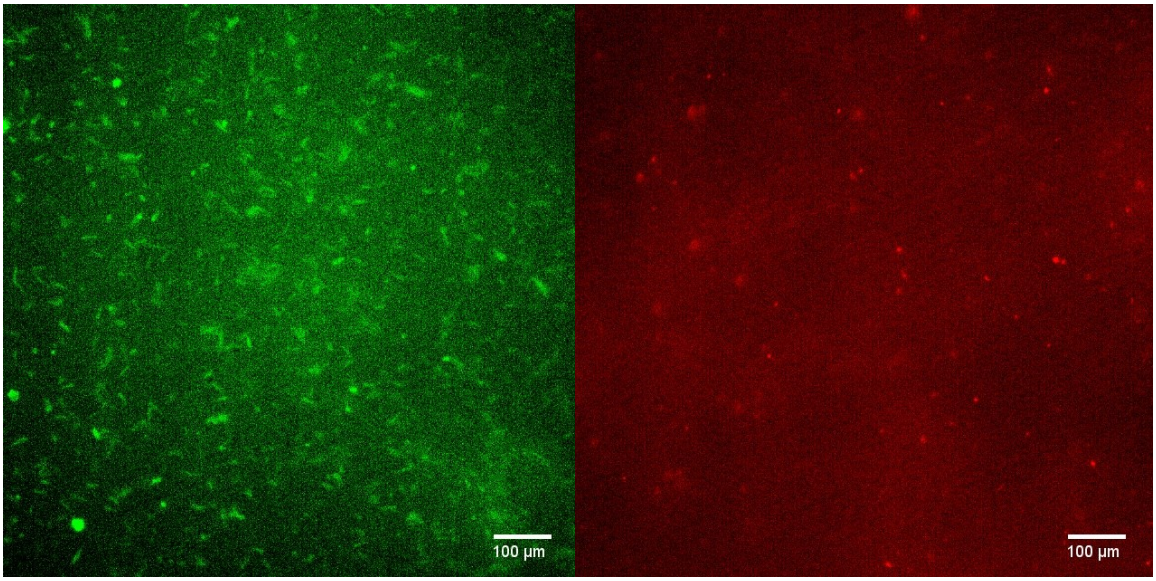

Figure 4.3 – The fluorescence microscopy images of d-TNTs coated with Alizarin. (left) Green channel image (Excitation: 480 nm; Emission 535 nm), (right) Red channel image (Excitation: 565 nm; Emission 610 nm)

Dye adsorption is another application that can be benefited using d-TNTs with high adsorption capacity and large surface area. Adsorption is an economical, easy and efficient method to remove pollutant dyes [9, 10]. In this method, the pollutants such as dyes are transferred from an aqueous media to the adsorbent where they can be reused by reprocessing after adsorption which makes the method a very economically and environmentally friendly [11, 12].

4.2.2 Dielectrophoretic Alignment of Single Discrete Titania Nanotubes Applications

The anodized TiO_2 nanotubes, as mentioned earlier, have attracted attention due to their unique properties such as wide bandgap, large surface area and tunable nanotube geometry. The electrical and optical properties of TNTAs such as carrier concentration and conversion efficiency have been explored to improve the applications of TNTAs in photocatalysis [1, 2]. However, the physical and structural properties of discrete (individual) titania nanotubes (d-TNTs) and their assembled objects have not been explored in full potential. The investigation of electrical properties of d-TNTs is still a challenge. In the proposed future project, alignment of d-TNTs across two electrodes via dielectrophoresis is expected to help studying the optical and electrical properties of d-TNTs in detail.

4.2.2.1 Dielectrophoresis Phenomena

A Dielectrophoresis (DEP) phenomenon was first described by Herbert Pohl in 1950. DEP is an electrostatic phenomenon that is described by the motion of the suspended particles in an inhomogeneous electric field due to polarization forces. DEP can also be explained as the transfer of dielectrics due to a dielectric force (FDEP) determined in equation 1:

$$F_{DEP} \propto \varepsilon_S \, Re\{K(\omega)\} \nabla |E_{rms}|^2 \qquad (1)$$

Where ε_m is dielectric constant of the surrounding medium, ε_p is dielectric constant of the particulates and E_{rms} is the average electric field intensity [3]. If F_DEP > 0, the particulates will move positively by dielectrophoresis to the places with higher electric field intensities. While F_DEP < 0, the particulates will move negatively by dielectrophoresis to the places with lower electric field intensities.

4.2.2.2 Possible Electrode Design

The first step in designing the electrodes is to create designs in the L-Edit software. A pattern generation is used to print the photomask of the designs to be used in photolithography. A previously designed photomask presented in figure 4.4 containing various separations per device of 2 μm, 4 μm, 12 μm, and 38 μm is used for some preliminary alignment experiments.

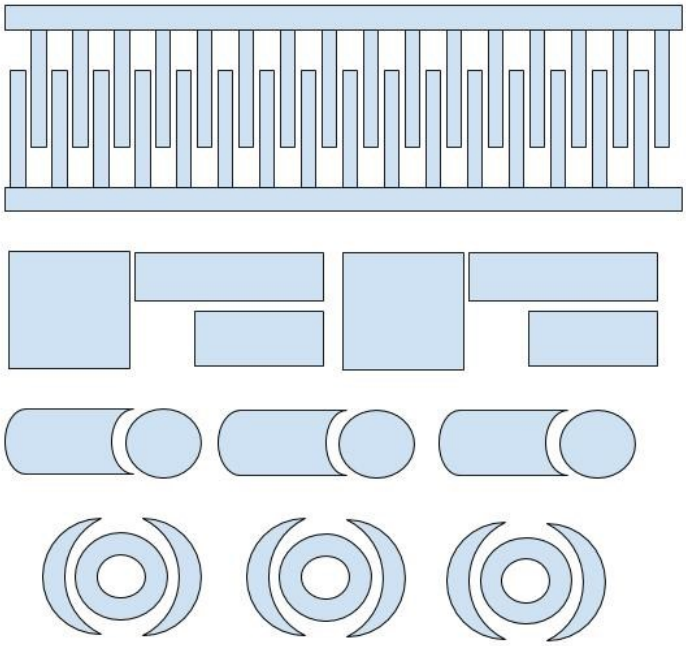

Figure 4.4 – Various designs of electrodes with different separation.

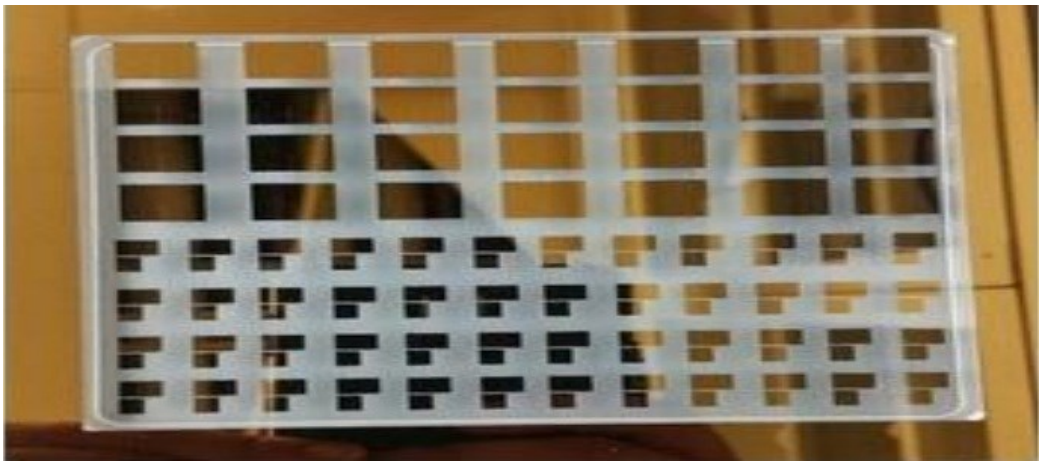

Figure 4.5 – The printed photomask by pattern generator

After the design of electrodes on L-Edit software was done and the photomask was printed with pattern generator shown in figure 4.5, the photolithography method was used to fabricate the design on a silicon wafer to be used in alignment experiments. The steps of the photolithography are as follows:

- Clean Si-SiO2 wafer with Piranha solution for 15 minutes, then treat with HDMS
- Apply 5-10 mL of HPR 504 positive photoresist. Spin coat for 10 s at 500 RPM, then 10 s at 4000 RPM
- Soft bake at 115° for 90 s, then allow 15 minutes for rehydration
- Expose UV through photomask for ~2.4 s
- Immerse the wafer in developer solution for 20 s until the exposed resist is removed
- Sputter 10 nm of Cr, followed by 200 nm of Au without breaking vacuum
- Wet etch the Au and Cr
- Immerse the wafer within acetone inside of ultrasonicator for a few minutes, then rinse the wafer with IPA to remove remaining acetone

4.2.2.3 Experiment Details and Possible Applications

The current-voltage (I-V) curves for the aligned single nanotubes across the electrodes can be obtained from 2-point electrical measurements in vacuum. From these measurements we expect that the current of crystalline phase (anatase or rutile) of d-TNTs to have a higher current based on the electrical conductivity study of nanotubes annealed at different temperatures reported by Tighineanu et. al. [4]. From the I-V curves, the semiconducting behavior of the d-TNTs can be explored and as a result of a series of I-V curve analysis, we will be able to obtain the carrier concentration, carrier mobility, resistivity and the resistance. It is specifically important to derive the mobility of the d-TNT to compare it with thin films and nanoparticles to prove the advantage of using d-TNTs in semiconductor device applications. For example, the advantage of the single nanotubes in this project is to have a higher electron transport in comparison to the bundled arrays of nanotubes. We expect that the contacts between the tubes in arrays of nanotube affect the electron transport making it more complicated. The information about mobility can help understanding the application of nanotubes in photocatalysis. For instance, if the electron mobility is low in a photocatalyst then a higher recombination rate of photogenereted holes and electrons is expected which lowers the photocatalytic activity.

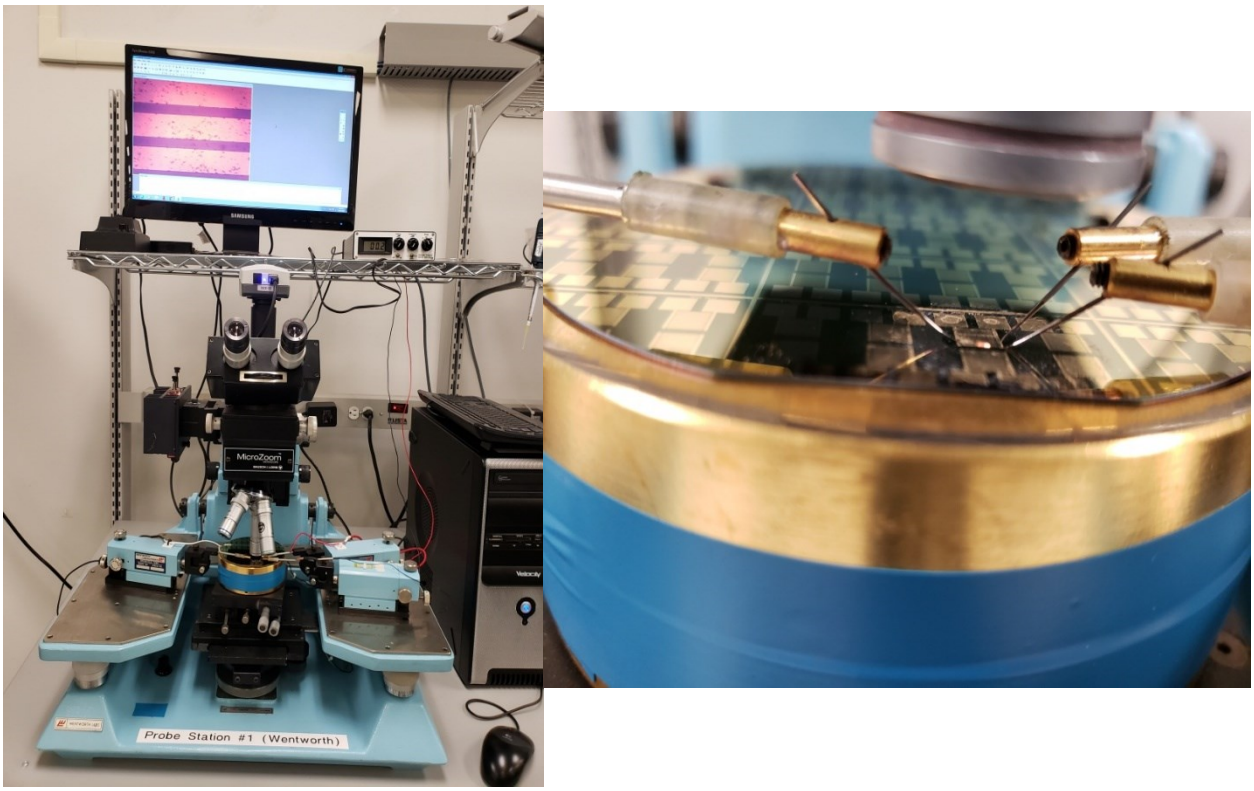

Figure 4.6 – The experimental set-up for alignment of d-TNTs consisting of a microscope and 4-point probe

We have run some basic experiments with 4-point probe to align the d-TNTs across the two electrodes with the designs including various distances of two electrodes to provide flexibility when aligning different length of nanotubes (figure 4.6). This project needs further modification of experimental design and measurements of I-V curves to further understand the electrical and optical properties of single nanotubes as well as fabricating semiconductor devices

References

Chapter 1

[1] X. Wang, Z. Li, J. Shi, and Y. Yu, "One-dimensional titanium dioxide nanomaterials: nanowires, nanorods, and nanobelts," *Chem. Rev.*, 2014, **114**, 9346–9384.

[2] B. Liu and E. S. Aydil, "Growth of oriented single-crystalline rutile TiO_2 nanorods on transparent conducting substrates for dye-sensitized solar cells," *J. Am. Chem. Soc.*, 2009, **131**, 3985-3990.

[3] D. F.-Rohlfing, A. Zaleska, and T. Bein, "Three-dimensional titanium dioxide nanomaterials," *Chem. Rev.*, 2014, **114**, 9487-9558.

[4] A. Fujishima and K. Honda, "Electrochemical photolysis of water at a semiconductor electrode," *Nature*, 1972, **238**, 37.

[5] S. I. Na, S. S. Kim, W. K. Hong, J. W. Park, J. Jo, Y. C. Nah, T. Lee, and D. Y. Kim, "Fabrication of TiO_2 nanotubes by using electrodeposited ZnO nanorod template and their application to hybrid solar cells," *Electrochim. Acta*, 2008, **53**, 2560-2566.

[6] C. Bae, H. Yoo, S. Kim, K. Lee, J. Kim, M. M. Sung, and H. Shin, "Template-directed synthesis of oxide nanotubes: Fabrication, characterization, and applications," *Chem. Mater.*, 2008, **20**, 756-767.

[7] M. G. Choi, Y. G. Lee, S. W. Song, and K. M. Kim, "Lithium-ion battery anode properties of TiO_2 nanotubes prepared by the hydrothermal synthesis of mixed (anatase and rutile) particles," *Electrochim. Acta*, 2010, **55**, 5975-5983.

[8] C. C. Tsai and H. Teng, "Regulation of the physical characteristics of titania nanotube aggregates synthesized from hydrothermal treatment," *Chem. Mater.*, 2004, **16**, 4352-4358.

[9] M. A. Khan and O. B. Yang, "Optimization of silica content in initial sol-gel grain particles for the low temperature hydrothermal synthesis of titania nanotubes," *Cryst. Growth Des.*, 2009, **9**, 1767-1774.

[10] T. Kasuga, M. Hiramatsu, A. Hoson, T. Sekino, and K. Niihara, "Titania nanotubes prepared by chemical processing," *Adv. Mater.*, 1999, **11**, 1307-1311.

[11] S. Kaneco, Y. Chen, P. Westerhoff, and J. C. Crittenden, "Fabrication of uniform size titanium oxide nanotubes: Impact of current density and solution conditions," *Scr. Mater.*, 2007, **56**, 373-376.

[12] H. Tsuchiya, J. M. Macak, I. Sieber, and P. Schmuki, "Self-organized high-aspect-ratio nanoporous zirconium oxides prepared by electrochemical anodization," *Small*, 2005, **1**, 722-725.

[13] J. M. Macák, H. Tsuchiya, and P. Schmuki, "High-aspect-ratio TiO_2 nanotubes by anodization of titanium," *Angew. Chem. Int. Ed.*, 2005, **44**, 2100-2102.

[14] V. Zwilling, E. Darque-Ceretti, A. Boutry-Forveille, D. David, M. Y. Perrin, and M. Aucouturier, "Structure and physicochemistry of anodic oxide films on titanium and TA6V alloy," *Surf. Interface Anal.*, 1999, **27**, 629-637.

[15] D. Gong, C. A. Grimes, O. K. Varghese, W. Hu, R. S. Singh, Z. Chen, and E. C. Dickey, "Titanium oxide nanotube arrays prepared by anodic oxidation," *J. Mater. Res.*, 2001, **16**, 3331-3334.

[16] D. Gong, A. Craig, Grimes, et al., Observation of titanium oxide nanotube-like arrays prepared by anodic oxidation, Boston: MRS Fall Meeting, Nov. 26–29, 2001.

[17] F. Wang, Z. Shi, F. Gong, J. Jiu, and M. Adachi, "Morphology control of anatase TiO_2 by surfactant-assisted hydrothermal method," *Chinese J. Chem. Eng.*, 2007, **15**, 754-759.

[18] P. Roy, S. Berger, and P. Schmuki, "TiO_2 nanotubes: Synthesis and applications," *Angew. Chem. Int. Ed.,* 2011, **50**, 2904-2939.

[19] Y. Yu and D. Xu, "Single-crystalline TiO_2 nanorods: Highly active and easily recycled photocatalysts," *Appl. Catal. B*, 2007, **73**, 166-171.

[20] Z. Wu, F. Dong, W. Zhao, H. Wang, Y. Liu, and B. Guan, "The fabrication and characterization of novel carbon doped TiO_2 nanotubes, nanowires and nanorods with high visible light photocatalytic activity," *Nanotechnology*, 2009, **20**, 235701.

[21] D. Kuang, J. Brillet, P. Chen, M. Takata, S. Uchida, H. Miura, K. Sumioka, S. M. Zakeeruddin, and M. Grätzel, "Application of highly ordered TiO_2 nanotube arrays in flexible dye-sensitized solar cells," *ACS Nano*, 2008, **2**, 1113-1116.

[22] K. Fujishima, and A. Honda, "Electrochemical photolysis of water one and two-dimensional structure of poly (L-Alanine) shown by specific heat measurements at low temperatures (1.5–20 K)," *Nature*, 1972, **238**, 38–40.

[23] X. Quan, S. Yang, X. Ruan, and H. Zhao, "Preparation of titania nanotubes and their environmental applications as electrode," *Environ. Sci. Technol.*, 2005, **39**, 3770-3775.

[24] K. Aisu, T. S. Suzuki, E. Nakamura, H. Abe, and Y. Suzuki, "AAO-template assisted synthesis and size control of one-dimensional TiO_2 nanomaterials," *J. Ceram. Soc. Japan*, 2013, **121**, 915-918.

[25] K. Wang, M. Wei, M. A. Morris, H. Zhou, and J. D. Holmes, "Mesoporous titania nanotubes: Their preparation and application as electrode materials for rechargeable lithium batteries," *Adv. Mater.*, 2007, **19**, 3016-3020.

[26] B. B. Lakshmi, C. J. Patrissi, and C. R. Martin, "Sol-gel template synthesis of semiconductor oxide micro- and nanostructures," *Chem. Mater.*, 1997, **9**, 2544-2550.

[27] T. Kasuga, M. Hiramatsu, A. Hoson, T. Sekino, and K. Niihara, "Titania nanotubes prepared by chemical processing," *Adv. Mater.*, 1999, **11**, 1307-1311.

[28] X. Wei, T. Wu, H. Pang, G. Lv, X. Yang, S. Wu, S. Li, and Z. Chen, "Controllable preparation of TiO_2 nanotube arrays on Ti foil substrates," *Integr. Ferroelectr.*, 2017, **182**, 127-133.

[29] G. Li, Z. Hong, H. Yang, and D. Li, "Phase composition controllable preparation of zirconia nanocrystals via solvothermal method," *J. Alloys Compd.*, 2012, **532**, 98-101.

[30] H. M. Cheng, W. H. Chiu, C. H. Lee, S. Y. Tsai, and W. F. Hsieh, "Formation of branched ZnO nanowires from solvothermal method and dye-sensitized solar cells applications," *J. Phys. Chem. C*, 2008, **112**, 16359-16364.

[31] J. Zhang, Y. Yao, T. Huang, and A. Yu, "Uniform hollow Fe_3O_4 spheres prepared by template-free solvothermal method as anode material for lithium-ion batteries," *Electrochim. Acta*, 2012, **78**, 502-507.

[32] W. Lee, R. Ji, U. Gösele, and K. Nielsch, "Fast fabrication of long-range ordered porous alumina membranes by hard anodization," *Nat. Mater.*, 2006, **5**, 741.

[33] D. Gong, C. A. Grimes, O. K. Varghese, H. Wu, R. S. Singh, Z. Chen, and E. C. Dickey, "Titanium oxide nanotube arrays prepared by anodic oxidation," *J. Mater. Res.*, 2001, **16**, 3331-3334.

[34] G. K. Mor, O. K. Varghese, M. Paulose, N. Mukherjee, and C. A. Grimes, "Fabrication of tapered, conical-shaped titania nanotubes," *J. Mater. Res.*, 2003, **18**, 2588-2593.

[35] Q. Cai, M. Paulose, O. K. Varghese, and C. A. Grimes, "The effect of electrolyte composition on the fabrication of self-organized titanium oxide nanotube arrays by anodic oxidation," *J. Mater. Res.*, 2005, **20**, 230-236.

[36] Q. Cai, L. Yang, and Y. Yu, "Investigations on the self-organized growth of TiO_2 nanotube arrays by anodic oxidization," *Thin Solid Films*, 2006, **515**, 1802-1806.

[37] E. E. Oguzie, B. N. Okolue, E. E. Ebenso, G. N. Onuoha, and A. I. Onuchukwu, "Evaluation of the inhibitory effect of methylene blue dye on the corrosion of aluminium in hydrochloric acid," *Mater. Chem. Phys.*, 2004, **87**, 394-401.

[38] M. Paulose, H. E. Prakasam, O. K. Varghese, L. Peng, K. C. Popat, G. K. Mor, T. A. Desai, and C. A. Grimes, "TiO_2 nanotube arrays of 1000 μm length by anodization of titanium foil: Phenol red diffusion," *J. Phys. Chem. C*, 2007, **111**, 14992-14997.

[39] S. Yoriya, G. K. Mor, S. Sharma, and C. A. Grimes, "Synthesis of ordered arrays of discrete, partially crystalline titania nanotubes by Ti anodization using diethylene glycol electrolytes," *J. Mater. Chem.*, 2008, **18**, 3332-3336.

[40] J. M. Macak and P. Schmuki, "Anodic growth of self-organized anodic TiO_2 nanotubes in viscous electrolytes," *Electrochim. Acta*, 2006, **52**, 1258-1264.

[41] V. C. Anitha, D. Menon, S. V. Nair, and R. Prasanth, "Electrochemical tuning of titania nanotube morphology in inhibitor electrolytes," *Electrochim. Acta*, 2010, **55**, 3703-3713.

[42] C. C. Raj and R. Prasanth, "Transverse tuning of TiO_2 nanotube array by controlling the electrochemical charge transfer resistance with potassium carbonate and sodium carbonate composition in ammonium fluoride electrolyte," *J. Electrochem. Soc.*, 2015, **162**, E23-E29.

[43] N. K. Allam, K. Shankar, and C. A. Grimes, "Photoelectrochemical and water photoelectrolysis properties of ordered TiO_2 nanotubes fabricated by Ti anodization in fluoride-free HCl electrolytes," *J. Mater. Chem.*, 2008, **18**, 2341-2348.

[44] D. Kim, S. Fujimoto, P. Schmuki, and H. Tsuchiya, "Nitrogen doped anodic TiO_2 nanotubes grown from nitrogen-containing Ti alloys," *Electrochem. commun.*, 2008, **10**, 910-913.

[45] J. M. Macak and P. Schmuki, "Anodic growth of self-organized anodic TiO_2 nanotubes in viscous electrolytes," *Electrochim. Acta*, 2006, **52**, 1258-1264.

[46] W. Jun and L. Zhiqun, "Anodic formation of ordered TiO_2 nanotube arrays: Effects of electrolyte temperature and anodization potential," *J. Phys. Chem. C*, 2009, **113**, 4026-4030.

[47] G. D. Sulka, J. Kapusta-Kołodziej, A. Brzózka, and M. Jaskuła, "Anodic growth of TiO_2 nanopore arrays at various temperatures," *Electrochim. Acta*, 2013, **104**, 526-535.

[48] V. M. Prida, E. Manova, V. Vega, M. Hernandez-Velez, P. Aranda, K. R. Pirota, M. Vázquez, and E. Ruiz-Hitzky, "Temperature influence on the anodic growth of self-aligned Titanium dioxide nanotube arrays," *J. Magn. Magn. Mater.*, 2007, **316**, 110-113.

[49] K. Indira, S. Ningshen, U. K. Mudali, and N. Rajendran, "Effect of anodization parameters on the structural morphology of titanium in fluoride containing electrolytes," *Mater. Charact.*, 2012, **71**, 58-65.

[50] W. Jun and L. Zhiqun, "Anodic formation of ordered TiO_2 nanotube arrays: Effects of electrolyte temperature and anodization potential," *J. Phys. Chem. C*, 2009, **113**, 4026-4030.

[51] S. H. Kang, J. Y. Kim, H. S. Kim, and Y. E. Sung, "Formation and mechanistic study of self-ordered TiO_2 nanotubes on Ti substrate," *J. Ind. Eng. Chem.*, 2008, **14**, 52-59.

[52] L. Yin, S. Ji, G. Liu, G. Xu, and C. Ye, "Understanding the growth behavior of titania nanotubes," *Electrochem. commun.*, 2011, **13**, 454-457.

[53] X. Feng, J. M. Macak, and P. Schmuki, "Robust self-organization of oxide nanotubes over a wide pH range," *Chem. Mater.*, 2007, **19**, 1534-1536.

[54] M. Paulose, K. Shankar, S. Yoriya, H. E. Prakasam, O. K. Varghese, G. K. Mor, T. A. Latempa, A. Fitzgerald, and C. A. Grimes, "Anodic growth of highly ordered TiO_2 nanotube arrays to 134 μm in length," *J. Phys. Chem. B*, 2006, **110**, 16179-16184.

[55] M. Christophersen, J. Carstensen, K. Voigt, and H. Föll, "Organic and aqueous electrolytes used for etching macro- and mesoporous silicon," in *Physica Status Solidi (A)*, 2003, **197**, 34-38.

[56] C. A. Grimes and G. K. Mor, TiO_2 nanotube arrays: Synthesis, properties, and applications. Springer Science & Business Media, 2009.

[57] A. El Ruby Mohamed and S. Rohani, "Modified TiO_2 nanotube arrays (TNTAs): Progressive strategies towards visible light responsive photoanode, a review," *Energy Environ. Sci*., 2011, **4**, 1065-1086.

[58] K. Shankar, G. K. Mor, A. Fitzgerald, and C. A. Grimes, "Cation effect on the electrochemical formation of very high aspect ratio TiO_2 nanotube arrays in formamide-water mixtures," *J. Phys. Chem. C*, 2007, **111**, 21-26.

[59] Q. Cai, M. Paulose, O. K. Varghese, and C. A. Grimes, "The effect of electrolyte composition on the fabrication of self-organized titanium oxide nanotube arrays by anodic oxidation," *J. Mater. Res.*, 2005, **20**, 230-236.

[60] J. M. Macak and P. Schmuki, "Anodic growth of self-organized anodic TiO_2 nanotubes in viscous electrolytes," *Electrochim. Acta*, 2006, **52**, 1258-1264.

[61] S. So, K. Lee, and P. Schmuki, "Ultrafast growth of highly ordered anodic TiO_2 nanotubes in lactic acid electrolytes," *J. Am. Chem. Soc.*, 2012, **134**, 11316-11318.

[62] R. Ameta, S. Benjamin, S. Sharma, and M. Trivedi, "Dye-sensitized solar cells," in *Solar Energy Conversion and Storage: Photochemical Modes*, CRC Press, 2015.

[63] F. A. Grant, "Properties of Rutile (Titanium Dioxide)," *Rev. Mod. Phys.*, 1959, **31**, 646.

[64] G. V. Samsonov, "The oxide handbook," Springer Science & Business Media, 2013.

[65] I. Paramasivam, J. M. Macak, T. Selvam, and P. Schmuki, "Electrochemical synthesis of self-organized TiO_2 nanotubular structures using an ionic liquid (BMIM-BF_4)," *Electrochim. Acta*, 2008, **54**, 643-648.

[66] A. F. Kanta, M. Poelman, and A. Decroly, "Electrochemical characterization of TiO_2 nanotube array photoanodes for dye-sensitized solar cell application," *Sol. Energy Mater. Sol. Cells*, 2015, **133**, 76-81.

[67] S. Y. Kim, Y. K. Kim, I. S. Park, G. C. Jin, T. S. Bae, and M. H. Lee, "Effect of alkali and heat treatments for bioactivity of TiO_2 nanotubes," *Appl. Surf. Sci.*, 2014, **321**, 412-419.

[68] X. Chen and S. S. Mao, "Titanium dioxide nanomaterials: Synthesis, properties, modifications and applications," *Chem. Rev.*. 2007, **107**, 2891-2959.

[69] T. L. Thompson and J. T. Yates, "Surface science studies of the photoactivation of TiO_2 - New photochemical processes," *Chem. Rev.*. 2006, **106**, 4428-4453.

[70] J. Muscat, V. Swamy, and N. M. Harrison, "First-principles calculations of the phase stability of TiO_2," *Phys. Rev. B*, 2002, **65**, 224112.

[71] S. Berger, R. Hahn, P. Roy, and P. Schmuki, "Self-organized TiO_2 nanotubes: Factors affecting their morphology and properties," *Phys. Status Solidi B*, 2010, **247**, 2424-2435.

[72] J. W. Diggle, T. C. Downie, and C. W. Goulding, "Anodic oxide films on aluminum," *Chem. Rev.*, 1969, **69**, 365-405.

[73] S. C. Roy, M. Paulose, and C. A. Grimes, "The effect of TiO_2 nanotubes in the enhancement of blood clotting for the control of hemorrhage," *Biomaterials*, 2007, **28**, 4667-4672.

[74] J. Zhang, P. Zhou, J. Liu, and J. Yu, "New understanding of the difference of photocatalytic activity among anatase, rutile and brookite TiO_2," *Phys. Chem. Chem. Phys.*, 2014, **16**, 20382-20386.

[75] K. Indira, U. K. Mudali, T. Nishimura, and N. Rajendran, "A Review on TiO_2 nanotubes: influence of anodization parameters, formation mechanism, properties, corrosion behavior, and biomedical applications," *Journal of Bio- and Tribo-Corrosion*. 2015, **1**, 28.

Chapter 2

[1] B. S. Lalia, V. Kochkodan, R. Hashaikeh, and N. Hilal, "A review on membrane fabrication: Structure, properties and performance relationship," *Desalination*. 2013, **326**, 77-95.

[2] M. M. Pendergast and E. M. V. Hoek, "A review of water treatment membrane nanotechnologies," *Energy Environ. Sci*., 2011, **4**, 1946-1971.

[3] R. K. Joshi, S. Alwarappan, M. Yoshimura, V. Sahajwalla, and Y. Nishina, "Graphene oxide: The new membrane material," *Appl. Mater. Today*. 2015, **1**, 1-12.

[4] M. Zahid, A. Rashid, S. Akram, Z. A. Rehan, and W. Razzaq, "A comprehensive review on polymeric nano-composite membranes for water treatment," *J. Membr. Sci. Technol.*, 2018, 8(01).

[5] M. Ulbricht, "Advanced functional polymer membranes," *Polymer*. 2006, **47**, 2217-2262.

[6] Y. Yampolskii, "Polymeric gas separation membranes," *Macromolecules*, 2012, **45**, 3298-3311.

[7] M. B. Rao and S. Sircar, "Performance and pore characterization of nanoporous carbon membranes for gas separation," *J. Memb. Sci.*, 1996, **110**, 109-118.

[8] S. Farrell and K. K. Sirkar, "Mathematical model of a hybrid dispersed network-membrane-based controlled release system," *J. Control. Release*, 2001, **70**, 51-61.

[9] V. Kochkodan, D. J. Johnson, and N. Hilal, "Polymeric membranes: Surface modification for minimizing (bio) colloidal fouling," *Adv. Colloid Interface Sci*., 2014, **206**, 116-140.

[10] E. Drioli and E. Fontananova, "Integrated membrane processes," in *Membrane Operations: Innovative Separations and Transformations*, 2009.

[11] J. H. Jhaveri and Z. V. P. Murthy, "A comprehensive review on anti-fouling nanocomposite membranes for pressure driven membrane separation processes," *Desalination*. 2016, **379**, 137-154.

[12] C. Barth, M. C. Gonçalves, A. T. N. Pires, J. Roeder, and B. A. Wolf, "Asymmetric polysulfone and polyethersulfone membranes: Effects of thermodynamic conditions during formation on their performance," *J. Memb. Sci.*, 2000, **169**, 287-299.

[13] A. Rahimpour, M. Jahanshahi, S. Khalili, A. Mollahosseini, A. Zirepour, and B. Rajaeian, "Novel functionalized carbon nanotubes for improving the surface properties and performance of polyethersulfone (PES) membrane," *Desalination*, 2012, **286**, 99-107.

[14] Q. Shi, Y. Su, S. Zhu, C. Li, Y. Zhao, and Z. Jiang, "A facile method for synthesis of pegylated polyethersulfone and its application in fabrication of antifouling ultrafiltration membrane," *J. Memb. Sci.*, 2007, **303**, 204-212.

[15] H. Wang, L. Yang, X. Zhao, T. Yu, and Q. Du, "Improvement of hydrophilicity and blood compatibility on polyethersulfone membrane by blending sulfonated polyethersulfone," *Chinese J. Chem. Eng.*, 2009, **17**, 324-329.

[16] C. Barth, M. C. Gonçalves, A. T. N. Pires, J. Roeder, and B. A. Wolf, "Asymmetric polysulfone and polyethersulfone membranes: Effects of thermodynamic conditions during formation on their performance," *J. Memb. Sci.*, 2000, **169**, 287-299.

[17] J. Aburabie, L. F. Villalobos, and K. V. Peinemann, "Composite membrane formation by combination of reaction-induced and nonsolvent-induced phase separation," *Macromol. Mater. Eng.*, 2017, **302**, 1700131.

[18] J. T. Jung, J. F. Kim, H. H. Wang, E. di Nicolo, E. Drioli, and Y. M. Lee, "Understanding the non-solvent induced phase separation (NIPS) effect during the fabrication of microporous PVDF membranes via thermally induced phase separation (TIPS)," *J. Memb. Sci.*, 2016, **514**, 250-263.

[19] A. A. Mosafer, M. R. Toosi, and M. Asghari, "Effect study of hexagonal mesoporous silica/polyaniline nanocomposite on the structural properties of polysulfone membranes and its heavy metal removal efficiency," *Sep. Sci. Technol.*, 2017, **52**, 1775-1786.

[20] A. Gholami, A. R. Moghadassi, S. M. Hosseini, S. Shabani, and F. Gholami, "Preparation and characterization of polyvinyl chloride-based nanocomposite nanofiltration-membrane modified by iron oxide nanoparticles for lead removal from water," *J. Ind. Eng. Chem.*, 2014, **20**, 1517-1522.

[21] J. Dasgupta, S. Chakraborty, J. Sikder, R. Kumar, D. Pal, S. Curcio, and E. Drioli, "The effects of thermally stable titanium silicon oxide nanoparticles on structure and performance of cellulose acetate ultrafiltration membranes," *Sep. Purif. Technol.*, 2014, **133**, 55-68.

[22] J. H. Li, X. S. Shao, Q. Zhou, M. Z. Li, and Q. Q. Zhang, "The double effects of silver nanoparticles on the PVDF membrane: Surface hydrophilicity and antifouling performance," *Appl. Surf. Sci.*, 2013, **265**, 663-670.

[23] S. Y. Lee, H. J. Kim, R. Patel, S. J. Im, J. H. Kim, and B. R. Min, "Silver nanoparticles immobilized on thin film composite polyamide membrane: Characterization, nanofiltration, antifouling properties," *Polym. Adv. Technol.*, 2007, **18**, 562-568.

[24] V. Kochkodan and N. Hilal, "A comprehensive review on surface modified polymer membranes for biofouling mitigation," *Desalination*. 2015, **356**, 187-207.

[25] M. Rezakazemi, A. Dashti, H. Riasat Harami, N. Hajilari, and Inamuddin, "Fouling-resistant membranes for water reuse," *Environ. Chem. Lett*., 2018, **16**, 715-763.

[26] A. S. Al-Amoudi and A. M. Farooque, "Performance restoration and autopsy of NF membranes used in seawater pretreatment," *Desalination*, 2005, **178**, 261-271.

[27] F. Meng, S. R. Chae, A. Drews, M. Kraume, H. S. Shin, and F. Yang, "Recent advances in membrane bioreactors (MBRs): Membrane fouling and membrane material," *Water Research*. 2009, **43**, 1489-1512.

[28] J. A. Nilson and F. A. DiGiano, "Influence of NOM composition on nanofiltration," *J. Am. Water Work. Assoc.*, 1996, **88**, 53-66.

[29] Q. Li and M. Elimelech, "Organic fouling and chemical cleaning of nanofiltration membranes: Measurements and mechanisms," *Environ. Sci. Technol.*, 2004, **38**, 4683-4693.

[30] S. N. Hoseini, A. K. Pirzaman, M. A. Aroon, and A. E. Pirbazari, "Photocatalytic degradation of 2,4-dichlorophenol by Co-doped TiO_2 (Co/TiO_2) nanoparticles and Co/TiO_2 containing mixed matrix membranes," *J. Water Process Eng.*, 2017, **17**, 124-134.

[31] S. Alzahrani and A. W. Mohammad, "Challenges and trends in membrane technology implementation for produced water treatment: A review," *J. Water Process Engineering*. 2014, **4**, 107-133.

[32] Q. Zhao, J. Hou, J. Shen, J. Liu, and Y. Zhang, "Long-lasting antibacterial behavior of a novel mixed matrix water purification membrane," *J. Mater. Chem. A*, 2015, **3**, 18696-18705.

[33] J. Wang, P. Zhang, B. Liang, Y. Liu, T. Xu, L. Wang, B. Cao, and K. Pan, "Graphene oxide as an effective barrier on a porous nanofibrous membrane for water treatment," *ACS Appl. Mater. Interfaces*, 2016, **8**, 6211-6218.

[34] B. Liang, P. Zhang, J. Wang, J. Qu, L. Wang, X. Wang, C. Guan, and K. Pan, "Membranes with selective laminar nanochannels of modified reduced graphene oxide for water purification," *Carbon*, 2016, **103**, 94-100.

[35] E. Celik, H. Park, H. Choi, and H. Choi, "Carbon nanotube blended polyethersulfone membranes for fouling control in water treatment," *Water Res.*, 2011, **45**, 274-282.

[36] L. Wang, X. Song, T. Wang, S. Wang, Z. Wang, and C. Gao, "Fabrication and characterization of polyethersulfone/carbon nanotubes (PES/CNTs) based mixed matrix membranes (MMMs) for nanofiltration application," *Appl. Surf. Sci.*, 2015, **330**, 118-125.

[37] P. Daraei, S. S. Madaeni, N. Ghaemi, M. A. Khadivi, B. Astinchap, and R. Moradian, "Enhancing antifouling capability of PES membrane via mixing with various types of polymer modified multi-walled carbon nanotube," *J. Memb. Sci.*, 2013, **444**, 184-191.

[38] J. Li, Z. Liu, C. He, H. Yue, and S. Gou, "Water shortages raised a legitimate concern over the sustainable development of the drylands of northern China: Evidence from the water stress index," *Sci. Total Environ.,* 2017, **590**, 739-750.

[39] M. Hu and B. Mi, "Enabling graphene oxide nanosheets as water separation membranes," *Environ. Sci. Technol.,* 2013, **47**, 3715-3723.

[40] D. Lim, S. W. Jung, M. S. Choi, S. M. Kang, H. S. Jung, and J. Y. Choi, "Historical record of metal accumulation and lead source in the southeastern coastal region of Korea," *Mar. Pollut. Bull.*, 2013, **74**, 441-445.

[41] J. Liu, C. Tian, J. Xiong, and L. Wang, "Polypyrrole blending modification for PVDF conductive membrane preparing and fouling mitigation," *J. Colloid Interface Sci.*, 2017, **494**, 124-129.

[42] P. Pandey and R. S. Chauhan, "Membranes for gas separation," *Prog. Polym. Sci.*, 2001, **26**, 853-893.

[43] Z. S. Wang, T. Sasaki, M. Muramatsu, Y. Ebina, T. Tanaka, L. Wang, and M. Watanabe, "Self-assembled multilayers of titania nanoparticles and nanosheets with polyelectrolytes," *Chem. Mater.,* 2003, **15**, 807-812.

[44] I. Genné, S. Kuypers, and R. Leysen, "Effect of the addition of ZrO_2 to polysulfone based UF membranes," *J. Memb. Sci.*, 1996, **113**, 343-350.

[45] R. Rezaee, S. Nasseri, A. H. Mahvi, R. Nabizadeh, S. A. Mousavi, A. Rashidi, A. Jafari, and S. Nazmara, "Fabrication and characterization of a polysulfone-graphene oxide nanocomposite membrane for arsenate rejection from water," *J. Environ. Heal. Sci. Eng.*, 2015, **13**, 61.

[46] H. L. Richards, P. G. L. Baker, and E. Iwuoha, "Metal nanoparticle modified polysulfone membranes for use in wastewater treatment: A critical review," *J. Surf. Eng. Mater. Adv. Technol.*, 2012, **2**, 183.

[47] A. L. Ahmad, A. A. Abdulkarim, B. S. Ooi, and S. Ismail, "Recent development in additives modifications of polyethersulfone membrane for flux enhancement," *Chem. Eng. J.* 2013, **223**, 246-267.

[48] J. N. Shen, H. M. Ruan, L. G. Wu, and C. J. Gao, "Preparation and characterization of PES-SiO_2 organic-inorganic composite ultrafiltration membrane for raw water pretreatment," *Chem. Eng. J.*, 2011, **168**, 1272-1278.

[49] S. Zinadini, A. A. Zinatizadeh, M. Rahimi, V. Vatanpour, and H. Zangeneh, "Preparation of a novel antifouling mixed matrix PES membrane by embedding graphene oxide nanoplates," *J. Memb. Sci.*, 2014, **453**, 292-30.

[50] X. Shi, G. Tal, N. P. Hankins, and V. Gitis, "Fouling and cleaning of ultrafiltration membranes: A review," *J. Water Process Eng.,* 2014, **1**, 121-138.

[51] K. C. Khulbe, C. Feng, and T. Matsuura, "The art of surface modification of synthetic polymeric membranes," *J. Appl. Polym. Sci.,* 2010, **115**, 855-895.

[52] D. Rana and T. Matsuura, "Surface modifications for antifouling membranes," *Chem. Rev.*, 2010, **110**, pp.2448-2471.

[53] O. Burtovyy, V. Klep, T. Turel, Y. Gowayed, and I. Luzinov, "Polymeric membranes: Surface modification by 'grafting to' method and fabrication of multilayered assemblies," in ACS Symposium Series, 2009.

[54] Z. Wang, H. Yu, J. Xia, F. Zhang, F. Li, Y. Xia, and Y. Li, "Novel GO-blended PVDF ultrafiltration membranes," *Desalination*, 2012, **299**, 50-54.

[55] B. Khorshidi, B. Soltannia, T. Thundat, and M. Sadrzadeh, "Synthesis of thin film composite polyamide membranes: Effect of monohydric and polyhydric alcohol additives in aqueous solution," *J. Memb. Sci.,* 2017, **523**, 336-345.

[56] G. Zorn, I. Gotman, E. Y. Gutmanas, R. Adadi, G. Salitra, and C. N. Sukenik, "Surface modification of Ti45Nb alloy with an alkylphosphonic acid self-assembled monolayer," *Chem. Mater.*, 2005, **17**, 4218-4226.

[57] L. Y. Ng, A. W. Mohammad, C. P. Leo, and N. Hilal, "Polymeric membranes incorporated with metal/metal oxide nanoparticles: A comprehensive review," *Desalination*. 2013, **308**, 15-33.

[58] J. Kim and B. Van Der Bruggen, "The use of nanoparticles in polymeric and ceramic membrane structures: Review of manufacturing procedures and performance improvement for water treatment," *Environ. Pollut*., 2010, **158**, 2335-234.

[59] H. F. Ridgway, J. D. Gale, Z. E. Hughes, M. B. Stewart, J. D. Orbell, and S. R. Gray, "Functional nanostructured materials and membranes for water treatment." John Wiley & Sons, 2013.

[60] Y. Liao, D. G. Yu, X. Wang, W. Chain, X. G. Li, E. M. Hoek, and R. B. Kaner, "Carbon nanotube-templated polyaniline nanofibers: Synthesis, flash welding and ultrafiltration membranes," *Nanoscale*, 2013, **5**, 3856-3862.

[61] X. Qu, P. J. J. Alvarez, and Q. Li, "Applications of nanotechnology in water and wastewater treatment," *Water Res.,* 2013, **47**, 3931-394.

[62] R. L. Davies and S. F. Etris, "The development and functions of silver in water purification and disease control," *Catal. Today*, 1997, **36**, 107-114.

[63] M. Gui, V. Smuleac, L. E. Ormsbee, D. L. Sedlak, and D. Bhattacharyya, "Iron oxide nanoparticle synthesis in aqueous and membrane systems for oxidative degradation of trichloroethylene from water," *J. Nanoparticle Res.*, 2012, **14**, 861.

[64] X. Cao, J. Ma, X. Shi, and Z. Ren, "Effect of TiO_2 nanoparticle size on the performance of PVDF membrane," *Appl. Surf. Sci.*, 2006, **253**, 2003-2010.

[65] Y. Nagaoka, R. Tan, R. Li, H. Zhu, D. Eggert, Y. A. Wu, Y. Liu, Z. Wang, and O. Chen, "Superstructures generated from truncated tetrahedral quantum dots," *Nature*. 2018, **561**, 378.

[66] T. Schulmeyer, S. A. Paniagua, P. A. Veneman, S. A. Jones, P. J. Hotchkiss, A. Mudalige, J. E. Pemberton, S. R. Marder, and N. R. Armstrong, "Modification of $BaTiO_3$ thin films: Adjustment of the effective surface work function," *J. Mater. Chem.*, 2007, **17**, 4563-4570.

[67] A. Cattani-Scholz, "Functional organophosphonate interfaces for nanotechnology: A review," *ACS Appl. Mater. Interfaces*, 2017, **9**, 25643-25655.

[68] M. Sadrzadeh and S. Bhattacharjee, "Rational design of phase inversion membranes by tailoring thermodynamics and kinetics of casting solution using polymer additives," *J. Memb. Sci.*, 2013, **441**, 31-44.

[69] E. Saljoughi, M. Sadrzadeh, and T. Mohammadi, "Effect of preparation variables on morphology and pure water permeation flux through asymmetric cellulose acetate membranes," *J. Memb. Sci.*, 2009, **326**, 627-634.

[70] D. Zhang, A. Karkooti, L. Liu, M. Sadrzadeh, T. Thundat, Y. Liu, and R. Narain, "Fabrication of antifouling and antibacterial polyethersulfone (PES)/cellulose nanocrystals (CNC) nanocomposite membranes," *J. Memb. Sci.*, 2018, **549**, 350-356.

[71] A. Karkooti, A. Z. Yazdi, P. Chen, M. McGregor, N. Nazemifard, and M. Sadrzadeh, "Development of advanced nanocomposite membranes using graphene nanoribbons and nanosheets for water treatment," *J. Memb. Sci.*, 2018, **560**, 97-107.

[72] M. Hayatbakhsh, M. Sadrzadeh, D. Pernitsky, S. Bhattacharjee, and J. Hajinasiri, "Treatment of an in situ oil sands produced water by polymeric membranes," *Desalin. Water Treat.*, 2016, **57**, 14869-14887.

[73] X. Zhao, J. Ma, Z. Wang, G. Wen, J. Jiang, F. Shi, and L. Sheng, "Hyperbranched-polymer functionalized multi-walled carbon nanotubes for poly (vinylidene fluoride) membranes: From dispersion to blended fouling-control membrane," *Desalinatio*n, 2012, **303**, 29-38.

[74] V. Vatanpour, S. S. Madaeni, R. Moradian, S. Zinadini, and B. Astinchap, "Novel antibifouling nanofiltration polyethersulfone membrane fabricated from embedding TiO_2 coated multiwalled carbon nanotubes," *Sep. Purif. Technol.*, 2012, **90**, 69-82.

[75] M. Sadrzadeh, J. Hajinasiri, S. Bhattacharjee, and D. Pernitsky, "Nanofiltration of oil sands boiler feed water: Effect of pH on water flux and organic and dissolved solid rejection," *Sep. Purif. Technol.*, 2015, **141**, 339-353.

[76] S. P. Chenakin, G. Melaet, R. Szukiewicz, and N. Kruse, "XPS study of the surface chemical state of a Pd/(SiO_2 + TiO_2) catalyst after methane oxidation and SO_2 treatment," *J. Catal.*, 2014, **312**, 1-11 .

[77] L. Zeng, Z. Lu, M. Li, J. Yang, W. Song, D. Zeng, and C. Xie, "A modular calcination method to prepare modified N-doped TiO_2 nanoparticle with high photocatalytic activity," *Appl. Catal. B*, 2016, **183**, 308-316.

[78] J. Park, T. Back, W. C. Mitchel, S. S. Kim, S. Elhamri, J. Boeckl, S. B. Fairchild, R. Naik, and A. A. Voevodin, "Approach to multifunctional device platform with epitaxial graphene on transition metal oxide," *Sci. Rep.,* 2015, **5**, 14374.

[79] G. Ai, R. Mo, H. Li, and J. Zhong, "Cobalt phosphate modified TiO_2 nanowire arrays as co-catalysts for solar water splitting," *Nanoscale*, 2015, **7**, 6722-6728.

[80] P. Zhang, H. Fan, S. Tian, Y. Chen, and J. Yan, "Synergistic effect of phosphorus-nitrogen and silicon-containing chain extenders on the mechanical properties, flame retardancy and thermal degradation behavior of waterborne polyurethane," *RSC Adv.*, 2016, **6**, 72409-72422.

[81] Y. Li, S. Li, Y. Wang, J. Wang, H. Liu, X. Liu, L. Wang, X. Liu, W. Xue, and N. Ma, "Electrochemical synthesis of phosphorus-doped graphene quantum dots for free radical scavenging," *Phys. Chem. Chem. Phys.*, 2017, **19**, 11631-11638.

[82] D. S. Yang, D. Bhattacharjya, S. Inamdar, J. Park, and J. S. Yu, "Phosphorus-doped ordered mesoporous carbons with different lengths as efficient metal-free electrocatalysts for oxygen reduction reaction in alkaline media," *J. Am. Chem. Soc.*, 2012, **134**, 16127-16130.

[83] T. Y. Ma and S. Z. Qiao, "Acid-base bifunctional periodic mesoporous metal phosphonates for synergistically and heterogeneously catalyzing CO_2 conversion," *ACS Catal.*, 2014, **4**, 3847-3855.

Chapter 3

[1] H. M. Cobb, "Stainless steel applications," *Hist. Stainl. Steel*, ASM International 2010.

[2] H. S. Khatak, R. Baldev, "Corrosion of austenitic stainless steel: Mechanism, mitigation and monitoring" ASM International: Materials Park, OH, 2002.

[3] J. Hernandez, J. Genesca, and A. Muñoz, "Formation of iron-carbonate scale-layer and corrosion mechanism of API X70 pipeline steel in carbon dioxide-saturated 3% sodium chloride," *Afinidad*, 2012, 69 (560).

[4] L. M. Al-Hadhrami, A. Quddus, and D. A. Al-Otaibi, "Calcium sulfate scale deposition on coated carbon steel and titanium," *Desalin. Water Treat.*, 2013, **51**, 2521-2528.

[5] L. Liu, X. F. Guo, Q. Y. Guo, H. Q. Fan, and Z. H. Zhong, "Drag reduction of gas-liquid two-phase flow in steel pipes with different inclination geometry," *Adv. Mater. Res.*, Trans Tech Publication 2012, **433**, 463-470.

[6] T. Sun, L. Feng, X. Gao, and L. Jiang, "Bioinspired surfaces with special wettability," *Acc. Chem. Res*., 2005, **38**, 644-652.

[7] X. M. Li, D. Reinhoudt, and M. Crego-Calama, "What do we need for a superhydrophobic surface? A review on the recent progress in the preparation of superhydrophobic surfaces," *Chem. Soc. Rev.*, 2007, **36**, 1350-1368.

[8] P. Roach, N. J. Shirtcliffe, and M. I. Newton, "Progess in superhydrophobic surface development," *Soft Matter*, 2008, **4**, 224-240.

[9] A. Ahuja, J. A. Taylor, V. Lifton, A. A. Sidorenko, T. R. Salamon, E. J. Lobaton, P. Kolodner, and T. N. Krupenkin, "Nanonails: A simple geometrical approach to electrically tunable superlyophobic surfaces," *Langmuir*, 2008, **24**, 9-14.

[10] E. Bormashenko, T. Stein, G. Whyman, Y. Bormashenko, and R. Pogreb, "Wetting properties of the multiscaled nanostructured polymer and metallic superhydrophobic surfaces," *Langmuir*, 2006, **22**, 9982-9985.

[11] J. Y. Shiu, C. W. Kuo, P. Chen, and C. Y. Mou, "Fabrication of tunable superhydrophobic surfaces by nanosphere lithography," *Chem. Mater.*, 2004, **16**, 561-564.

[12] A. Nakajima, K. Hashimoto, T. Watanabe, K. Takai, G. Yamauchi, and A. Fujishima, "Transparent superhydrophobic thin films with self-cleaning properties," *Langmuir*, 2000, **16**, 7044-7047.

[13] A. Nakajima, A. Fujishima, K. Hashimoto, and T. Watanabe, "Preparation of transparent superhydrophobic boehmite and silica films by sublimation of aluminum acetylacetonate," *Adv. Mater.*, 1999, **11**, 1365-1368.

[14] M. Ma, Y. Mao, M. Gupta, K. K. Gleason, and G. C. Rutledge, "Superhydrophobic fabrics produced by electrospinning and chemical vapor deposition," *Macromolecules*, 2005, **38**, 9742-9748.

[15] K. Liu and L. Jiang, "Metallic surfaces with special wettability," *Nanoscale*, 2011, **3**, 825-838.

[16] N. J. Shirtcliffe, G. McHale, M. I. Newton, and Y. Zhang, "Superhydrophobic copper tubes with possible flow enhancement and drag reduction," *ACS Appl. Mater. Interfaces*, 2009, **1**, 1316-1323.

[17] J. Ou and J. P. Rothstein, "Direct velocity measurements of the flow past drag-reducing ultrahydrophobic surfaces," *Phys. Fluids*, 2005, **17**, 103606.

[18] C. H. Choi and C. J. Kim, "Large slip of aqueous liquid flow over a nanoengineered superhydrophobic surface," *Phys. Rev. Lett.*, 2006, **96**, 066001.

[19] Y. Liu, H. Cao, Y. Chen, S. Chen, and D. Wang, "Self-assembled super-hydrophobic multilayer films with corrosion resistance on copper substrate," *RSC Adv.*, 2016, **6**, 2379-2386.

[20] R. Fürstner, W. Barthlott, C. Neinhuis, and P. Walzel, "Wetting and self-cleaning properties of artificial superhydrophobic surfaces," *Langmuir*, 2005, **21**, 956-961.

[21] A. Lafuma and D. Quéré, "Superhydrophobic states," *Nat. Mater.*, 2003, **2**, 457.

[22] S. K. Biswas and K. Vijayan, "Friction and wear of PTFE - a review," *Wear*, 1992, **158**, 193-211.

[23] T. Ito, S. M. Forman, C. Cao, F. Li, Jr, C. R. Eddy, M. A. Mastro, R. T. Holm, R. L. Henry, K. L. Hohn, and J. H. Edgar, "Self-assembled monolayers of alkylphosphonic acid on GaN substrates," *Langmuir*, 2008, **24**, 6630-6635.

[24] W. Gao, L. Dickinson, C. Grozinger, F. G. Morin, and L. Reven, "Self-assembled monolayers of alkylphosphonic acids on metal oxides," *Langmuir*, 1996, **12**, 6429-6435 .

[25] R. Luschtinetz, A. F. Oliveira, H. A. Duarte, and G. Seifert, "Self-assembled monolayers of alkylphosphonic acids on aluminum oxide surfaces - A theoretical study," *Z. Anorg. Allg. Chem.*, 2010, **636**, 1506-1512.

[26] A. Ulman, *An Introduction to Ultrathin Organic Films: From Langmuir-Blodgett to Self-Assembly*. Academic Press, 2013.

[27] M. Toney, A. A. Virkar, S. Mannsfeld, J. H. Oh, M. Toney, J. Locklin, and Z. Bao, "Crystalline ultrasmooth self-assembled monolayers of alkylsilanes for organic field-effect transistors," *J. Am. Chem. Soc.*, 2009, **131**, 9396-9404.

[28] B. Adolphi, E. Jähne, G. Busch, and X. Cai, "Characterization of the adsorption of ω-(thiophene-3-yl alkyl) phosphonic acid on metal oxides with AR-XPS," in *Analytical and Bioanalytical Chemistry*, 2004, **379**, 646-652.

[29] E. S. Gawalt, M. J. Avaltroni, N. Koch, and J. Schwartz, "Self-assembly and bonding of alkanephosphonic acids on the native oxide surface of titanium," *Langmuir*, 2001, **17**, 5736-5738.

[30] A. Raman, M. Dubey, I. Gouzman, and E. S. Gawalt, "Formation of self-assembled monolayers of alkylphosphonic acid on the native oxide surface of SS316L," *Langmuir*, 2006, 22, 6469-647.

[31] A. Raman and E. S. Gawalt, "Self-assembled monolayers of alkanoic acids on the native oxide surface of SS316L by solution deposition," *Langmuir*, 2007, **23**, 2284-2288.

[32] N. S. Bhairamadgi, S. P. Pujari, F. G. Trovela, A. Debrassi, A. A. Khamis, J. M. Alonso, A. A. Al Zahrani, T. Wennekes, H. A. Al-Turaif, C. van Rijn, and Y. A. Alhamed, "Hydrolytic and thermal stability of organic monolayers on various inorganic substrates," *Langmuir*, 2014, **30**, 5829-5839.

[33] S. S. Latthe, P. Sudhagar, A. Devadoss, A. M. Kumar, S. Liu, C. Terashima, K. Nakata, and A. Fujishima, "A mechanically bendable superhydrophobic steel surface with self-cleaning and corrosion-resistant properties," *J. Mater. Chem. A*, 2015, **3**, 14263-14271.

[34] L. B. Boinovich, A. M. Emelyanenko, V. K. Ivanov, and A. S. Pashinin, "Durable icephobic coating for stainless steel," *ACS Appl. Mater. Interfaces*, 2013, **5**, 2549-2554.

[35] T. T. Isimjan, T. Wang, and S. Rohani, "A novel method to prepare superhydrophobic, UV resistance and anti-corrosion steel surface," *Chem. Eng. J.*, 2012, **210**, 182-187.

[36] Y. Thomas, "An essay on the cohesion of fluids," *Philos. Trans. R. Soc. London*, 1805, **95**, 65-87.

[37] D. Y. Kwok, C. N. C. Lam, A. Li, A. Leung, R. Wu, E. Mok, and A. W. Neumann, "Measuring and interpreting contact angles: A complex issue," *Colloids Surf. A,* 1998, **142**, 219-235.

[38] H. Tavana, C. N. C. Lam, K. Grundke, P. Friedel, D. Y. Kwok, M. L. Hair, and A. W. Neumann, "Contact angle measurements with liquids consisting of bulky molecules," *J. Colloid Interface Sci.*, 2004, **279**, 493-502.

[39] T. T. Chau, "A review of techniques for measurement of contact angles and their applicability on mineral surfaces," *Miner. Eng*., 2009, **22**, 213-219.

[40] A. W. Adamson and A. P. Gast, *Physical Chemistry of Surfaces, Sixth Edition*. 1997.

[41] R. N. Wenzel, "Surface roughness and contact angle," *J. Phys. Chem.*, 1949, **53**, 1466-1467.

[42] A. Tuteja, W. Choi, M. Ma, J. M. Mabry, S. A. Mazzella, G. C. Rutledge, G. H. McKinley, and R. E. Cohen, "Designing superoleophobic surfaces," *Science*, 2007, **318**, 1618-1622.

[43] H. S. Awad, "The effect of zinc-to-HEDP molar ratio on the effectiveness of zinc-1, hydroxyethylidene-1,1 diphosphonic acid in inhibiting corrosion of carbon steel in neutral solutions," *Anti-Corrosion Methods Mater.*, 2005, **52**, 22-28.

[44] S. Farsinezhad, P. R. Waghmare, B. D. Wiltshire, H. Sharma, S. Amiri, S. K. Mitra, and K. Shankar, "Amphiphobic surfaces from functionalized TiO_2 nanotube arrays," *RSC Adv.*, 2014, **4**, 33587-33598.

[45] Z. Chu and S. Seeger, "Superamphiphobic surfaces," *Chem. Soc. Rev*., 2014, **43**, 2784-2798.

[46] B. Bhushan, K. Koch, and Y. C. Jung, "Nanostructures for superhydrophobicity and low adhesion," *Soft Matter*, 2008, **4**, 1799-1804.

[47] A. B. D. Cassie, "Contact angles," *Discussions of the Faraday Society*. 1948, **3**, 11-16.

[48] F. S. de Souza and A. Spinelli, "Caffeic acid as a green corrosion inhibitor for mild steel," *Corros. Sci.*, 2009, **51**, 642-649.

[49] V. Swamy, A. Kuznetsov, L. S. Dubrovinsky, R. A. Caruso, D. G. Shchukin, and B. C. Muddle, "Finite-size and pressure effects on the Raman spectrum of nanocrystalline anatase TiO_2," *Phys. Rev. B*, 2005, **71**, 184302.

[50] G. A. Tompsett, G. A. Bowmaker, R. P. Cooney, J. B. Metson, K. A. Rodgers, and J. M. Seakins, "The Raman spectrum of brookite, TiO_2 (Pbca, Z = 8)," *J. Raman Spectrosc.*, 1995, **26**, 57-62.

[51] R. Luschtinetz, J. Frenzel, T. Milek, and G. Seifert, "Adsorption of phosphonic acid at the TiO_2 anatase (101) and rutile (110) surfaces," *J. Phys. Chem. C*, 2009, **113**, 5730-5740.

[52] N. S. Bhairamadgi, S. P. Pujari, F. G. Trovela, A. Debrassi, A. A. Khamis, J. M. Alonso, A. A. Al Zahrani, T. Wennekes, H. A. Al-Turaif, C. van Rijn, and Y. A. Alhamed, "Hydrolytic and thermal stability of organic monolayers on various inorganic substrates," *Langmuir*, 2014, **30**, 5829-5839.

[53] N. Kantor-Uriel, P. Roy, S. Saris, V. Kiran, D. H. Waldeck, and R. Naaman, "Evidence for enhanced electron transfer by multiple contacts between self-assembled organic monolayers and semiconductor nanoparticles," *J. Phys. Chem. C*, 2015, **119**, 15839-15845.

[54] N. S. Bhairamadgi, S. P. Pujari, F. G. Trovela, A. Debrassi, A. A. Khamis, J. M. Alonso, A. A. Al Zahrani, T. Wennekes, H. A. Al-Turaif, C. van Rijn, and Y. A. Alhamed, "Hydrolytic and thermal stability of organic monolayers on various inorganic substrates," *Langmuir*, 2014, **30**, 5829-5839.

[55] A. Ulman, "An Introduction to Ultrathin Organic Films: From Langmuir-Blodgett to Self-Assembly," *Academic press*, 2013.

[56] A. Ramirez, S. Shuman, and B. Schwer, "Human RNA 5′-kinase (hClp1) can function as a tRNA splicing enzyme in vivo," *RNA*, 2008, **14**, 1737-1745.

[57] M. Grossi and B. Riccò, "Electrical impedance spectroscopy (EIS) for biological analysis and food characterization: A review," *J. Sensors Sens. Syst.*, 2017, **6**, 303-325.

[58] J. Zhu, A. Bailly, M. Zwiewka, V. Sovero, M. Di Donato, P. Ge, J. Oehri, B. Aryal, P. Hao, M. Linnert, and N. I. Burgardt, "TWISTED DWARF1 mediates the action of auxin transport inhibitors on actin cytoskeleton dynamics.," *Plant Cell*, 2016, **28**, 930-948.

[59] M. Edalatpour, L. Liu, A. Jacobi, K. Eid and A. Sommers, "Managing water on heat transfer surfaces: A critical review of techniques to modify surface wettability for applications with condensation or evaporation," *Applied Energy*, 2018, **222**, 967–992.

[60] Y. Wei, H. Qi, X. Gong and S. Zhao, "Specially Wettable Membranes for Oil–Water Separation," *Advanced Materials Interfaces*, 2018, **5**, 1800576.

[61] P. Roy, R. Kisslinger, S. Farsinezhad, N. Mahdi, A. Bhatnagar, A. Hosseini, L. Bu, W. Hua, B. D. Wiltshire, A. Eisenhawer, P. Kar and K. Shankar, "All-solution processed, scalable superhydrophobic coatings on stainless steel surfaces based on functionalized discrete titania nanotubes," *Chemical Engineering Journal*, 2018, **351**, 482–489.

Chapter 4

[1] C. Ruan, M. Paulose, O. K. Varghese, G. K. Mor, and C. A. Grimes, "Fabrication of highly ordered TiO_2 nanotube arrays using an organic electrolyte," *J. Phys. Chem. B*, 2005, 109, 15754-15759.

[2] F. Fabregat-Santiago, E. M. Barea, J. Bisquert, G. K. Mor, K. Shankar, and C. A. Grimes, "High carrier density and capacitance in TiO_2 nanotube arrays induced by electrochemical doping," *J. Am. Chem. Soc.*, 2008, **130**, 11312-11316.

[3] R. Krupke, F. Hennrich, H. v. Löhneysen, and M. M. Kappes, "Separation of metallic from semiconducting single-walled carbon nanotubes," *Science*, 2003, **301**, 344-347.

[4] A. Tighineanu, T. Ruff, S. Albu, R. Hahn, and P. Schmuki, "Conductivity of TiO_2 nanotubes: Influence of annealing time and temperature," *Chem. Phys. Lett.*, 2010, **494**, 260-263.

[5] A. Claro, M. J. Melo, S. Schäfer, J. S. S. de Melo, F. Pina, K. J. van den Berg, and A. Burnstock, "The use of microspectrofluorimetry for the characterization of lake pigments," *Talanta*, 2008, **74**, 922-929.

[6] C. Miliani, A. Romani, and G. Favaro, "Acidichromic effects in 1,2-di- and 1,2,4-trihydroxyanthraquinones. A spectrophotometric and fluorimetric study," *J. Phys. Org. Chem.*, 2000, **13**, 141-150.

[7] J. E. Moser, "On the kinetics and mechanism of light-induced electron transfer at the semiconductor/electrolyte interface," *Sol. Energy Mater. Sol. Cells*, 1995, **38**, 343-345.

[8] R. Huber, J. E. Moser, M. Grätzel, and J. Wachtveitl, "Real-time observation of photoinduced adiabatic electron transfer in strongly coupled dye/semiconductor colloidal systems with a 6 fs time constant," *J. Phys. Chem. B*, 2002, **106**, 6494-6499.

[9] W. S. Alencar, W. S. Alencar, E. C. Lima, B. Royer, B. D. dos Santos, T. Calvete, E. A. da Silva, C. N. Alves, "Application of aqai stalks as biosorbents for the removal of the Dye Procion Blue MX-R from aqueous solution," *Sep. Sci. Technol.*, 2012, **47**, 513-526.

[10] D. C. Dos Santos, M. A. Adebayo, E. C. Lima, S. F. Pereira, R. Cataluña, C. Saucier, P. S. Thue, F. M. Machado, "Application of carbon composite adsorbents prepared from coffee waste and clay for the removal of reactive dyes from aqueous solutions," *J. Braz. Chem. Soc.*, 2015, **26**, 924-938.

[11] M. J. Puchana-Rosero, M. A. Adebayo, E. C. Lima, F. M. Machado, P. S. Thue, J. C. P. Vaghetti, C. S. Umpierres, M. Gutterres, "Microwave-assisted activated carbon obtained from the sludge of tannery-treatment effluent plant for removal of leather dyes," *Colloids Surfaces A Physicochem. Eng. Asp.*, 2016, **504**, 105-115.

[12] R. K. Gautam, A. Mudhoo, and M. C. Chattopadhyaya, "Kinetic, equilibrium, thermodynamic studies and spectroscopic analysis of Alizarin Red S removal by mustard husk," *J. Environ. Chem. Eng.*, 2013, **1**, 1283-1291.

[13] D. S. Rahman, H. Chatterjee and S. K. Ghosh, "Excess surface energy at the tips of gold nanospikes: From experiment to modeling," *The Journal of Physical Chemistry C*, 2015, 150615143906005.

[14] L. C. T. Shoute and G. R. Loppnow, "Excited-state dynamics of alizarin-sensitized TiO_2 nanoparticles from resonance Raman spectroscopy,"*The Journal of Chemical Physics*, 2002, **117**, 842–850.